Experimental Testing of Geomechanical Behavior of Fiber-Reinforced Cemented Paste Backfill (FR-CPB) under Warmer Curing Temperature

by

Iarley Loan Sampaio Libos

A thesis
submitted to the Faculty of Graduate Studies
in partial fulfilment of the requirements for the
Degree of Master of Science
in

Civil Engineering

Supervisor
Dr. Liang Cui
Assistant Professor – Dept. of Civil Engineering

Lakehead University
Thunder Bay, Ontario
June 2020

Author’s Declaration Page

Here, I declare that this is the original thesis dissertation document of Iarley Loan Sampaio Libos with the inclusion of any final revisions suggested by the examiners' committee and that this is my authorship work. I authorize this document to be electronically available to the public.

Abstract

Backfilling techniques enable improved ore recovery and structural stability to underground mines employing a material to fill the voids after the excavation. Fiber-reinforced cemented paste backfill (FR-CPB) is this material and it consists of mine tailings, cement, mixing, and fibers. After placed into the underground space (called stope), FR-CPB provides sufficient ground support, enables the exploration of larger amounts of ore since no orebody pillars are required to sustain the excavations, and thus enhances mining production. The reinforcement technique has been considered as a promising approach for the backfilling design. However, regarding that mining activities may take place at a depth of more than 1000 meters, the geothermal gradient can not only change the temperature of FR-CPB but also affect its geomechanical behaviors due to its temperature-dependent characteristics. Therefore, the objective of this research is to experimentally investigate compression, tension, shear, triaxial, and fracture behaviors of FR-CPB subjected to different warmer curing temperatures (20°C, 35°C, and 45°C). Moreover, to identify the mechanisms responsible for the evolution of geomechanical behavior, a series of mold-based monitoring programs have been designed and performed to measure changes related to matric suction, electrical conductivity, and temperature in FR-CPB. Additionally, to determine the progress of binder hydration and associated microstructure change, extensive X-ray diffraction (XRD) analysis and scanning electron microscopy (SEM) observation have been conducted at the microscale. The obtained results evidenced that warmer curing temperature can significantly affect the fiber-CPB matrix interfacial interaction. Correspondingly, the geomechanical (including tensile, compressive, shear, and fracture) behavior show strong temperature sensitivity from early to advanced ages. Therefore, the obtained results from the present study can not only improve the understanding of the geomechanical behavior of FR-CPB but also contribute to the safe design of backfill structures in underground mines.

Keywords: Backfilling, Cementitious Material, FR-CPB, Geothermal Gradient, Temperature, Compressive Strength

Acknowledgment

At first, I would like to thank God for blessing me with health, clarity, and strength to persevere in this path to accomplish such a challenging task. I would like to express all my gratitude towards Dr. Liang Cui, my thesis degree supervisor, for not only offer me this opportunity and believe in my work but also for his brilliant mentorship and incredible support.

Thank you to my family in Brazil (Fabio Libos, Tais E.S.O. Libos, Ully H.S. Libos, Iann M.S. Libos, and Alana M.S. Oliveira) for their advice, good words, care, and motivation even from far away, always believing in my potential. One more thank you to my Canadian Family (Greg Hanlon, Suzanne Hanlon, Saffron Hanlon, Corina Hanlon, and Olivia Hanlon) for all their support, understanding, and care during the entire journey of my graduate studies in Canada.

My special thanks to Robert Timoon and Cory Hubbard, my laboratory technicians and friends, for all their help, good advice, time, and experiences construction process throughout all the moments we spent together in the lab overcoming every single challenge imposed. Other special thanks to Sai Pramod Singalreddy, my dear friend and also master`s student, for sharing the best and worst moments in the lab, for being the living witness of everything that was overcome to accomplish this achievement, and for being such a wonderful human being.

Lastly, but of utmost importance, I would like to thank my thesis committee members, Dr. Ahmed Elshaer and Dr. Wilson Wang, for their time, consideration, and valuable suggestions to further enhance this work.

Table of Contents

List of Tables

List of Figures

List of Abbreviations

CPB	Cemented Paste Backfill
FR-CPB	Fiber-Reinforced Cemented Paste Backfill
C_c	Cement content
w/c	Water-to-cement ratio
$\%_{CW}$	Solids by weight
$\%_{CV}$	Solids by volume
SEM	Scanning Electron Microscopy
CTRL	Control group
UCS	Unconfined Compressive Strength
STS	Splitting Tensile Strength
DS	Direct Shear
CU	(Consolidated & Undrained) Triaxial
TPB	Three-Point Bending
SCB	Semicircular Bend
MS-DA	Material strength-based design approach
LVDT	Linear Variable Differential Transformer
EC	Electrical Conductivity
ISRM	International Society for Rock Mechanics

Nomenclature

Roman

P_{max}	Maximum load
F_x	*S*hear force
P_a	Given applied axial load
P_m	Peak load from TPB test
P	Maximum force
D	Averaged diameter of the specimen
t	Thickness of the specimen
A	Surface area of the specimen
B	Thickness of the specimen
W	Width or height of the specimen
D	Diameter of semicircular specimen
T	Thickness of semicircular specimen
a	Notch length
K_{IC}	Mode-I (opening) Fracture Toughness – ASTM D5045 method
Y_I	Normalized stress intensity factor for mode I
Y_{II}	Normalized stress intensity factor for mode II
K_I	Mode-I fracture toughness – SCB Method proposed by ISRM
K_{II}	Mode-II fracture toughness – SCB Method proposed by ISRM
K_{eff}	Mixed-Mode fracture toughness – SCB Method proposed by ISRM
CS	Chemical shrinkage coefficient
m_c	Initial mass of cement in the flask

I_b	Brittleness index
Δu	Pore water pressure variation

Greek

σ_t	Splitting tensile strength
τ	Nominal shear stress
$(\sigma_1 - \sigma_3)$	Measured principal stress difference or deviator stress
α	Notch inclination angle
ΔV	Volume change of water measured by the graduated pipette
β	Pore water coefficient
$\Delta\sigma_3$	Confining pressure variation
τ_{max}	Peak shear strength
τ_{res}	Residual shear strength

Chapter 1 Introduction

1.1. Background and Research Motivation

Cemented paste backfill (CPB) is mainly composed of tailings (78 to 85% solid mass concentration), a binding agent (3-7%), and mixing water (Belem and Benzaazoua, 2008). CPB delivers an eco-friendly aspect to the mining scenario as it integrates tailings produced by the mine in its composition, reducing waste disposal costs and environmental problems (Yilmaz, 2011). After placement into the mine`s stope (underground cavities), CPB not only acts as major ground support for pillars and rock walls but also serves as a working platform for further mining operations (Sivakugan et al., 2015). Figure 1.1 illustrates the field scenario where CPB is poured into a mine stope.

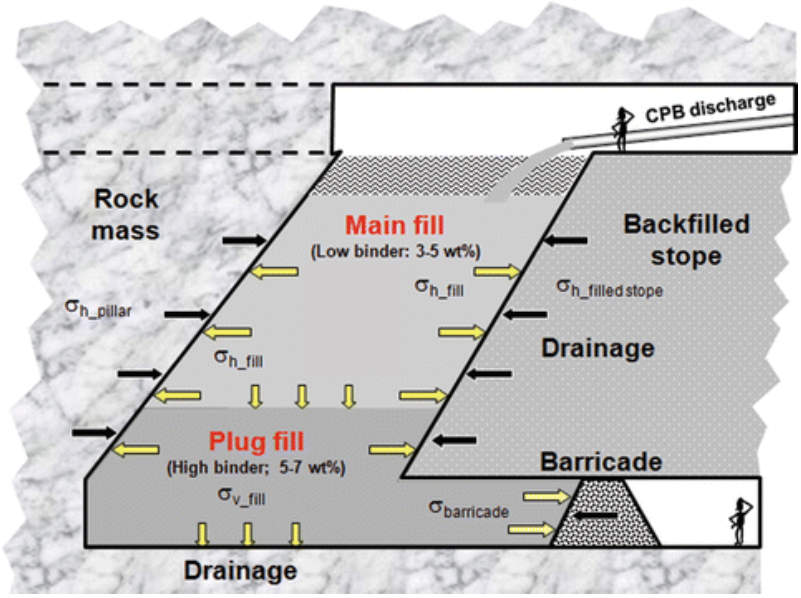

Figure 1.1 – CPB utilization inside a stope during field operations (Adapted from Karaoglu and Yilmaz (2017)).

However, it is important to highlight that CPB is utilized in underground mines where valuable orebodies are extracted from thousands of meters below ground level (Marschalko et al. 2012). According to the previous study of Pourmalek and Shariatipour (2019), the geothermal gradient exerts an increment of approximately 25°C to 45°C per kilometer (see Figure 1.2), which indicates that fresh CPB will be cured under warmer temperature after poured into an underground mine stope. Moreover, acknowledging that FR-CPB is a type of cementitious material, its properties and

behavior are temperature-sensitive (Schindler A. 2004). Therefore, the warmer curing temperature must be fully considered in the design of mine backfill.

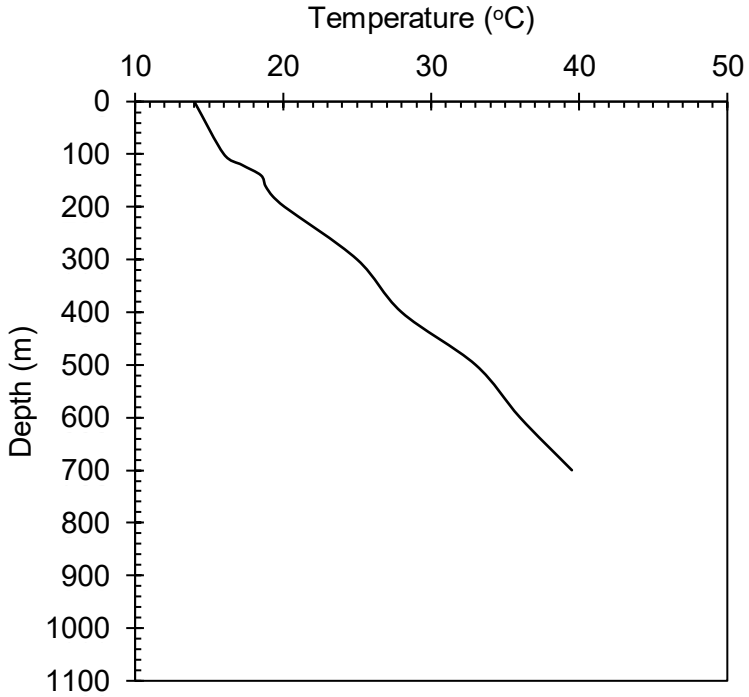

Figure 1.2 – Geothermal gradient referent to depth (adapted from Blackwell and Steele, 1989).

Moreover, to improve the mechanical behavior and performance of CPB, fiber reinforcement has been considered as a promising technique (Yi et al., 2015), being this modified material called fiber-reinforced cemented paste backfill (FR-CPB). The mechanical stability has been considered to be a critical criterion for mine backfill design (Xiawei, Y., 2016). However, after placed into the underground excavations, FR-CPB is subjected to complex field loading conditions. In consequence, the geomechanical (including compressive, tensile, shear, and fracture) behavior of FR-CPB must be evaluated simultaneously to yield a safe design of mine backfill.

For the compressive behavior, the mine backfill mass is progressively exposed without the presence of confining pressure (free-standing wall scenario) as pillar recovery processes (see Figure 1.3), evidencing the critical role that unconfined compressive strength (UCS) played in the safe design (Yilmaz et al., 2015). Therefore, to satisfy the design requirements on mechanical stability, the strength-based design method (UCS-based) has been adopted by the US Environmental Protection Agency (1989) to regulate CPB design.

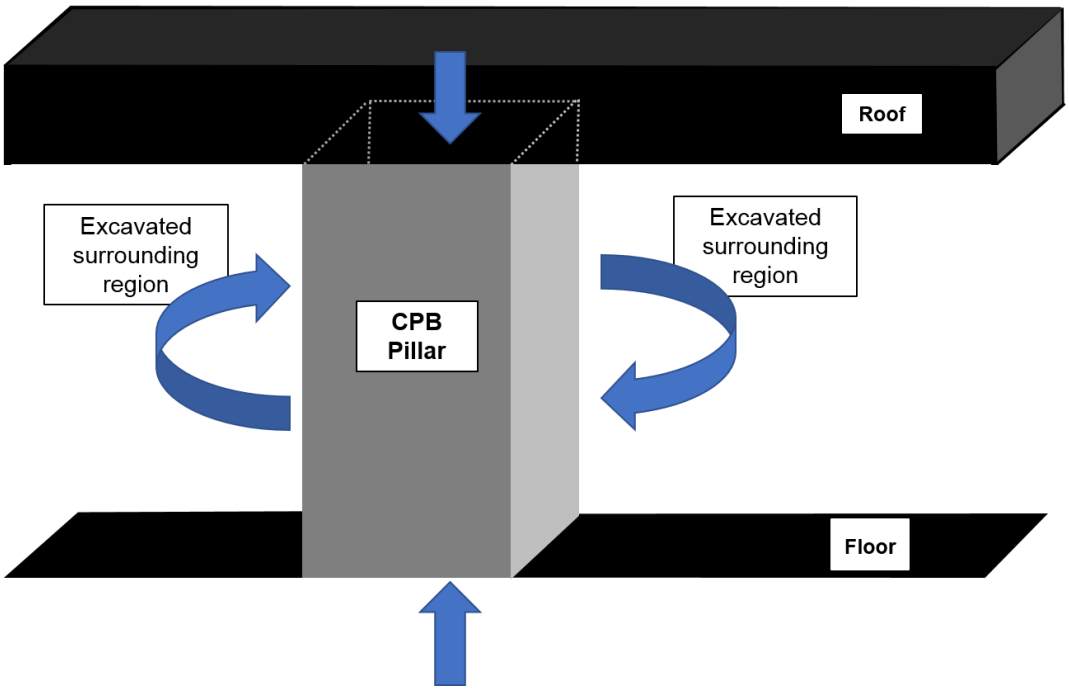

Figure 1.3 – Free-standing wall representation.

Also, a few experimental studies have been conducted to investigate the development of UCS in FR-CPB. Mitchell and Stone (1987) confirmed that the inclusion of fiber can effectively improve the UCS of CPB and thus reduce the usage of costly cement. Yi et al. (2015) found that FR-CPB with 5% cement and 0.5% fiber content evidences an increase of 70%~90% in UCS compared to CPB without fiber inclusion.

For the tensile stress, Grice (1998) addresses that the tensile stress develops in CPB mass when the underhand cut and fill mining method is adopted. Correspondingly, the tensile strength plays a critical role in the mechanical stability of such CPB structures. However, as a type of cementitious material, the tensile strength of CPB is weaker relative to its compressive strength (Jaber et al. 2018; Baldovino et al. 2018; Chhorn et al. 2018). Therefore, through the fiber bridging effect, the addition of fibers can significantly improve the tensile behavior of CPB. However, due to the temperature sensitivity of cement hydration, warmer curing temperatures can affect the fiber-CPB matrix interfacial interaction. Therefore, it is necessary to investigate the effect of warmer curing temperatures on the tensile behavior of FR-CPB. Figure 1.4 depicts the previously mentioned scenario.

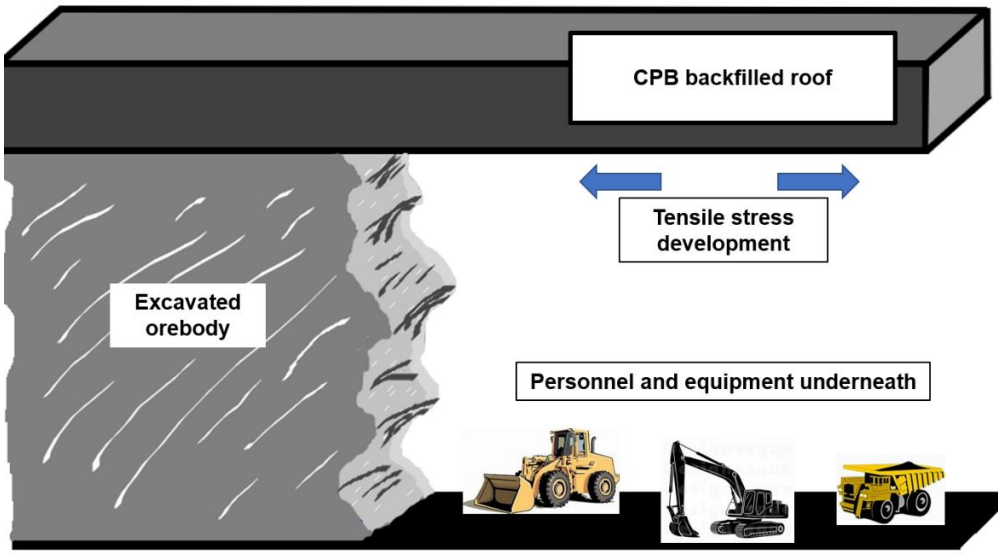

Figure 1.4 – Tensile stress development.

Apart from the compressive and tensile behavior, the shear behavior of FR-CPB also affects its mechanical stability. Specifically, after poured into stopes FR-CPB is confined by surrounding rocks with a rough surface due to the blasting operation (Singh et al. 2016). Meanwhile, the consolidation process of FR-CPB will trigger the passive shear resistance along the rock walls. Consequently, the shear stress develops in the CPB-rock interfacial transition zone (see Figure 1.5), and thus influences the stress state in backfill mass. Therefore, the shear behavior is another concern to safely design FR-CPB.

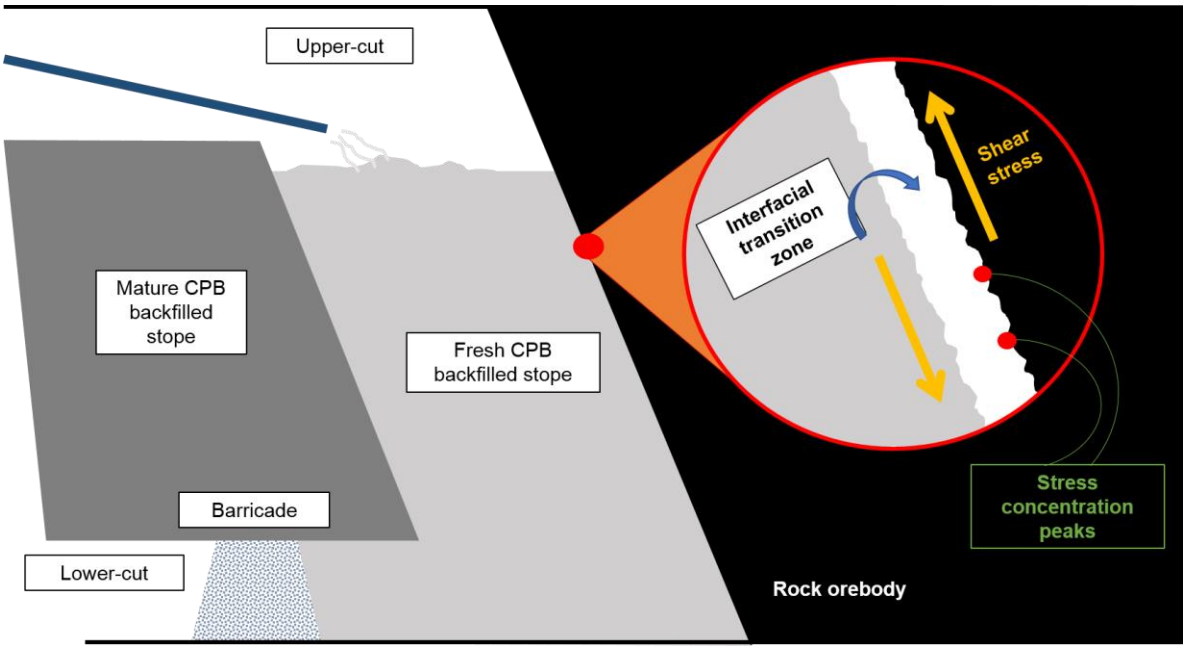

Figure 1.5 – Pre-existing notches field scenario during stope backfilling.

Furthermore, the irregular rock surface possesses pre-existing notches (Nyberg and Fjellborg, 2000) which have randomly concave and convex surfaces at the micro- and macro-scale. Therefore, the surface topography of soft FR-CPB is dominated by the rough rock walls. As a result, the surface notches can be widely formed along the CPB surfaces. However, the stress concentration near the notch (i.e., crack) fronts may directly cause the crack propagation and coalescence, and thus the failure of FR-CPB (Susmel, 2009). Therefore, assessment of fracture behavior of FR-CPB is a prerequisite for the development of effective measures to control local failure events and a global collapse of the structure (Pham, 2000).

Additionally, due to the overburden pressure and in-situ horizontal stress (Su and Peng, 1987), the unequal principal stresses are commonly featured in FR-CPB mass. For instance, as shown in Figure 1.6, FR-CPB pillar structures surrounded by an orebody matrix or by a backfilled material matrix are common during field operations in underground mines (Altun et al. 2010). Therefore, to better understand and assess the in-situ mechanical behavior of FR-CPB subjected to confinement and axial load simultaneously, the investigation of the triaxial behavior is crucial to the safe design of backfill structures.

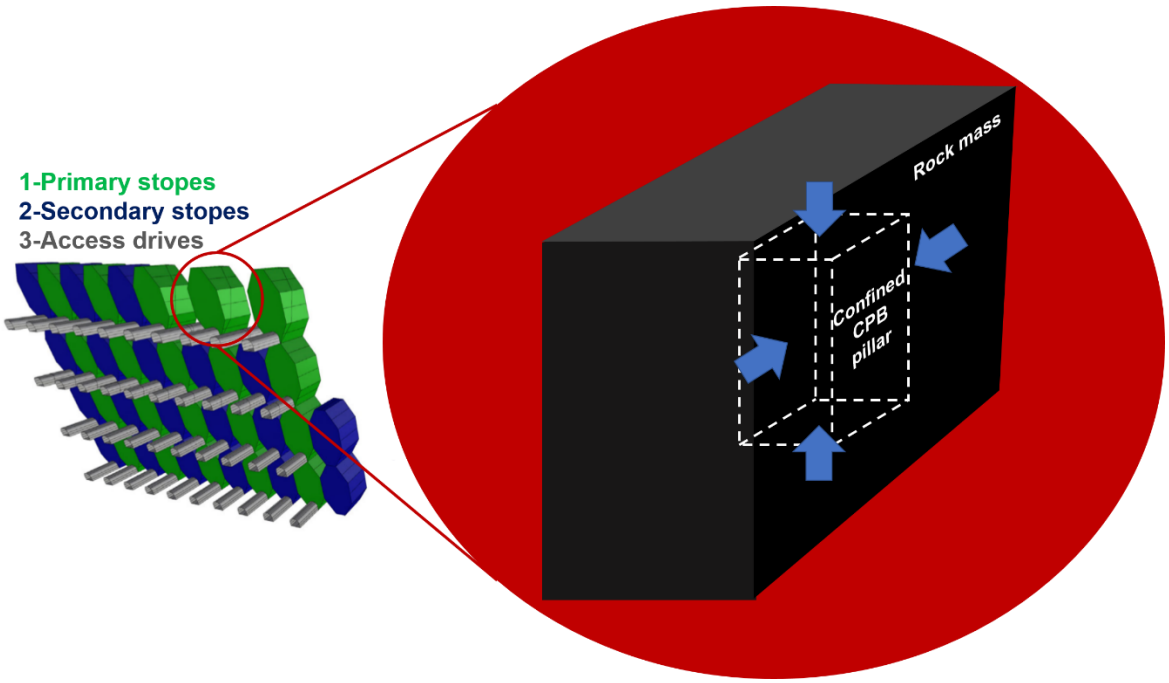

Figure 1.6 – Confined pillar where triaxial shear behavior is predominant (adapted from Sivakugan et al. 2015).

Therefore, the compressive, tensile, shear, and fracture behaviors must be fully studied to provide a concrete understanding of the geomechanical behavior of FR-CPB, which can contribute

towards the optimization of design criteria. Moreover, as mentioned previously, the geothermal gradient in underground mines directly results in the warmer curing temperature conditions. Due to the curing temperature dependence of cementitious materials (Fall et al., 2010), it is required to incorporate the thermal factor into the study on the geomechanical behavior of FR-CPB.

Additionally, to guide this experimental study, a theoretical framework based on the elastoplasticity theory (Aboudi, 1984) and fracture mechanics theory (Andrews, 1974) was employed. The knowledge related to the elastoplastic deformation of geomaterials, accounting for its constitutive matrix and its structural evaluation under plastic deformation, helped to develop this study. Also, the insight related to stress concentration, fracture propagation, materials` surface work and energy, and energy dissipation from fracture mechanics theory were of fundamental importance to enable a solid comprehension of the obtained results.

1.2. Research Objectives

To evaluate the geomechanical behavior of FR-CPB subjected to warmer curing temperatures, a series of laboratory experiments and monitoring programs were conducted in this study. Based on the present study, the specific objectives are summarized as follows:

1. Experimentally investigate the compression and tension behavior of FR-CPB subjected to warmer temperature and develop a predictive model to capture the relationship between compressive and tensile strength;
2. Experimentally study the effect of warmer curing temperature on the shear-displacement behavior and shear constitutive properties (including shear stiffness, cohesion, angle of internal friction, and dilation angle), and develop a series of predictive models to characterize the evolution of shear constitutive properties of FR-CPB from early to advanced ages;
3. Experimentally evaluate the effect of curing temperature on the constitutive behavior including stress-strain relation, volume change, and pore-water pressure evolution in FR-CPB subjected to triaxial loading conditions.
4. Experimentally investigate the effects of curing time, cement content, and saturation state (saturated and unsaturated state) on the evolution of mode-I fracture toughness of CPB, also investigating the fracture behavior of FR-CPB subjected to various curing temperatures. Scanning electron microscope (SEM) observations and dry density measurements were applied to validate the results.

1.3. Methodology

To achieve the research objectives in this research work, extensive experimental studies and analytical analyses were conducted. The detailed information about the research methodology section was listed as follows:

1. Build knowledge and awareness about FR-CPB technology through a complete and detailed literature review and identify the research gap related to their applications and design criteria.
2. Utilize ASTM C192/C192M-13a guidance to convey all sample preparation and storage processes.
3. Apply the procedures and calculations present in ASTM C39/C39M-18 and ASTM D3967-16 as references to perform, respectively, compression and tensile tests on temperature cured control CPB and FR-CPB samples. Furthermore, use data analysis to establish a linear fitting function to predict the material`s tensile strength correlated to its UCS.
4. Employ ASTM D3080/D3080M-11 calculations and procedures as guidance to investigate the shear behavior of control CPB and FR-CPB samples cured at different warmer temperatures.
5. Based on ASTM D4767-11, triaxial tests were conducted on control CPB and FR-CPB samples to investigate the stress-strain behavior, volume change, and pore water pressure when subjected to warmer temperatures.
6. According to ASTM D5045-14 and (ISRM) Semicircular Bend (SCB) method was utilized to obtain the fracture toughness of CPB and FR-CPB samples cured at various warmer temperatures.
7. Through the incorporation of matric suction sensor and electric conductivity sensor, a series of mold-based monitoring programs were designed and conducted on the FR-CPB subjected to different curing temperatures. The monitored results were used to interpret the evolution of the geomechanical behavior of FR-CPB.

Through the auxiliary laboratory analysis including chemical shrinkage measurement (based on ASTM C1608-17), scanning electron microscopy (SEM) observation, and dry density determination (based on ASTM D7263-18), the microstructure change of FR-CPB was identified and used to explain the effect of warmer curing temperature on the geochemical behavior of FR-CPB.

For the implementation of research methodology, this research was divided into three different research components including 1) laboratory testing; 2) mold-based monitoring; and 3) auxiliary laboratory analysis. Each component was subdivided into smaller testing sections that were scheduled between April 2019 and January 2020. The testing program covers all the tests necessary to investigate specific behaviors of FR-CPB and allow the understanding of its mechanical behavior (component one). The mold-based monitoring program was used to assess the development of the binder hydration products inside the material, using electronic sensors to quantitatively measure important parameters (component two). Lastly, auxiliary laboratory analysis was conducted to demonstrate the macro and microstructure of FR-CPB, providing proof and evidence of changes observed when submitting the material to different curing conditions (component three). To better showcase how the experimental programs were organized, the diagram in Figure 1.7 was created.

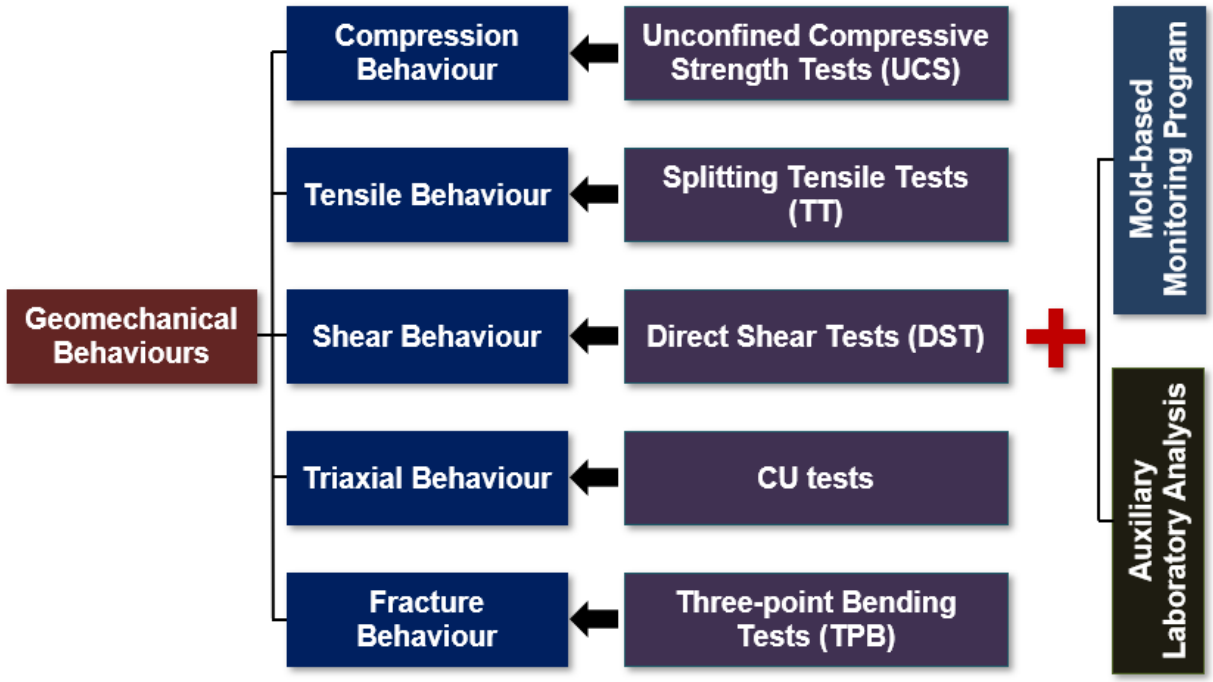

Figure 1.7 – Dissertation main programs organization.

1.4. Thesis Organization

To better present and arrange this research work, it was divided into 5 main chapters. The **first chapter** introduces the background information, research objectives, methodology, and thesis organization. The **second chapter** focuses on mining operation processes and explores in-depth

knowledge related to backfilling technologies with emphasis on CPB and FR-CPB. Also, it builds awareness about the present research gap. The **third chapter** delivers a detailed description of testing materials and equipment used in this research, how the laboratory programs were divided, how the tests were organized, and which processes were followed. Also, it covers the applied calculations with the corresponding equations, and all the details necessary to guarantee the replicability of this study. The **fourth chapter** is to present the experimental results and associated discussion on the effect of warmer curing temperature on the geomechanical behavior of FR-CPB. Based on all the information provided by the other four chapters, the **fifth chapter** presents a summary of the most important conclusions obtained and also provides recommendations for possible future works that can further improve the area of study of this research.

Chapter 2 Literature Review

2.1. Mining Operations Overview

The underground mine technique focuses on extracting valuable orebodies from the underground, reaching depths of thousands of meters below the surface (Chen et al., 2003). When an ore deposit of elevated grade is found with proper dimensions to justify the costs of its extraction operations, then it is time to assess optimum methods to retrieve all the ore from deep inside the underground (Hamrin et al. 2001). The methods utilized to explore orebodies from the underground depend not only on the financial aspect of the employed procedures, but they also rely on the characteristics of the surrounding rock and the orebody itself (Harraz, 2010). However, to be able to apply any methods and finally reach the orebody location, the construction of the infrastructure of the mine (ramps, shafts, tunnels, winzes) should be first executed accordingly to the mining plans, named as "dead work" (Brown, 2003). Figure 2.1 evidences the basic infrastructure of an underground mine with a concrete plant at the ground level.

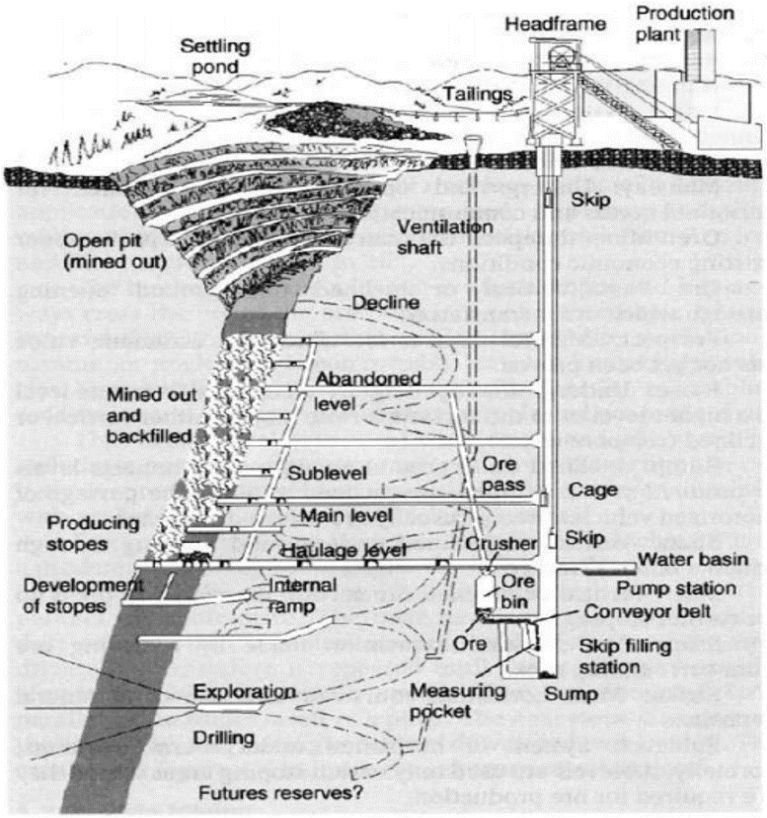

Figure 2.1 – Underground mine infrastructure - Ground level concrete plant scenario (Hartman and Mutmansky, 2002).

Due to the complex geological conditions and associated mining plans, the target mineral resources can be recovered by various mining methods including room and pillar mining, longwall, and cut and fill stoping approaches. Largely applied in coal mines, the room and pillar method extracts mineral material in a segmented format leaving untouched structures (pillars) of material to carry the load from the ground (Hartman and Matmansky, 2002). After the orebody is depleted, the miners start to carefully remove the pillars on their way back, permitting the roof to collapse (Kim et al. 2019). Figure 2.2 depicts the room and pillar method application in a coal mine.

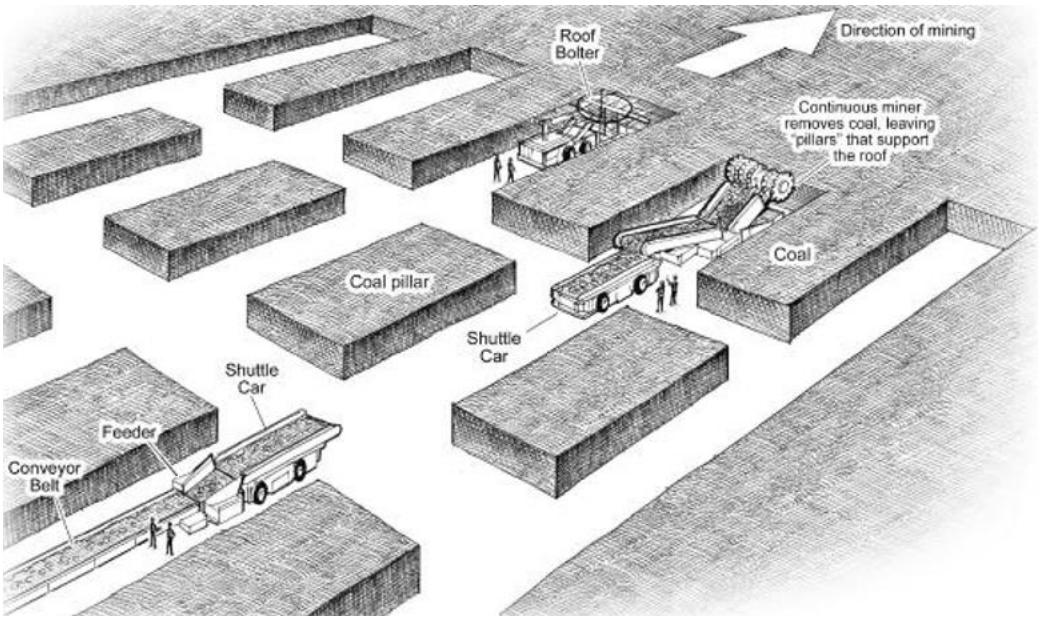

Figure 2.2 – Room and Pillar method applied to a coal mine (US Securities and Exchange Commission, 1989).

The longwall mining method is a heavy-machinery based stoping method. Rotary drums grind the material from the orebody while a conveyor belt system beneath them collects and transports the broken raw ore to a processing station (Okubo and Yamatomi, 2009). Hydraulic supports sustain the weight of the ceiling during mining operations and thus control the roof subsidence after a certain strip of material is mined (Peng, 2006). Figure 2.3 presents a schematic comprehension of the longwall mining method.

The cut and fill method is becoming more popular in the mining industry due to the abundance of filling material present in mines and the environmental benefits it delivers. In this method, stoping processes are employed. Correspondingly, drilling, blasting, loading, and transporting are the main activities employed during this mining process. Then, the excavated underground openings will be backfilled (Huang, 2019). Although the cut and fill method inevitably increases

the operational cost, it also allows reduced dilution and loss of mined ore, ultimately functioning when exploring high-grade minerals (Scoble and Moss, 1994). A typical representation of the cut and fill method is shown in Figure 2.4.

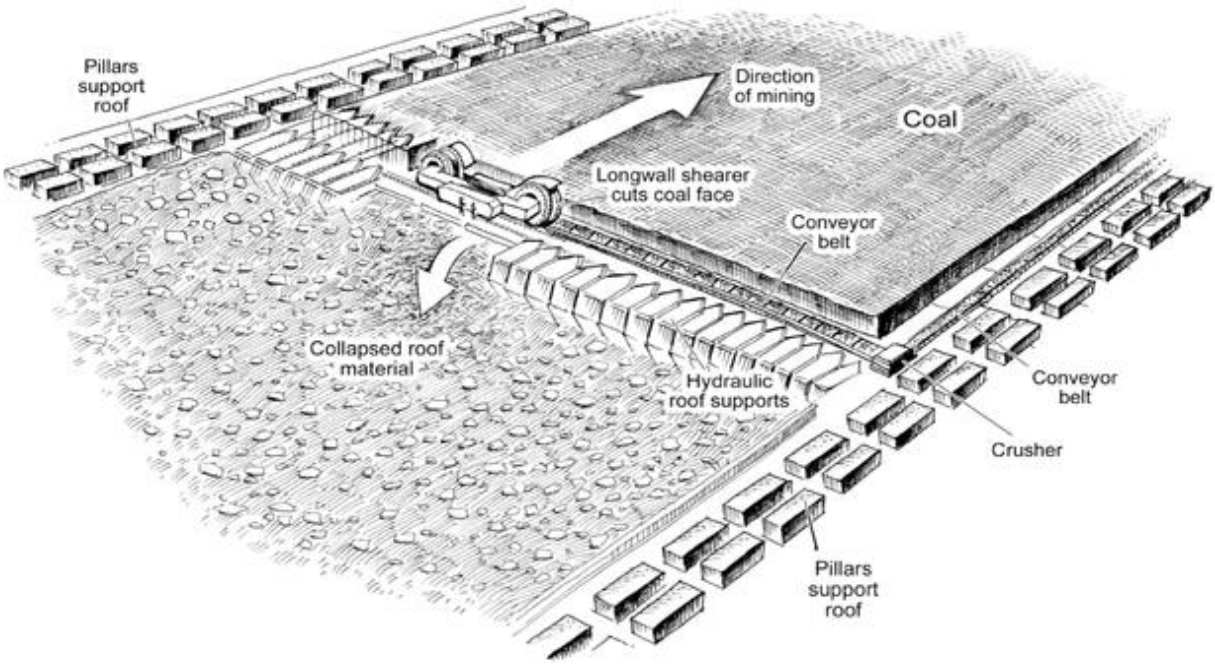

Figure 2.3 – Longwall mining method (US Securities and Exchange Commission, 1989).

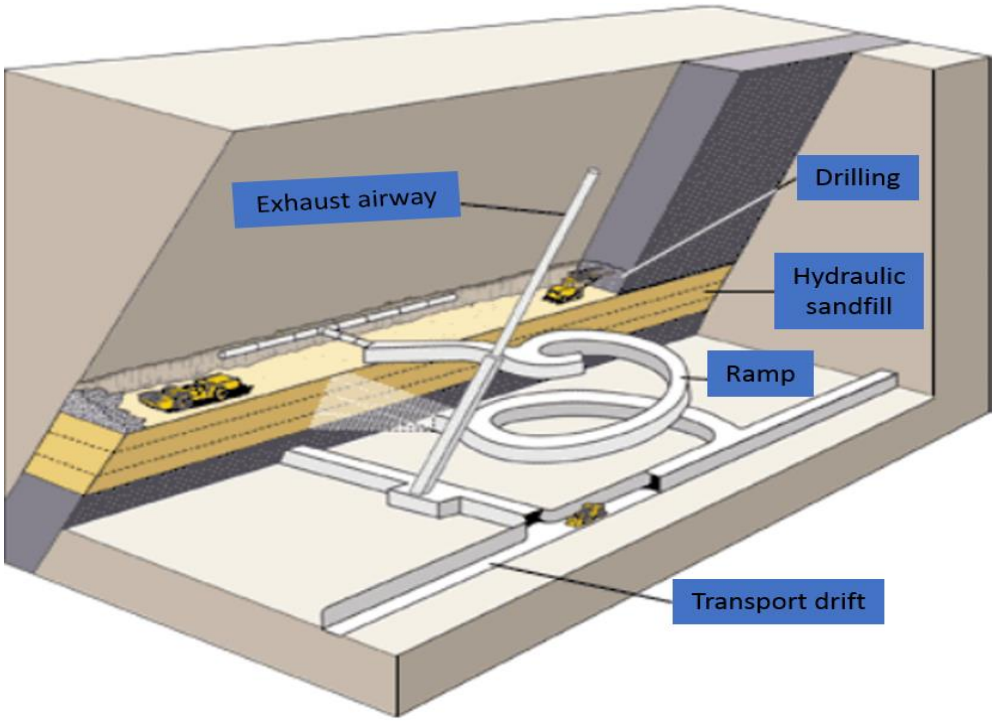

Figure 2.4 – Cut and Fill method using hydraulic fill technique (Adapted from Hamrin, 1997).

Only three different methods utilized in the mining field were discussed here, justifying Table 2.1 inclusion to this work as an informative resource adapted from the table provided by Dr. Hassan Z. Harraz. In this table, it is possible to encounter a summary of the methods employed in the mining sector with their respective significance factors.

Table 2.1 – Table of Methods for Underground Mining (Adapted from Harraz, 2010).

FACTORS / METHODS	ROOM AND PILLAR	STOPE AND PILLAR	SHRINKAGE STOPING	SUBLEVEL STOPING	CUT AND FILL STOPING	SQUARE SET STOPING	LONGWALL STOPING	SUBLEVEL CAVING	BLOCK CAVING
ORE STRENGTH	Weak / Moderate	Moderate / Strong	Strong	Moderate / Strong	Moderate / Strong	Weak	Any	Moderate / Strong	Weak / Moderate
ROCK STRENGTH	Moderate / Strong	Moderate / Strong	Strong	Fairly Strong	Weak	Weak	Weak / Moderate	Weak	Weak / Moderate
DEPOSIT SHAPE	Tabular	Tabular / Lenticular	Tabular / Lenticular	Tabular / Lenticular	Tabular / Irregular	Any	Tabular	Tabular / Massive	Massive / Thick
DEPOSIT DIP	Low / Flat	Low / Moderate	Fairly Steep	Fairly Steep	Fairly Steep	Any	Low / Flat	Fairly Steep	Fairly Steep
DEPOSIT SIZE	Large / Thin	Any	Thin / Moderate	Thick / Moderate	Thin / Moderate	Usually Small	Thin / Wide	Large / Thick	Very Thick
ORE GRADE	Moderate	Low / Moderate	Fairly High	Moderate	Fairly High	High	Moderate	Moderate	Low
ORE UNIFORMITY	Uniform	Variable	Uniform	Uniform	Variable	Variable	Uniform	Moderate	Uniform
DEPTH	Shallow / Moderate	Shallow / Moderate	Shallow / Moderate	Moderate	Moderate / Deep	Deep	Moderate / Deep	Moderate	Moderate

2.2. Backfilling Technologies

Backfilling technologies utilize the rock-solid waste (tailings) generated by the processing of raw ore from a mine to fill the underground stopes (Emad et al. 2015). Therefore, the mine backfill technology can also be used as an alternative to the surface disposal of mine solid wastes, and thus reduce the associated environmental issues (e.g., acid mine drainage) as addressed by Johnson and Hallberg (2005). Moreover, after placed into the underground openings, backfill materials are required to provide sufficient secondary ground support and thus facilitate pillar recovery and serve as a working floor for the underground mining worker and equipment. Due to the addition of binders, the rapid strength acquisition of mine backfill mass can significantly improve the

mechanical stability of surrounding rock mass and thus reduce the mining cycle time (Sheshpari, 2015). Therefore, mine backfill operation is becoming more popular in modern mines (Barrett et al. 1978). Based on mixture materials, the mine backfill methods can be classified into three categories including dry rock backfill, hydraulic backfill and cemented paste backfill.

Dry rock backfill utilizes rock wastes, dry tailings, gravel, and sand to fill the subterranean galleries formed after mining operations (Li, 2016). The mixture materials with different particle sizes can reduce the pore void space and increase the solid content. Moreover, through friction resistance between dry particles, the dry rock backfill can provide active support forces to stabilize the stopes (Sun et al. 2017).

Concerning the hydraulic backfill technology, it consists of tailings, water, and hydraulic binder. It is a slurry containing the water and tailings from the mine previously subjected to a centrifugation process. The centrifugation process is used to eliminate any slime trace formed in the tailings during storage and improve the density of the material. After reaching over 70% solids by weight ($\%_{CW}$) improved density, the hydraulic backfill is ready for most applications (Smith and Mitchell, 1982). The settlement of the coarse sediments happens quickly after the slurry is poured from the pipelines. Meanwhile, the excess water is accumulated on the surface of the consolidated layer due to the gravity effect (Fourie et al. 1994). The parameter that controls the transport of the slurry in the pipelines to avoid clogging issues is its solids by volume percentage ($\%_{CV}$). In the field, the values of $45\%_{CV}$ to $50\%_{CV}$ are commonly employed to fulfill the requirements (Cooke, 2001). The total water present in the backfill material depends on the tailings' residual water content and the required $\%_{CW}$ for a specific application. The permeability of the hydraulic fill together with the accumulated water on the surface of the poured material respond to the water drainage ratio (Borgesson, 1981). The practical porosity of a hydraulic fill with effective drainage is approximately 50%. After placement, the hydraulic backfill mass demands some hours to be walkable and one day to be opened for equipment transit (Pariseau and Kealy, 1972).

CPB is a complex and relatively new technology that is becoming more popular due to its applicability and competitive operation costs (Sheshpari, 2015). As CPB is the main material explored in this research work, the next section is reserved exclusively to discuss the CPB technology.

2.3. Cemented Paste Backfill (CPB)

CPB is used more commonly around the world in underground mines over the last decade (Xue et al. 2020; Cao et al. 2019; Wang et al. 2016). It is a mix of tailings (78 to 85% solid mass concentration), a binding agent (3% to 7% by weight of dry paste), and water that employs the development of bond hydration as its main strength gain mechanism (Belem and Benzaazoua, 2008). As well explained by Qi and Fourie (2019), the chemical reaction between the binding agent and water allows the solidification of water (bond hydration) inside a matrix mostly constituted by tailing particles, locking components together (C-S-H formation) and resulting in a more solid material with microscopic pores (reduced void size). Moreover, the application of CPB can reduce the ore loss and dilution and thus improve ore processing and ore recovery rate. A large amount of tailings is utilized into CPB preparation, and thus can be used as an effective alternative to mitigate surface tailings disposal. Consequently, CPB technology can significantly reduce environmental (e.g., acid mine drainage) and mechanical (tailing dam failure) catastrophes. Furthermore, during the preparation of CPB, the wastewater generated by mineral processing can be collected and reused (Edraki et al., 2014; Deb et al., 2017). CPB also enables higher stability during adjacent pillars excavation, improving operations safety together with production effectiveness as more material is explored (Belem et al. 2002). Therefore, mechanical stability has been considered to be a critical criterion for CPB design.

As mentioned before, the mechanical stability of CPB has been considered as a key design criterion of CPB structures after placed into stopes. CPB is also required to provide effective secondary ground support to prevent roof subsidence (Aubertin et al., 2013) and ensure the safety of underground mining workers (Cui and Fall, 2016a). Correspondingly, the material strength-based design approach (MS-DA) has been widely adopted for the design of CPB structures, which utilizes UCS as the main parameter. For instance, Brackebusch (1994) found that CPB with a cement content of 3% to 7% can achieve UCS from 700 to 2000 kPa. Belem and Benzaazoua (2008) experimentally investigated 28-day UCS and confirmed that a minimum UCS of 1000 kPa is required to maintain the stability of a free-standing wall while adjacent pillars are explored. Moreover, Grice (1998) also found that UCS values greater than 4 MPa are required to provide effective roof support. Additionally, to avoid the liquefaction process in early-age CPB, early-age UCS values greater than 150 kPa are needed (Bloss, 2002). US Environmental Protection Agency (1989) characterizes CPB as serviceable after its UCS reaches 345 kPa.

However, as mentioned before, the complex field loading conditions dominate the stress state in CPB structures. Correspondingly, the compressive, tensile, shear, and fracture behavior must be fully considered in the assessment of mechanical stability of mine backfill structure. Specifically, during pillar recovery processes (see Figure 2.5), the mine backfill mass is progressively exposed without the presence of confining pressure (free-standing wall scenario) (Yilmaz et al. 2015).

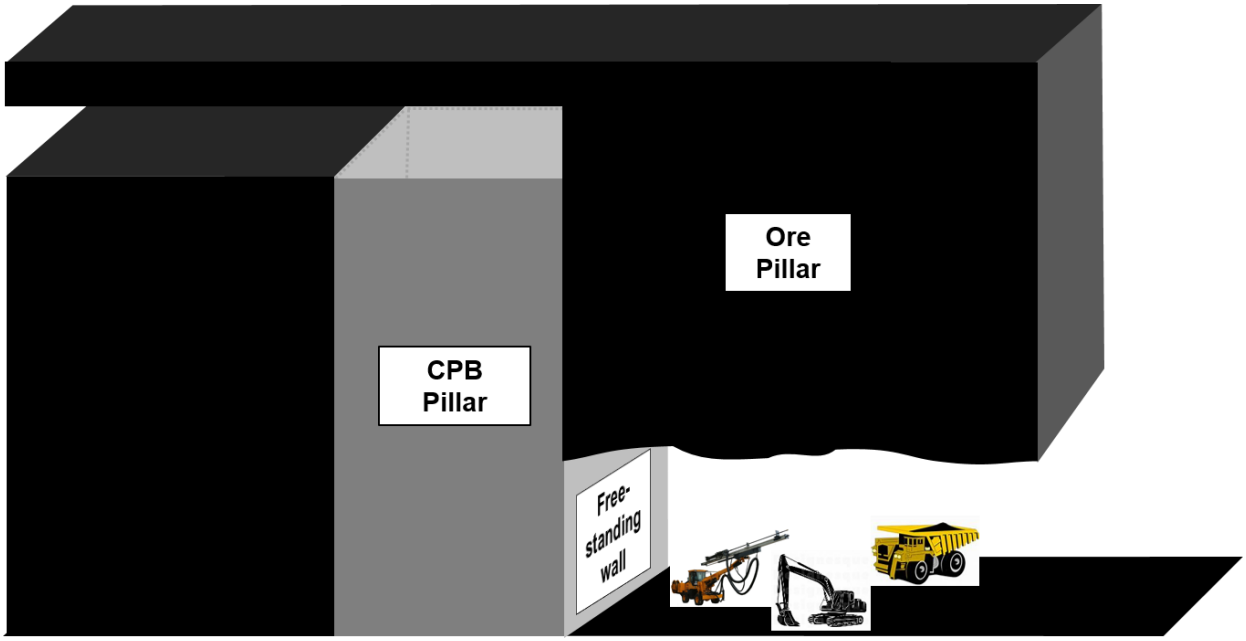

Figure 2.5 – Ore pillar recovery process and CPB free-standing wall.

Correspondingly, the UCS plays a critical role in the safe design of CPB structures. Apart from the UCS, tensile strength is another crucial design parameter for CPB. For example, in a deep underground mine with narrow and steeply dipping veins of ore, the underhand cut-and-fill stoping method is widely adopted (Johnson et al. 2015). Therefore, the massive CPB beam must provide sufficient tensile strength to ensure the safety of mining workers beneath it (see Figure 1.4). Moreover, the shear behavior of CPB also plays a critical role in the mechanical stability of the stopes backfilled with it. Specifically, as the ore pillars are progressively recovered, unequal principal stresses developed in CPB mass may cause shear failure, especially at high-stress conditions. Additionally, the shear behavior of CPB also governs the interface behavior between CPB and the surrounding rock mass (Figure 1.5). Due to the overburden pressure and consolidation process, the relative displacement occurs along the rock-CPB interface (Cui and Fall, 2017). Compared to the surrounding rock mass, the stiffness and strength of CPB are considerably smaller. As a result, the interfacial shear failure mainly occurs on the soft CPB side.

Furthermore, the traditional material strength-based design approach (MS-DA) assumes that intact construction materials exist before the application of field static and dynamic loadings (Harries and McNeice, 2006), which may result in an unsafe design. Specifically, stopes resulted from the production blasting possess rough rock walls (Liu et al., 2016). The rough rock walls own sharp convex and concave wedges along their surfaces at both microscale and macroscale. Therefore, after placement into a stope, the surface topography of soft CPB materials is governed by the rough rock walls and thus may result in randomly distributed micro- and macro-notches along the CPB surface. Consequently, when the CPB mass with pre-notched surfaces is exposed due to the extraction of adjacent pillars and subjected to field loading conditions, the stress concentration takes place near the notch tips. As a result, when the nominal stress acting on CPB is less than its design strength, the stress intensity factor may reach its critical value (i.e., critical stress intensity factor) and thus causes the crack initiation, propagation, and further regions segregation inside CPB mass. Therefore, the failure of CPB mass at macroscale can take place when the nominal stress is less than the design strength, which indicates an unsafe design methodology when opting for the conventional MS-DA.

Therefore, to yield a safe design for CPB structures, the fracture mechanics-based method is needed. Correspondingly, as the key fracture mechanics property, the fracture toughness is required to be determined. Due to the wide existence of tensile stress in CPB subjected to field loading conditions (Xu and Cao, 2018), mode-I (opening) fracture toughness (K_{IC}) plays a key role in the analysis of mechanical stability of CPB structure. As a type of cementitious material, the cement hydration contributes directly to the development of a cohesive strength component (Matallah et al., 2013). Therefore, CPB demonstrates strongly time-dependent behavior (Belem et al., 2010). Consequently, as the key factors associated with cement hydration, the effect of curing time and cement content on the fracture toughness are required to be identified. Moreover, the pore water is consumed during the cement hydration (Peyronnard and Benzaazoua, 2012), and thus results in the transition of CPB from a fully saturated state to an unsaturated state (i.e., self-desiccation process) (Cui and Fall, 2018a). Correspondingly, the development of matric suction affects the effective stress carried by the solid phase (Simms and Grabinsky, 2009) and thus the resistance to fracture initiation and propagation in CPB. Hence, the curing time, cement content and saturation state play crucial roles in the development of fracture toughness in CPB.

No studies have been conducted to systematically investigate the evolution of Mode-I fracture toughness and associated factors (curing time, cement content, and saturation state). Therefore, one of the objectives of this study is to experimentally investigate the effects of curing time (3, 7, 28, and 90 days), cement content (C_c=2%, 4.5%, and 7%), and saturation state (saturated and unsaturated state) on the evolution of mode-I fracture toughness of CPB through three-point bending tests.

2.4. Fiber-Reinforced Cemented Paste Backfill (FR-CPB)

To improve the mechanical behavior and performance of CPB, fiber reinforcement has been considered as a promising technique (Yi et al., 2015). The utilization of FR-CPB reduces the risks of local failures during mining operations due to improvements in mechanical properties and induced changes in failure patterns because of fiber inclusions (Chen et al., 2020).

A few experimental studies have been conducted to investigate the UCS development of FR-CPB. For instance, Mitchell and Stone (1987) confirmed that the inclusion of fiber can effectively improve the UCS of CPB and thus reduce the usage of cement that is more costly. Yi et al. (2015) found that FR-CPB with 5% cement and 0.5% fiber contents evidences an increase of 70-90% in UCS compared to CPB without fiber inclusion. Furthermore, other studies were conducted to assess the gains FR-CPB could deliver. Cao et al., (2019) pointed out how FR-CPB bears larger deformation and holds minor pieces in place after failure, delivering a safer operational environment. Yi et al. (2018) found that FR-CPB can enable higher heights of exposed walls, resulting in a reduction of the stopes required to mine an orebody.

The present limited experimental studies mainly focused on the identification of the effect of fiber inclusions on the compressive and tensile strength of FR-CPB. For example, to reveal the effect of fiber inclusion on tensile strength, Chen et al. (2019) conducted a series of indirect Brazilian tensile tests on FR-CPB specimens and found that the polypropylene fiber can substantially enhance the tensile strength and residual strength of CPB. Additionally, little attention has been paid to the shear behavior of FR-CPB. Based on the literature review, only one experimental study (Festugato et al., 2013) has been performed to investigate the cyclic shear response of FR-CPB at 14 days. Festugato et al. (2013) found that the inclusion of fibers increases the shear strength of CPB after successive load cycles.

Moreover, underground mining activities can reach a depth greater than 1000 meters (Marschalko et al., 2012). Due to the geothermal gradient (approximately 25°C to 45°C/km (Pourmalek and Shariatipour, 2019)), the mine backfill is commonly exposed to a warmer temperature in the deep underground excavations, curing under such conditions. As a type of cementitious material, FR-CPB properties and behavior are temperature-sensitive. For example, several experimental studies (Fall et al. 2010; Mbonimpa et al. 2019; Wu et al. 2013) have shown that the warmer curing temperature can increase the uniaxial compressive strength (UCS) of CPB. However, to the authors' knowledge, only one experimental study (Xu et al., 2019) was conducted to investigate the effect of warmer temperature on compressive behavior of FR-CPB, and found that higher temperature is able to further refine the pore structure and improve UCS of FR-CPB as well. Therefore, the thermal factor must be fully considered in the FR-CPB design, delivering better competitiveness to this technology.

Additionally, as indicated by Jianhua et al. (2019) and Di et al. (2020), the increase of curing humidity also exerts substantial modifications to the production of binder hydration products inside CPB, leading to the formation of a denser material matrix. However, not only temperature or humidity affect the behavior of CPB. The identification of the factors that affect CPB is a complex task because it relates to multiphysics processes (Ghirian and Fall, 2013; Ghirian and Fall, 2014). When FR-CPB is considered, this identification becomes even more complex since, apart from the multiphysics processes, a multiscale analysis (Kevorkian and Cole, 1996) should also be considered. Thus, this work mainly focused on the warmer curing temperature as it is a critical field condition present in all underground mines. Also, the majority of the previous researches was conducted on CPB subjected to room temperature, resulting in data that cannot be used to represent the actual underground mine scenario.

Very limited studies have been so far published on the effect of warmer temperature on the geomechanical behavior (compression, tensile, shear, triaxial, and fracture) of FR-CPB, which significantly affect the successful implementation of fiber reinforcement technique in the field. Therefore, this research aims to experimentally investigate the compression, tensile, shear, triaxial and fracture behaviors of FR-CPB cured under warmer temperature.

2.5. Summary

To enhance the ore recovery, particularly for the precious and rare metals, CPB (a high-density mixture of mill tailings, cement, and water) has been widely adopted in the underground mines and experienced rapid development in recent decades. Other than the environmental advantages (less waste dumped in surface-level reservoirs, reduced risks of generating ecological imbalance issues, and less water use) CPB can provide a safe and stable working platform for miners and mining equipment. Moreover, CPB may also serve as the excavation roof of access tunnels, enabling the passage of mining machinery and workers to the ore pillars. Therefore, the mechanical stability of CPB is a major concern for the successful implementation of backfill technology.

Acknowledging that underground mining happens thousands of meters below the surface level and that the temperature raises 25°C to 45°C per kilometer traveled in direction of the core of planet earth (geothermal gradient), fresh CPB is subjected to warmer curing temperature loadings in underground mine stopes. As a type of cementitious material, the temperature dependence of cement hydration inevitably influences the evolution of mechanical properties and behavior. Therefore, the temperature factor must be fully considered in the CPB design.

Furthermore, the inclusion of fibers into the mixture of CPB as a reinforcement, creating FR-CPB, has been considered as a promising technique to improve the geomechanical behavior of CPB. The preliminary studies on FR-CPB indicate that fiber inclusions can substantially enhance the UCS of backfill materials and thus further broaden its application possibilities in the mining industry.

However, compared to other cementitious materials such as concrete and mortar, CPB possesses some unique characteristics. First, CPB consists mainly of whole tailings particles, and thus possesses different characteristics of fiber-particles interaction. Moreover, as a type of temporary underground structure, the low cement content is commonly adopted to control the backfilling cost and yield a unique evolution of the geomechanical performance of CPB as curing time elapses. Additionally, the complex field loading conditions indicates the compressive, tensile, shear, and fracture behavior must be considered simultaneously. Therefore, when the fibers are introduced to the CPB matrix, the fiber-CPB matrix interfacial interaction will be significantly affected by the unique characteristics of CPB. Most importantly, as a key in-situ factor, the warmer curing temperature induced by the geothermal gradient can significantly affect the advancement of cement hydration, which indicates that the thermal factor must be fully considered in the

assessment of geomechanical behavior of FR-CPB. Therefore, it is necessary to conduct a comprehensive investigation regarding the geomechanical behavior of FR-CPB cured under warmer temperatures.

To reveal the effect of curing temperature, extensive experimental studies including laboratory tests, monitoring programs, and auxiliary laboratory analyses were conducted. The constitutive behavior and mechanical properties were determined, and the associated evolutionary characteristics and controlling mechanics were identified. Moreover, this study also established a series of predictive models to estimate the variation of geomechanical properties of FR-CPB. Therefore, the obtained results form this cannot only improve the understanding of the geomechanical behavior of FR-CPB but also contribute to the successful implementation of fiber reinforcement in CPB technology.

Chapter 3 Materials and Methods

3.1. Introduction

This study aims to investigate the geomechanical behavior of FR-CPB subjected to various curing temperatures. To achieve the research objectives, extensive experimental investigations were conducted. To demonstrate the laboratory studies in this thesis, the chapter will first present the detailed information about the testing materials and equipment in Section 3.2 and 3.3, respectively. Then, the mixture recipe and associated specimen preparation will be discussed in Section 3.4. After that, the detailed laboratory study program will be presented in Section 3.5. The information about scanning electron microscope observation, chemical shrinkage measurement, and dry density determination will be summarized in Section 3.6 followed by the summary in Section 3.7.

3.2. Materials

CPB and FR-CPB specimens were prepared through a mixture of quartz tailings, General Use Portland Cement, fiber insertions, and tap water.

3.2.1. Cement and mixing water

General Use Portland cement was used as a binding agent, which has been widely adopted in CPB formulations due to its availability and versatility (Tariq and Yanful, 2013). The compound compositions are presented in Table 3.1. The tap water was used as mixing water. The chemical elements present in the tap water are summarized in Table 3.2.

Table 3.1 – Composition of General Use Portland Cement (GU).

Composition	Al_2O_3	SiO_2	Fe_2O_3	FeO	MgO	CaO	Na_2O	K_2O	TiO_2	P_2O_5	MnO
Content (%)	3.74	46.71	4.24	3.81	1.73	35.24	0.36	2.90	0.72	0.37	0.15

Table 3.2 – Chemical elements present in mixing water.

Chemical element	Ba	Ca	Cu	K	Mg	Na	S	Si	Sr
Content (ppm)	0.01	14.50	0.01	0.55	3.00	7.29	1.30	1.07	0.03

3.2.2. Tailings

The quartz tailings (silica) were used as tailings materials. The chemical compositions of quartz tailings are listed in Table 3.3. It can be found that the quartz tailings consist of 99.7% silicon dioxide which is the major mineral found in hard rock mines in Canada (Cui and Fall, 2018b). Moreover, it is well known that there exist various types and content of sulfide (e.g., pyrite and pyrrhotite) in the natural tailings, which may inhibit the progress of cement hydration (Yan et al., 2020). Therefore, to identify the critical role played by cement hydration in the development of fracture toughness, the chemically inert silica can effectively minimize the uncertainties associated with natural tailings. Based on the particle size analysis of quartz tailings (Figure 3.1), the D-values (D_{10}, D_{30}, and D_{60}), the coefficient of uniformity (C_U=D_{60}/D_{10}), and the curvature coefficient (C_{Coef}=D_{30}^2/(D_{10}×D_{60})) were determined and tabulated in**Error! Reference source not found.**.

Table 3.3 – Chemical composition of quartz tailings.

Composition	Al_2O_3	SiO_2	Fe_2O_3	FeO	MgO	CaO	Na_2O	K_2O	TiO_2	P_2O_5
Content (%)	0.17	99.70	0.03	0.024	0.01	0.02	0.01	0.02	0.02	0.01

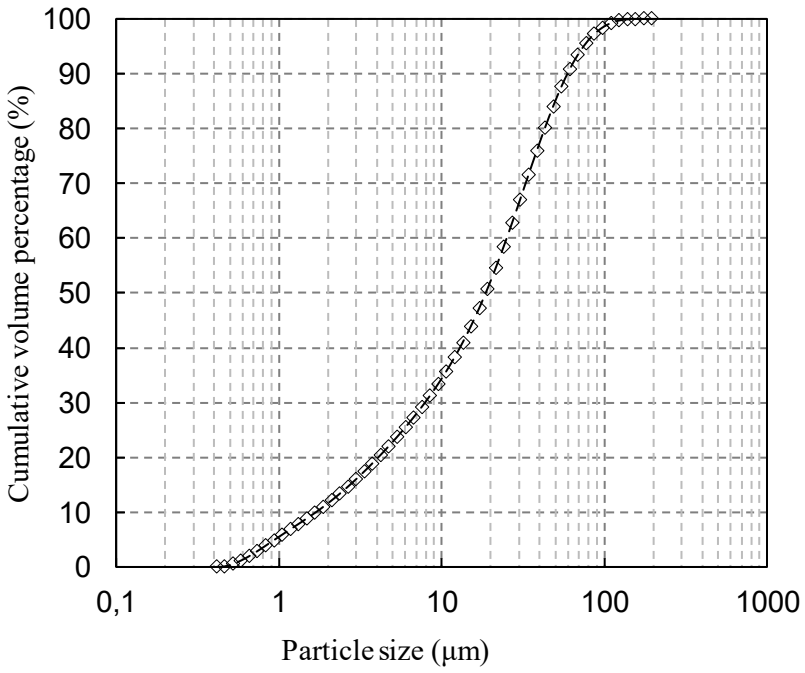

Figure 3.1 – Particle size distribution of quartz tailings.

Table 3.4 – Particle size distribution parameters of quartz tailings.

D_{10} (μm)	D_{30} (μm)	D_{60} (μm)	C_U (-)	C_{Coef} (-)
1.87	8.47	25.67	13.72	1.50

-: dimensionless

3.2.3. Polypropylene Fibers

Polypropylene monofilament microfibers (PSI Fiberstrand MultiMix 80) with 13-mm length were bought from Euclid Chemical group (boxes containing 45 bags with 0.3 kg of fibers each) to be introduced into the FR-CPB mixture. The fibers not only follow ASTM C1116 specifications and requirements necessary for applications related to fiber-reinforced concrete and shotcrete but also comply with the code that regulates synthetic fibers utilization (ICC ES AC32), implicating negligible changes concerning FR-CPB utilization since both concrete and CPB are cementitious materials. Table 3.5 summarizes the properties of the employed fibers.

Table 3.5 – Polypropylene fibers properties list.

Properties List (Unit)	**Value**
Specific Gravity (-)	0.91
Dosage Rate (kg/m^3)	0.3
Length (mm)	13
Diameter (μm)	54
Melt Point (°C)	160
Electrical and Thermal Conductivity (-)	Low
Water Absorption (-)	Negligible
Acid and Alkali Resistance (-)	Excellent

-: dimensionless

3.3. Tools and equipment pieces

To mix CPB and FR-CPB in the laboratory, a KitchenAid Pro 5 Plus Stand Mixer (Figure 3.2) was employed to conduct all mixing procedures. Hard plastic molds from Hoskin Scientific were used

as containers to store and cure specimens until the required curing time was reached. Figure 3.3 showcases the dimension of the molds employed in this study.

Figure 3.2 – KitchenAid Pro 5 Plus Stand Mixer.

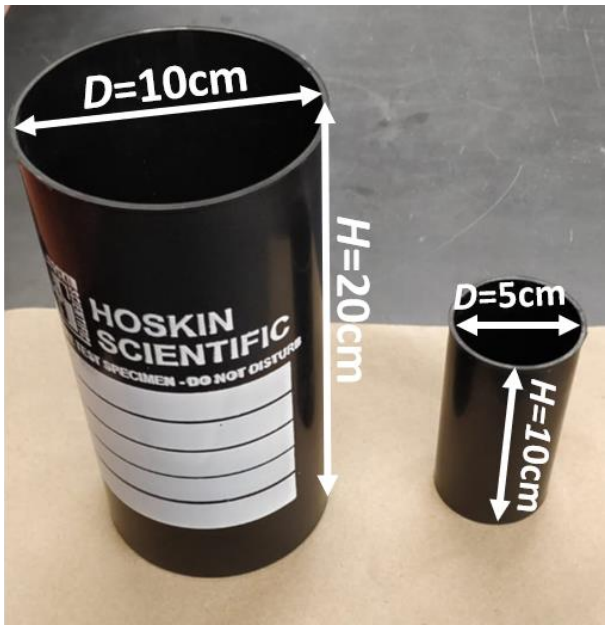

Figure 3.3 – Large and small molds dimensions.

To prepare the specimens in accordance with the testing procedures requirements, a 12" Glide Miter Saw with diamond masonry blade was used to trim and shape the specimens. Figure 3.4 shows the miter saw utilized.

Figure 3.4 – BOSCH Mitre Saw (The Home Depot Canada).

Additionally, distinct laboratory tests required distinct loading frames due to specific testing conditions or specific system placement inherent to the laboratory facility. In this study, three loading frames were used. The first frame, a T57 Compression Test Machine (Figure 3.5) fabricated by Wykeham Farrance Eng. LTD., with a capacity of 5 tons was employed to conduct Unconfined Compressive Strength, Tensile and Three-Point Bending tests.

Figure 3.5 – Wykeham Farrance T57 Loading Frame.

The second frame, a Direct Shear Apparatus (EL28-007 series), manufactured by ELE International, with the capacity of 1-ton normal load acting on the sample was combined with its shear box device and used to perform the Direct Shear tests. Both the direct shear frame and shear box are presented in Figure 3.6 as a) and b), respectively.

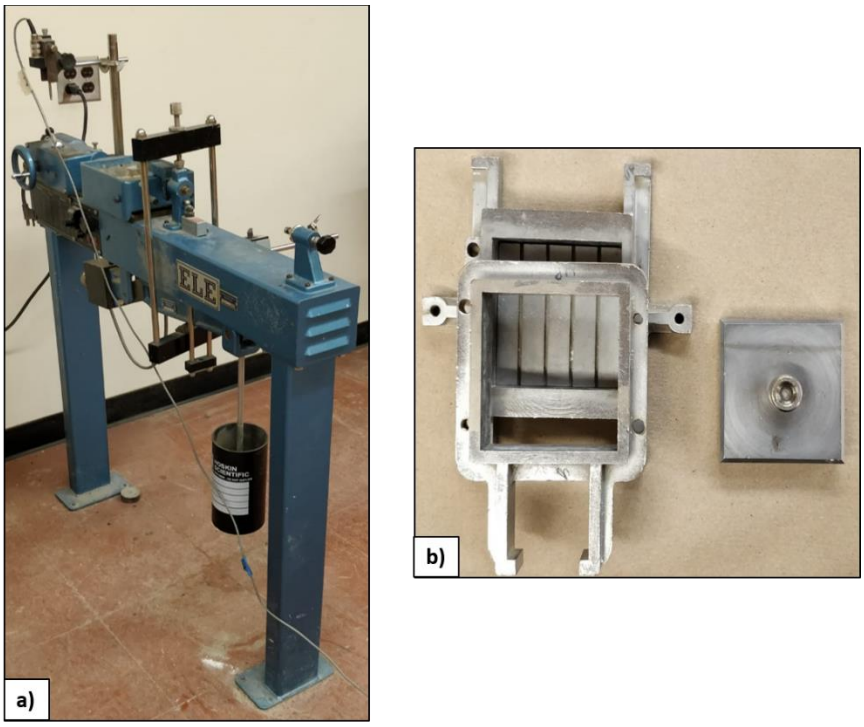

Figure 3.6 – Direct Shear Test a) load frame and b) shear box.

The third frame is shown in Figure 3.7. It is a Digital Tritest 50, also manufactured by ELE International with 5-tons capacity and was employed to operate triaxial tests on the samples.

Figure 3.7 – Triaxial Test Load Frame.

Lastly, some sensors were configurated and calibrated to electronically read and store the data obtained during tests. A 1000 pounds capacity load cell from ARTECH Industries Inc. collected readings referent to the loading applied to the samples. Moreover, 25-mm Linear Variable Differential Transformer (LVDT) sensors from A-Tech Instruments Ltd. were employed to store displacement measurements during tests. The calibration of the sensors followed the manufacturer`s specifications and guidebook. Initial assessment measurements were contrasted against the values obtained from a displacement calibration reference device (VJ Tech DSC 2000 calibration) to ensure the differences were minimal and in the order of three decimal places. Both load cell (strain gauge) and LVDTs (high-level) were connected to a data logging system that was integrated into a central computer with StrainSmart software installed. The software enabled the merging and monitoring of collected data from the sensors, creating the behavioral curve of the tested material in real-time. Figure 3.8 depicts the load cell and the LVDT adopted in this study.

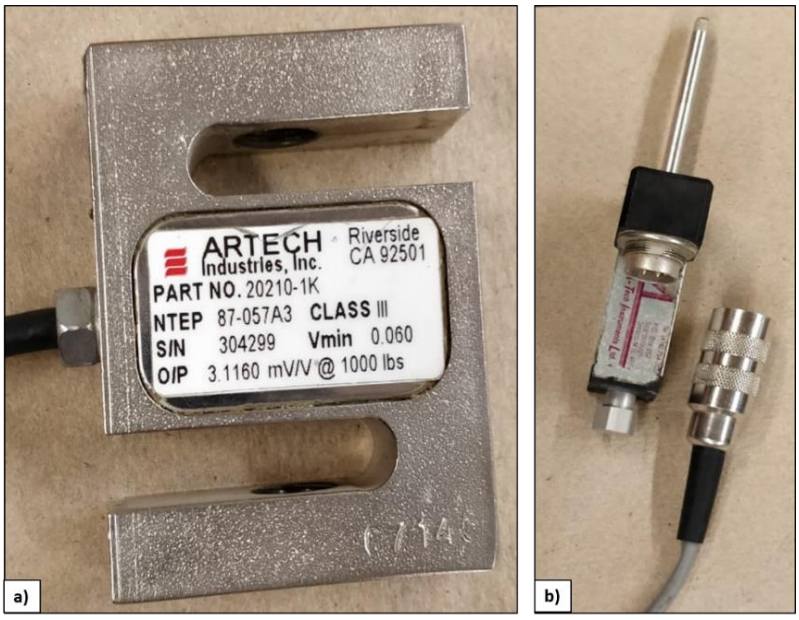

Figure 3.8 – Data collecting sensors: a) Load cell; b) LVDT.

3.4. Mixture Recipe and Specimen Preparation

3.4.1. Mixture Recipe

In this study, a 4.5% cement content, a 7.6 water-to-cement ratio (w/c), and a 0.5% fiber content (from total solid phase), together with 13-mm length polypropylene fibers, were the non-variable parameters adopted to mix all FR-CPB specimens. CPB specimens were also cast with the same

values of cement content and water-to-cement ration, but no fibers were included. This way, CPB specimens acted as the control group.

The mixture process followed ASTM C192 as a reference since CPB or FR-CPB possesses no standardized specimen casting procedures. To cast the specimens, a dry mix using only the solid materials (tailings and cement with or without fibers) was conducted for five minutes before adding the water content and mixing for more eight minutes (wet mix). Figure 3.9 illustrates the dry and wet mixing processes.

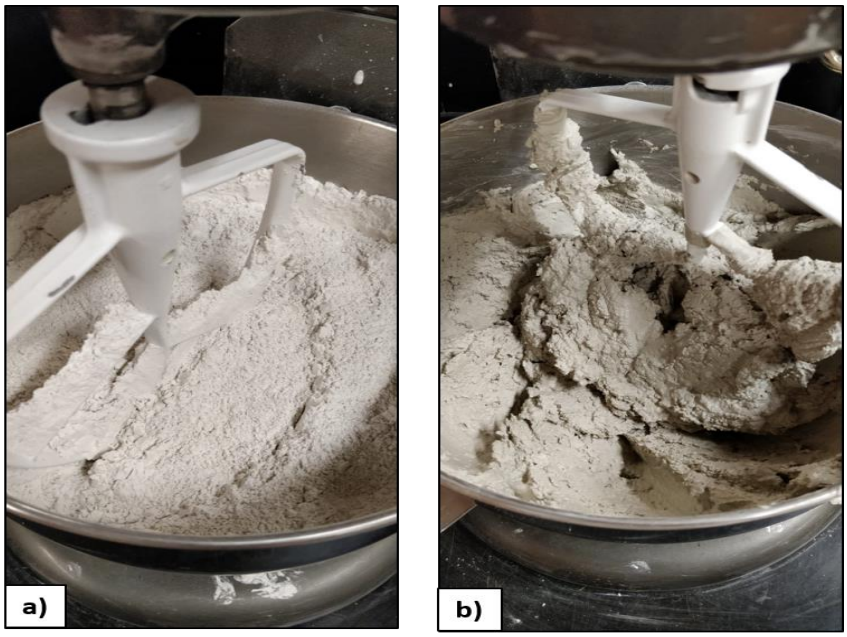

Figure 3.9 – Different mixes present during mixing procedures: a) Dry mix; b) Wet mix.

After mixed, the paste was poured into large or small molds (Figure 3.3) accordingly to the casting schedule and cast on three layers. Each layer was cast using the same procedures, rodded 25 to 30 times, tapped on the sides 12 to 15 times obeying a deflection of 90º after each set of 3 lateral taps, and hit 20 times against the counter to remove the entrapped air inside the paste. After casting the last layer, the mold surface was scraped 12 times obeying 90º revolution after each pass of the spatula to deliver better surface control. Then, the mold was covered with the lid, sealed with tape to avoid water from scaping (undrained conditions), and left to cure under room temperature (approximately 20°C), 35°C, and 45°C for 7, 28, and 90 days. Once the curing time was reached, a drill was used to create a little perforation on its bottom to allow air pressure to enter and help in the demolding process.

3.4.2. Specimen Preparation 1: Unconfined Compressive strength (UCS) Tests

UCS tests required the utilization of small molds (5cm diameter by 10cm height). After the demolding process, UCS specimens` top and bottom initial layers were trimmed 2mm using the miter saw to guarantee a precise flat contact between the sample and the loading frame. Once the trimming process was finalized, the testing could start. Figure 3.10 showcases a specimen used in a UCS test.

Figure 3.10 – UCS Test specimen.

3.4.3. Specimen Preparation 2: Splitting Tensile Strength (STS) Test

STS tests used large samples (10cm diameter by 20cm height) that, after removed from molds, had their bottom surface trimmed 2cm to avoid performance problems related to the demolding process. After the removal of the 2cm layer, disc-shaped specimens were cut obeying 5cm intervals starting from the bottom. This specimen preparation process enabled retrieving three disc-shaped specimens of 10cm diameter by 5cm height per large mold and those were the ones tested to obtain the STS of CPB and FR-CPB. Figure 3.11 illustrates the final specimen used in STS tests.

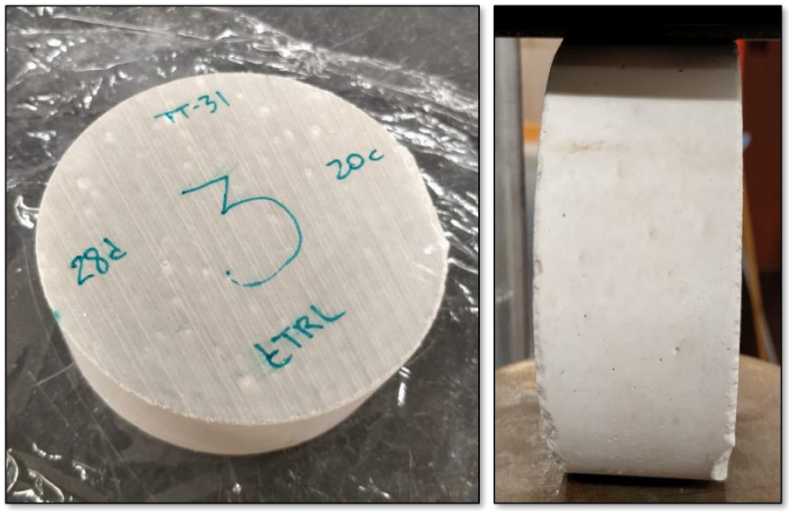

Figure 3.11 – STS Test specimen.

3.4.4. Specimen Preparation 3: Direct Shear (DS) Test

DS tests used squared samples with 6cm by 6cm surface area and 3cm height. These specimens were shaped from disc-shaped specimens with 3cm height. Similar to the STS specimen preparation procedures, large samples were taken from their molds and trimmed 2cm starting from the bottom. However, this time the interval applied between cuts was 3cm which resulted in five disc-shaped specimens of 10cm diameter and 3cm height per large sample. The layer close to the surface of the mold was never used to diminish any chance of uncertainties. With the help of the pieces that constitute the shearing box device, a 6cm by 6cm square was drawn on the surface of the disc-shaped specimens and vertical cuts following the square boundaries were executed to shape the disc specimen into a squared specimen. The squared specimens with 6cm of length, 6cm of width, and 3cm of height were the ones tested and are shown in Figure 3.12.

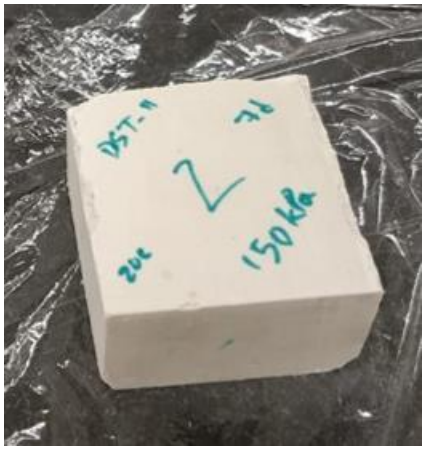

Figure 3.12 – DS Test Specimen.

3.4.5. Specimen Preparation 4: Triaxial Test

The preparation of the triaxial specimens started with a procedure similar to the one employed in UCS test specimens` preparation. The specimens were removed from the mold and trimmed 2mm on top and bottom surfaces. After trimmed, the specimens were placed into a tank filled with cold water and 101 kPa of negative pressure was applied to them for one hour to re-saturate the specimens. After one hour, the specimens were ready to be tested (Figure 3.13). More details about this re-saturation process will be presented in Section 3.5.3.

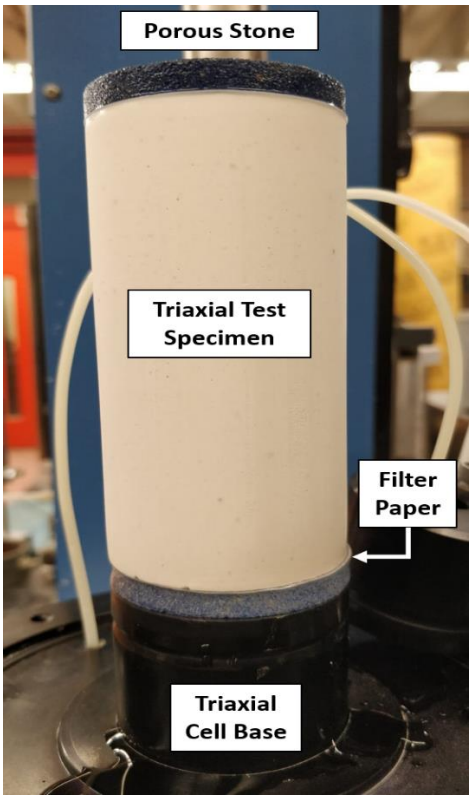

Figure 3.13 – Triaxial Test specimen.

3.4.6. Specimen Preparation 5: Three-Point Bending (TPB) Test - CPB Beam Specimens

Samples from the large molds were used to prepare CPB beam specimens. Once the curing time was reached, the sample was cut into two halves and each half was downed to a small beam with 20cm of length (L), 2.27cm of width (B) and 4.55cm of height (W) using the miter saw in the laboratory. After shaped into a beam, the specimen received a central 1-mm wide notch of 2.27cm length (a). Figure 3.14 depicts the beam sample used in TPB tests.

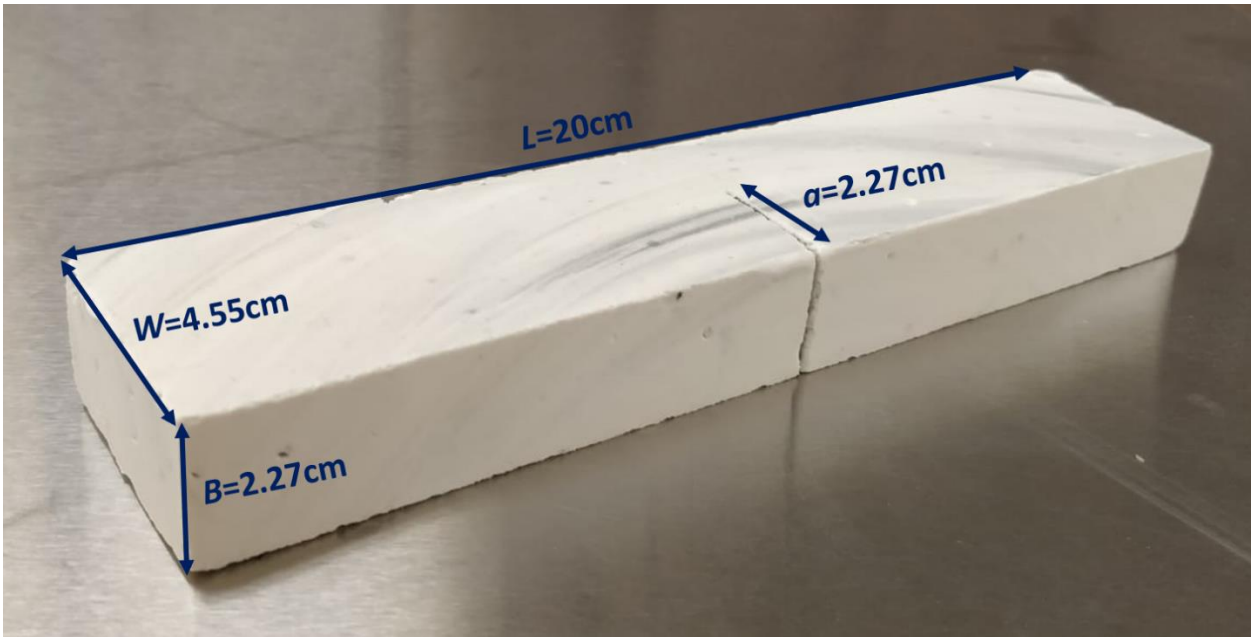

Figure 3.14 – TPB Test beam specimen.

3.4.7. Specimen Preparation 5: Three-Point Bending (TPB) Test – Semicircular Bend (SCB) FR-CPB Specimens

A sample from a large mold was also employed here. The last 2cm from the bottom was removed and, to retrieve specimens from it, perpendicular cuts following 5cm intervals along its 20-cm length were executed. The obtained disc-shaped samples with 10cm diameter and 5cm height were then divided into two halves (Figure 3.15) and pre-notched in the center following angles of 0°, 30° and 54° relative to the vertical axis (Figure 3.16 (a), (b), and (c), respectively). After cutting the notch, the specimen was ready to be tested.

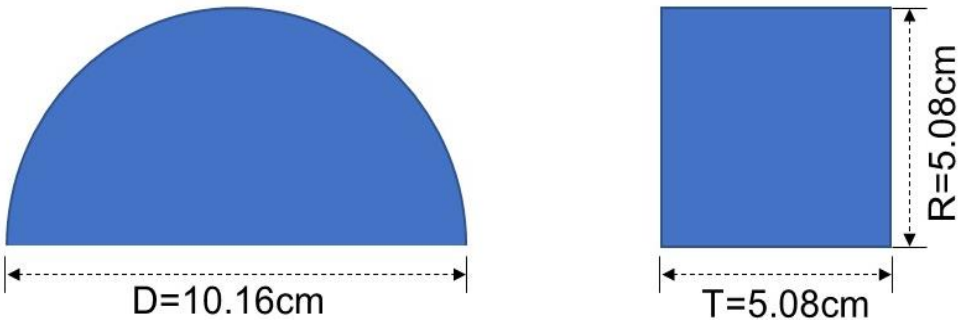

Figure 3.15 – SCB FR-CPB specimen.

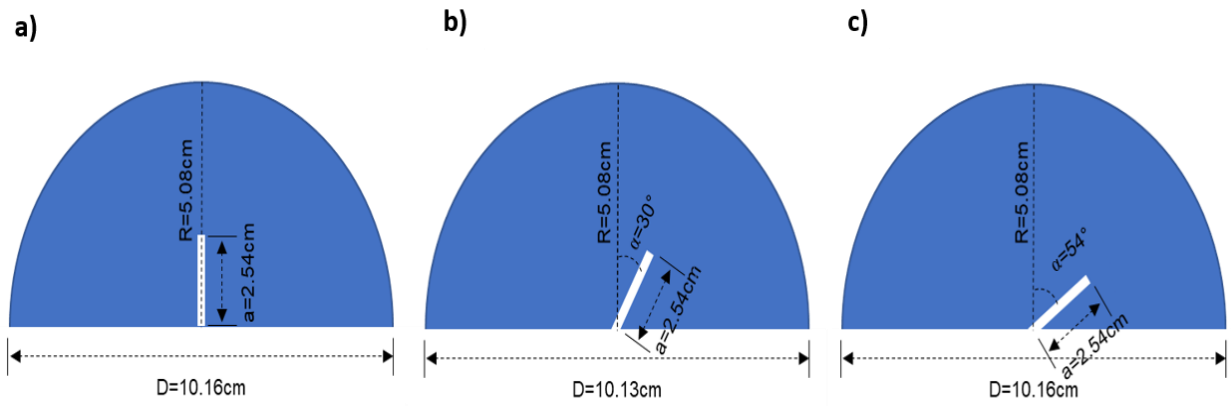

Figure 3.16 – Pre-notch positions (α: notch angle w.r.t. from the vertical line along radius): (a) mode I specimen used to determine K_I; (2) mixed-mode (I+II) specimen used to determine K_{eff}; and (c) mode II specimen used to determine K_{II}.

3.5. Experimental Study Program

3.5.1. Mold-based monitoring program

The chemical reaction between cement and water inside CPB or FR-CPB structures develops a porous matrix with microscopical voids as they transcend from its initial fully saturated state to a dryer and more solid state, consuming the water present in the materials` medium. This phenomenon induces a high matric suction, allowing the measurement of CPB or FR-CPB saturation state. Additionally, it is known that the cement hydration development in CPB is easily identified by electrical conductivity observations as the charges in the material`s matrix behave according to the evolution of the electric field inside (Cui and Fall, 2016b).

Therefore, a mold-based monitoring program was created to identify and record the progress of the matric suction and electrical conductivity of FR-CPB specimens cured under 20°C, 35°C, and 45°C during 90 days. 5TE (electrical conductivity) and T5X tensiometer (matric suction) sensors together with a data-logging system (ZL6) were employed to successfully enable data acquisition. Figure 3.17 showcases a sketch of the experimental setup of the monitoring program.

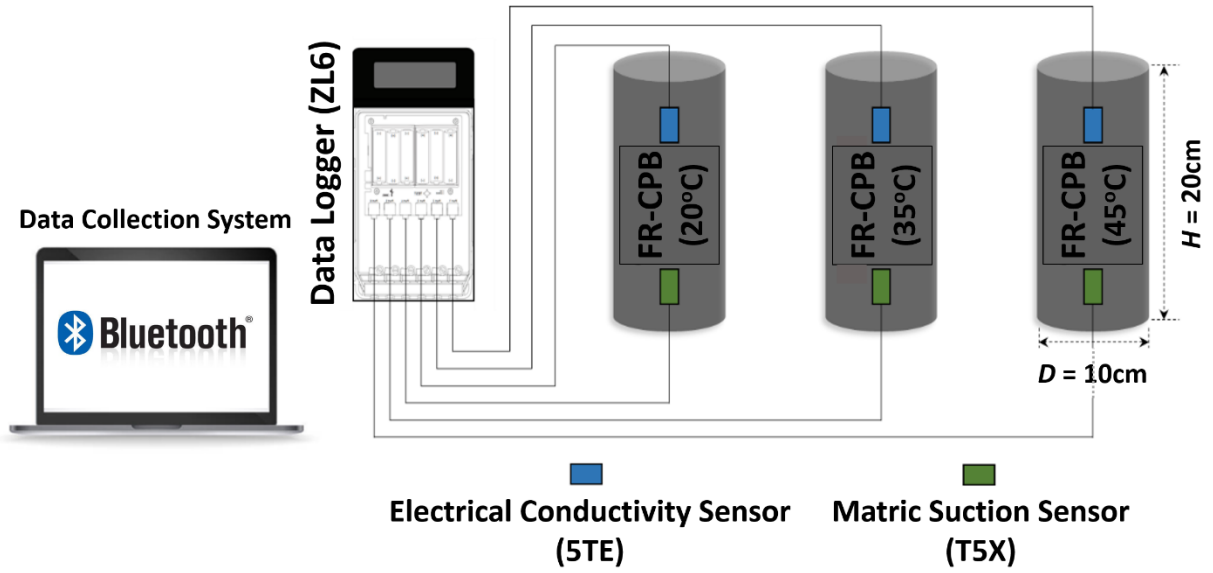

Figure 3.17 – Mold-based monitoring program configuration.

3.5.2. Unconfined Compressive Strength (UCS) Test

To study the compression performance of FR-CPB cured under warm temperatures, UCS tests were conducted on FR-CPB and control CPB specimens according to ASTM C39 since this backfilling technology possesses no standard guide yet. Temperatures of 20°C, 35°C, and 45°C were applied to the samples while they cured for 7, 28, and 90 days. The displacement rate was set to 1mm/minute on the T57 load frame and an LVDT (25-mm capacity) together with the load cell (1000-lbs capacity) were used to record axial displacement and the axial load, respectively. The measured data was collected by a data logging system and combined in a single file using StrainSmart software.

Once testing was finalized, the files were exported as excel files, allowing the start of data processing referent to the specimens` compressive strength performance. To obtain the peak compressive strength and compressive performance curve of the material, the calculations for UCS values followed the equation below:

$$UCS = \frac{4000\ P_{max}}{\pi D^2} \quad (1)$$

Where,

UCS: unconfined compressive strength (MPa);

P_{max}: maximum load (peak value of stress-strain curve) (kN);

D: averaged diameter of the specimen (mm).

To improve the accuracy and reproducibility of the UCS tests, three replicate specimens were tested for each curing time. Based on the obtained results from UCS tests, the material parameters (UCS value, secant modulus (E_{50}), and compression behavior (stress-strain curve)) were retrieved from the processed raw data. Figure 3.18 illustrates how the previously mentioned properties are showcased in this work and how they can be identified to enable a clear comparison between different results.

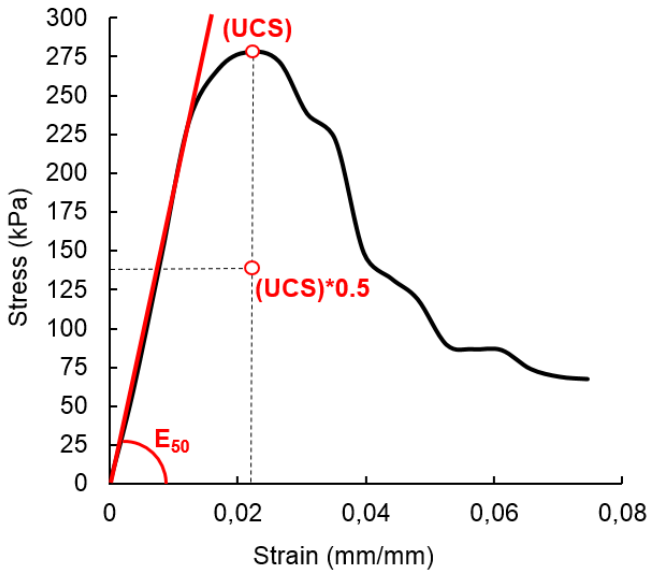

Figure 3.18 – Parameters obtained from an UCS test.

3.5.3. Splitting Tensile Strength (STS) Test

Based on ASTM 3967 (rock material), STS tests were conducted on FR-CPB and control CPB specimens subjected to warm temperature curing. When the targeted curing time (7, 28, and 90 days) was reached, the specimens under 20°C, 35°C, and 45°C were taken out from their molds and trimmed into disk specimens as mentioned in Section 3.3.3. For each curing time, STS tests were performed a minimum of three times to ensure repeatability of testing results. The adopted load cell, LVDT, data acquisition system, and StrainSmart software were also employed in this testing procedure.

After all the data was exported into Excel format files, the tensile performance investigation could start. Through the experimental data from STS tests, the tensile performance (stress-displacement curve) and material stiffness (slope of straight-line portion of the stress-displacement curve) could be obtained. With respect to the calculation method used to obtain STS values from tests, the following equation was the one used:

$$\sigma_t = \frac{2P_{max}}{\pi t D} \quad (2)$$

Where,

σ_t: splitting tensile strength (MPa);

P_{max}: maximum load (peak value of the stress-displacement curve) (N);

t: the thickness of the specimen (mm);

D: diameter of the specimen (mm).

3.5.4. Direct Shear (DS) Test

According to ASTM D3080 (soil material), a series of direct shear tests was conducted on FR-CPB and control CPB specimens to investigate the effect of warm temperature curing on their shear strength. Temperatures of 20°C, 35°C, and 45°C together with curing times of 7, 28, and 90 days were adopted. Also, three different normal stresses of 50, 100, and 150kPa were applied to the specimens during testing procedures and three specimens were tested for each curing time to ensure the accuracy of results.

The tests were conducted at a shearing rate of 1.0 mm/minute, with a maximum horizontal displacement of 8mm. During the tests, the horizontal and vertical displacements were respectively measured by two displacement transducers. The load cell was used to record the shear stress in the horizontal direction. The data logging system was utilized to collect the data from the sensor and the StrainSmart software used to organize and export the data files.

After exporting the data as excel-format files, the data processing operation started. This time, the data analysis aimed to investigate the shear performance of the material through obtaining the material`s shear stress-displacement curve and further evaluation of its hardening and softening sections. Also, cohesion and friction angle (shear strength parameters) were evaluated concerning each test performed. Therefore, the following equation governed the shear strength calculations, applying corrections to the area as the horizontal development developed:

$$\tau = \frac{F_x}{A} \quad (3)$$

Where,

τ: nominal shear stress (kPa);

F_x: shear force (kN);

A: surface area of the specimen (m^2) – must be corrected as the horizontal displacement increases.

3.5.5. Triaxial Test – Consolidated & Undrained (CU)

ASTM D4767 (soil material) was used as a reference to perform CU triaxial tests over FR-CPB and control CPB specimens to further investigate the impact of warm curing in the material`s properties and behavior. The temperatures employed were 20°C, 35°C, and 45°C together with 3-, 7-, and 28-day curing times. Additionally, three distinct confining pressures of 25, 50, and 75 kPa were applied to the 3-day specimens, changing to 50, 100, and 150 kPa for the 7-day and, lastly, applying 100, 200 and 300 kPa once a 28-day sample was tested. A total of three specimens were tested per curing time to guarantee the replicability of results.

A displacement ratio of 1mm/minute was adopted to conduct the tests and a maximum vertical displacement of 12mm was established. For this test, the 1000-lbs capacity load cell was used to measure the principal stress difference (deviator stress) applied and an LVDT was used to monitor the progress of the vertical displacement. Additionally, a pressure transducer and a volume change device were used to enable readings regarding pressure and volume changes as the loading subjected to the specimen increased. Before any test started, all the specimens were subjected to a re-saturation process for one hour employing the method discussed in Section 3.5.3.

The pressure transducer, from OMEGA Engineering, was calibrated and coupled to the triaxial load cell as shown in Figure 3.19. The volume change device, from VJ Tech, was connected to the channel related to the top region of the specimen and received an LVDT sensor to acquire the movement of its central piston indicating the volume change inside the specimen (Figure 3.20). A data logging system was connected to the load cell, to the LVDT measuring vertical displacement, to the pressure transducer, and to the LVDT coupled to the volume change device, receiving all the information from the data acquisition process. Then, the data was sorted by the StrainSmart software and exported in excel format to allow the respective analysis.

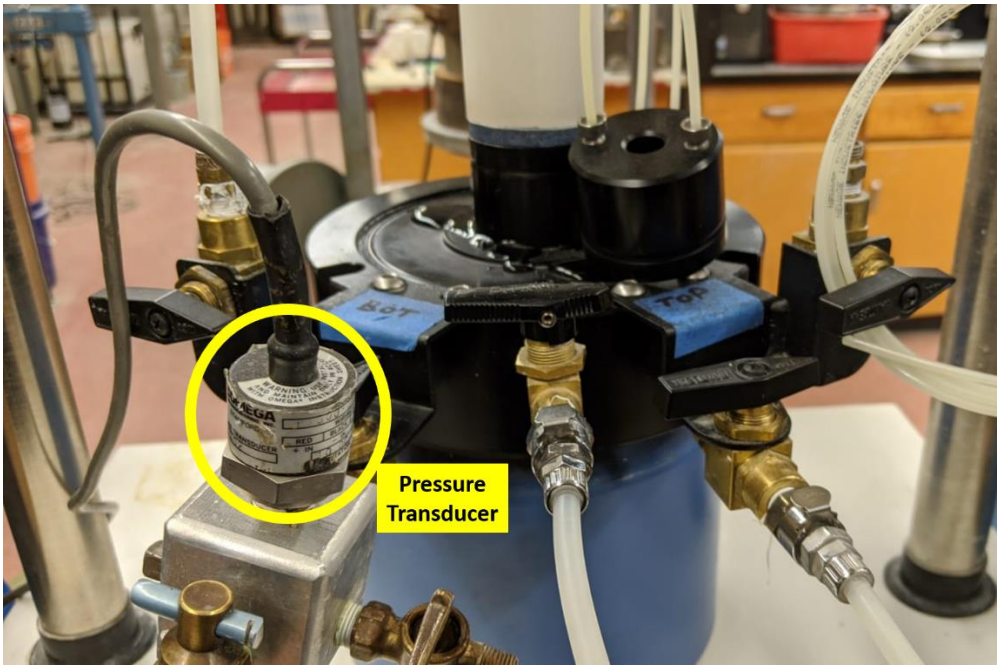

Figure 3.19 – Pressure Transducer coupled to the Triaxial cell.

Figure 3.20 – Volume Change Device.

The objective of the data analysis was to acquire the stress-strain curves of FR-CPB specimens subjected to warmer temperature curing and monitor variations of the pore water pressure and volume. Hence, the following equations and parameters were employed to enable the calculations and further development of the stress-strain curves:

$$(\sigma_1 - \sigma_3) = \frac{P_a}{A} \tag{4}$$

Where,

($\sigma_1 - \sigma_3$): measured principal stress difference or deviator stress (kPa);

P_a: given applied axial load (kN);

A: corresponding cross-sectional area (m^2).

3.5.6. Three-Point Bending (TPB) Test – Beam Specimen Method

According to ASTM D5045 (plastic material), the critical stress intensity factor (i.e., fracture toughness), K_{Ic}, was determined by the three-point bending (TPB) tests. To prepare the pre-notched beam specimen, the cylindrical CPB specimens obtained from plastic molds were trimmed when the target curing time (3, 7, 28, and 90 days) was reached as specified in Section 3.3.6. Per curing time, three specimens were used to comply with the data accuracy parameters utilized in this work. Additionally, this method was employed to investigate fracture toughness changes resultant from distinct cement content values (2%, 4.5%, and 7%). As shown in Figure 3.21, the test specimen has a thickness (B) of 2.27cm, a width (W) of 4.55cm (i.e., W=2B), a length of 20cm, and a crack length (a) of 2.27cm (i.e., a/W=0.5).

During the TPB tests to obtain the material`s fracture toughness, a high-precision digital force gauge (model: SHIMP FG3005, capacity: 50N, resolution: 0.05N) was employed to measure the vertical load (P), and a displacement transducer was used to recall the loading point displacement (u). A loading rate of 1mm/min was adopted in the present study. Also, EDMS Data Acquisition software stored, organized, and exported the data files to enable the data analysis process. Based on the obtained testing results, the mode-I fracture toughness, K_{Ic}, was calculated from the following relationship:

$$K_k = \frac{6P_m\sqrt{a}}{BW}\left\{\frac{1.99 - \frac{a}{W}\left(1 - \frac{a}{W}\right)\left[2.15 - 3.93\frac{a}{W} + 2.7\left(\frac{a}{W}\right)^2\right]}{\left(1 + 2\frac{a}{W}\right)\left(1 - \frac{a}{W}\right)^{\frac{3}{2}}}\right\} \tag{5}$$

Where,

P_m: peak load from TPB test ($Pa \cdot m^{1/2}$);

B: thickness of the specimen (m);

W: width or height of the specimen (m);

a: notch length (m).

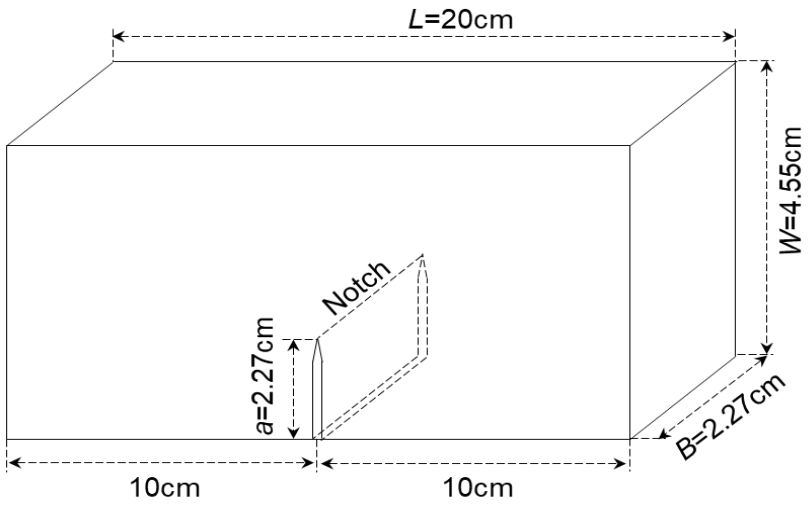

Figure 3.21 – Pre-notched beam specimen used in Three-Point Bending tests.

3.5.7. Three-Point Bending (TPB) Test – Semicircular Bend (SCB) Specimen Method

Based on one testing procedure suggested by the International Society for Rock Mechanics (ISRM), the semicircular bend (SCB) method combined with a three-point bending test was applied to obtain the fracture toughness of FR-CPB specimens cured under warm temperatures. Temperatures of 20°C, 35°C, and 45°C were used in this study. Additionally, once the specimens were mature enough (3, 7, and 28 days), the trimming process could start as mentioned in Section 3.3.7, resulting in specimens as shown in Figure 3.16 with their respective notch configuration. Three specimens were tested for each curing time to guarantee replicability.

The semicircular specimens' thickness (T) was 5cm while their diameter (D) was 10cm and the notch length was 2.5cm, approximately. To perform the three-point bending tests (TPB), a frame was designed to couple the high-precision digital force gauge (model: SHIMP FG3005, capacity: 50N, resolution: 0.05N) to the T57 loading frame and allow vertical load (P) readings acquisition while a displacement transducer was employed to collect displacement variations (u). Also, a base to hold the specimens in place had to be designed with rolling supports and an 8.13cm span (S) in between them to comply with the rock mechanics requirements as illustrated in Figure 3.22. The TPB tests in this study used a 1mm/min loading rate.

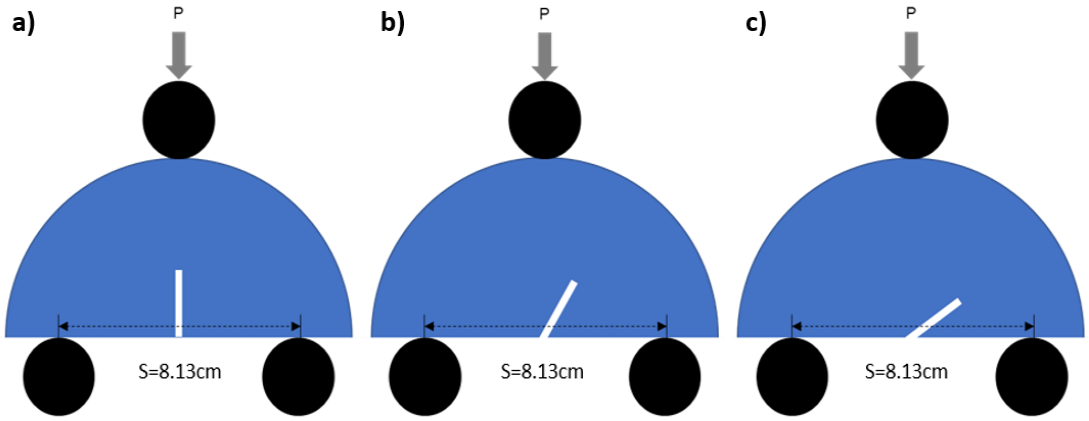

Figure 3.22 – Experimental setup of fracture toughness measurement: (a) K_I when α=0°; (b) K_{eff} when α=30°; and (c) K_{II} when α=54°.

Acknowledging that, after cracks start to appear in solid materials, stresses are concentrated on the tip of these fractures and further loading applications will trigger their propagation through the material (Liu et al., 2018). Two distinct modes in which the fracture propagation can happen inside the rock mechanics field are called: mode I (tensile) and mode II (in-plane shearing) (Kuruppu et al., 2014), as illustrated in Figure 3.23. When any of these modes are combined, it generates a called combined- or mixed-mode. In this study, α=0° is applied for mode I (K_I), α=54° for mode II (K_{II}), and α=30° for a mixed-mode (K_{eff}) that combines mode I plus mode II.

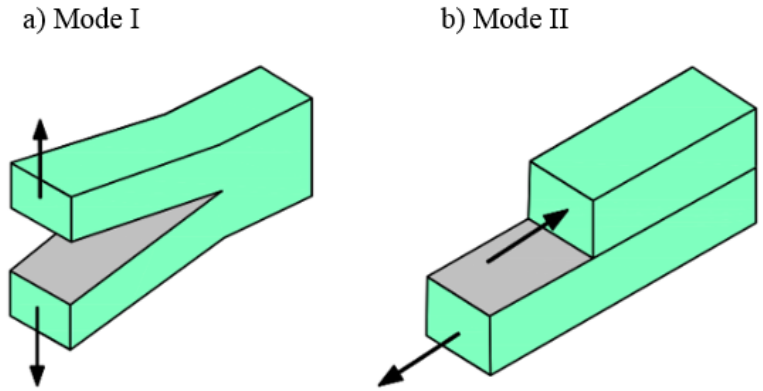

Figure 3.23 – Fracture propagation modes: (a) mode I and (b) mode II (Feng et al., 2019).

Therefore, three pre-specified notch positions were used in this study to determine K_I, K_{II}, and K_{eff} of FR-CPB. To calculate the fracture toughness, the following calculation methods were adopted (K values in $P_a.\sqrt{m}$):

Mode I fracture toughness (based on SCB specimen with a vertical notch (α=0°)):

$$K_I = \frac{P}{DT}\sqrt{\pi a}Y_I \tag{6}$$

Where,

P: maximum force (peak value of force vs. displacement curve) (N);

D: diameter of semicircular specimen (m);

T: thickness of semicircular specimen (m);

a: notch length (m);

Y_I: normalized stress intensity factor for mode I (in this study, Y_I=6.52) (dimensionless).

Mode II fracture toughness (based on SCB specimen with an inclined notch (α=54°)):

$$K_{II} = \frac{P}{DT}\sqrt{\pi a}Y_{II} \tag{7}$$

Where,

P: maximum force (peak value of force vs. displacement curve) (N);

D: diameter of semicircular specimen (m);

T: thickness of semicircular specimen (m);

a: notch length (m);

Y_{II}: normalized stress intensity factor for mode II (in this study, Y_{II}=1.072) (dimensionless).

Mixed Mode fracture toughness (based on SCB specimen with an inclined notch (α=30°)):

$$K_{eff} = \sqrt{K_I^2 + K_{II}^2}$$

$$K_{eff} = \sqrt{\left(\frac{P}{DT}\sqrt{\pi a}Y_I\right)^2 + \left(\frac{P}{DT}\sqrt{\pi a}Y_{II}\right)^2}$$

$$K_{eff} = \frac{P}{DT}\sqrt{\pi a}\sqrt{Y_I^2 + Y_{II}^2} \tag{8}$$

Where,

P: maximum force (peak value of force vs. displacement curve) (N);

D: diameter of semicircular specimen (m);

T: thickness of semicircular specimen (m);

a: notch length(m);

Y_I: normalized stress intensity factor for mode I (in this study, Y_I=4.052) (dimensionless);

Y_{II}: normalized stress intensity factor for mode II (in this study, Y_{II}=1.445) (dimensionless).

3.6. Auxiliary Laboratory Analysis

3.6.1. Scanning Electron Microscopy (SEM) Observation

SEM observations were conducted on early and advanced age FR-CPB samples to investigate differences in the material`s microstructure with respect to temperature variation and further comprehend the aspects related to the bonding between fibers and the medium they were inserted. To allow this kind of observation, a potent microscope (Hitachi SU-70) was employed and pieces with surface dimensions of 2mm by 2mm plus 1 mm thickness were removed from dry FR-CPB specimens, requiring gold coating to enable any image formation.

3.6.2. Chemical Shrinkage

Apart from the microstructure analysis, the self-desiccation and associated densification process in CPB were assessed by the chemical shrinkage measurement according to ASTM C1608-17. Since chemical shrinkage mainly takes place in CPB during an early age, the chemical shrinkage measurement was conducted on CPB specimens with three different cement content (2, 4.5, and 7%) for 28 days, respectively. Two replicate samples were prepared for each cement content to improve the reproducibility and accuracy of the experimental measurements. Moreover, based on previous studies (Zhang et al., 2013; Tazawa et al., 1995), it has been confirmed that Erlenmeyer flasks are able to enlarge the surface area of samples and thus improve the precision of chemical shrinkage measurement. Therefore, 250ml Erlenmeyer flasks were adopted to contain fresh CPB

paste covered by tap water. The experimental setup of chemical shrinkage measurement is presented in Figure 3.24. Furthermore, to confirm the self-densification process and its contribution to the K_{Ic}, the measurement of dry density was conducted on CPB specimens at the curing time of 7, 28 and 90 days according to ASTM D7263-09.

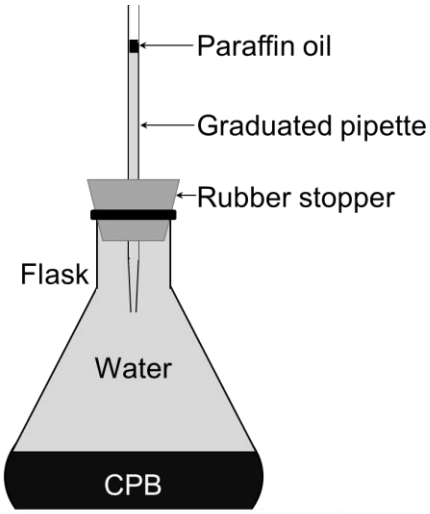

Figure 3.24 – Experimental setup of chemical shrinkage measurement.

The chemical shrinkage was calculated by the ratio of water volume change and the initial mass of cement in CPB:

$$CS = \frac{\Delta V}{m_c} \tag{9}$$

Where,

CS: chemical shrinkage coefficient (mL/g);

ΔV: volume change of water measured by the graduated pipette (mL);

m_c: initial mass of cement in the flask (g).

3.6.3. Vacuum-Based Rapid Re-saturation Approach

To identify the effect of saturation state, two groups of 90-day CPB specimens were prepared. When the curing time reached 90 days, one group of CPB specimens was re-saturated. However, after placed into water, the re-saturation process took more than 24 hours in 90-day specimens. The slow re-saturation process affects the accurate control of curing time and thus the cement hydration in CPB. Therefore, a rapid re-saturation approach was developed in this study. As shown in Figure 3.25, to accelerate the re-saturation process, the 90-day CPB specimens were placed in

a three-gallon vacuum chamber filled with tap water. Then, a vacuum pump (model: BA-3.6 CFM 1-Stage Vacuum Pump) was adopted to apply negative pressure (suction) of 101 kPa in the chamber for one hour. Then, the β pore water coefficient ($\beta=\Delta u/\Delta\sigma_3$, with u as pore water pressure, and σ_3 as confining pressure) was measured through a triaxial shear test apparatus according to ASTM D4767 to examine the saturation state. Through the rapid re-saturation approach, a β value greater than 0.95 was obtained and thus confirmed the effectiveness of the proposed rapid re-saturation approach.

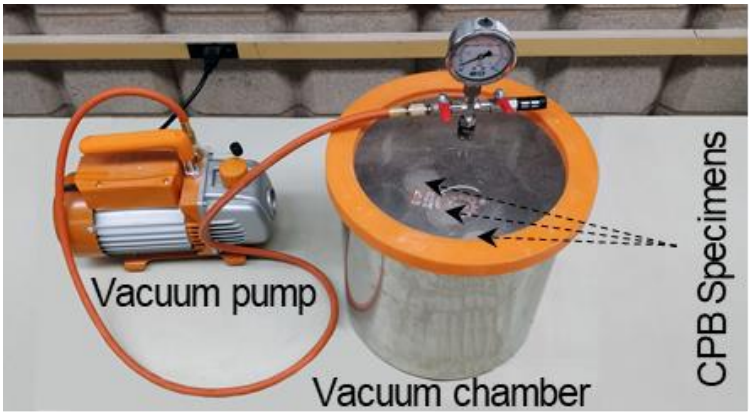

Figure 3.25 – Experimental setup through the vacuum-based rapid re-saturation approach.

3.7. Summary

This chapter was intended to be used as a laboratory report, conveying the necessary information to guarantee that the experiments employed were able to be replicated and, thus, comply with the transparency parameters a serious research work must attain. Important information about the materials, tools, equipment pieces, mixture recipe and specimen preparation, experimental study programs, and auxiliary laboratory analysis applied in this research is found in this chapter. However, to better organize and help the reader`s understanding,

Table 3.6 was created as a summary of all the experiments presented in this chapter.

Table 3.6 – Summary table of experimental procedures.

TESTS / PARAMETERS	UCS Test	STS Test	DS Test	CU Test	TPB Test	
					Beam Specimen	SCB Specimen
C_c (%)	4.5	4.5	4.5	4.5	2, 4.5 and 7	4.5
w/c	7.6	7.6	7.6	7.6	7.6 and 7.6 of the 4.5% C_c for 2% and 7% C_c	7.6
Fiber Content ($\%_{CW}$)	0.5	0.5	0.5	0.5	-	0.5
Curing Time (Days)	7, 28 and 90	7, 28 and 90	7, 28 and 90	3, 7 and 28	3, 7, 28 and 90	3, 7 and 28
Specimens per Curing Time	3	3	3	3	3	3
Temp. (^oC)	20, 35, and 45	20, 35, and 45	20, 35, and 45	20, 35, and 45	-	20, 35, and 45
Normal Load (kPa)	-	-	50, 100 and 150	-	-	-
Confining Pressure (kPa)	-	-	-	25, 50 and 75 kPa for 3-day specimens; 50, 100 and 150 for 7-day specimens; 100, 200 and 300 for 28-day specimen	-	-
Equations Page	65	66	67	70	71	73 and 74

OBS: The undrained curing state was applied to all samples to account for the worst-case scenario.

Chapter 4 Results and Discussion

4.1. Compression and Tensile Behavior

4.1.1. Effect of curing temperature on the compressive and tensile behavior of early-age FR-CPB

The comparison of constitutive curves of early-age (7-day) FR-CPB subjected to various curing temperatures is presented in Figure 4.1. In this figure, the compressive and tensile behavior results were plotted side by side to allow a better understanding of the relationship between these two behaviors as they act in opposite directions. Moreover, the results were demonstrated in this manner because the compression and tensile test results can generate their own Mohr circle, facilitating the creation of the failure surface.

From Figure 4.1, it can be observed that curing temperature significantly affects the pre- and post-failure behavior of FR-CPB subjected to uniaxial compressive and tensile stresses. Specifically, at the pre-failure stage, the hardening behavior becomes more evident with the increased curing temperature. Correspondingly, the slopes (i.e., elastic modulus in Figure 4.1a, and material stiffness in Figure 4.1b) of the loading curves become steeper as curing temperature increases. As cementitious materials present temperature-dependent properties, a more cohesive and dense CPB matrix can be formed at warmer curing temperatures. Therefore, the resultant stiffer and stronger CPB can resist the deformation to a higher extent, causing the enhancement of the hardening behavior. However, it should be noted that the loading portions of FR-CPB and control CPB cured at the same temperature (20°C) are close to each other, which indicates the relatively limited effect of fiber inclusion on the pre-failure behavior.

At the post-failure stage, softening behavior can be observed in both compressive and tensile unloading processes, and becomes more apparent as curing temperature increases. The strain corresponding to peak stress (see Figure 4.1a) and displacement corresponding to peak loads (see Figure 4.1b) decrease with the increased curing temperature, which implies the weakening tolerance capacity of plastic deformation and thus the loss of material ductility at warmer curing temperatures. However, there exist some distinct aspects of the compressive and tensile behavior of FR-CPB at the post-failure stage. First, early-age FR-CPB shows distinct residual compressive strengths, while similar residual tensile resistance forces were observed in the STS tests. This is

because, as shown in Figure 4.2, the shear cracks are commonly observed in FR-CPB specimens under compressive tests. Correspondingly, frictional resistance can be mobilized along the shear crack surfaces and contributes to the residual compressive strength. Additionally, due to the lubricant effect of pore water between solid particles (Martin et al., 2009), a larger interparticle shear resistance can develop when more pore water is consumed by the accelerated cement hydration at a warmer curing temperature. Consequently, a higher residual compressive strength is obtained from FR-CPB cured at a warmer curing temperature. However, no friction mobilization occurs along the tensile cracks. Therefore, similar residual tensile resistance forces are observed in FR-CPB under STS tests. Second, as shown in Figure 4.1b, it is interesting to find that an enhanced pseudo hardening behavior (i.e., a second peak force) appears at the post-failure stages. The pseudo hardening behavior can be explained by the progressive development of the passive fiber bridging effect at the post-failure stage. As discussed previously, the warmer curing temperature is able to facilitate the formation of a more dense and cohesive CPB matrix which can hold the fibers to a greater extent. Consequently, an improved pseudo hardening behavior is obtained from FR-CPB cured at a warmer temperature.

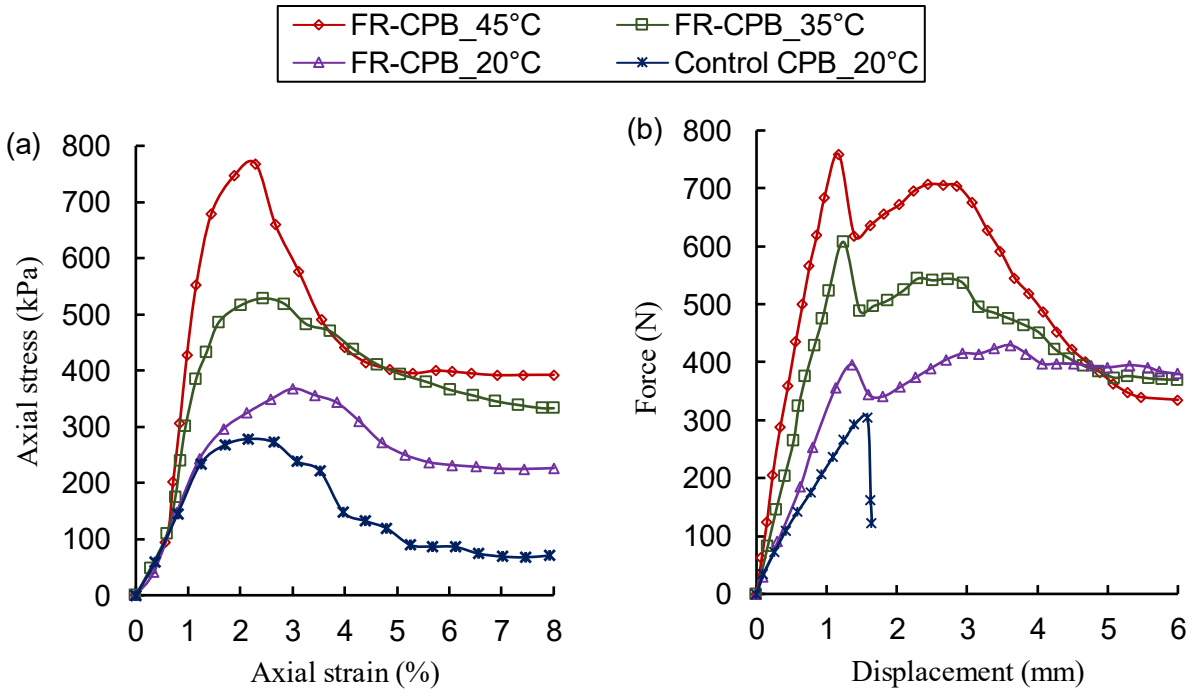

Figure 4.1 – Early-age (7-day) constitutive behavior of FR-CPB: (a) stress-strain behavior from compression tests (UCS values) and (b) force-displacement curve from tensile tests (STS values).

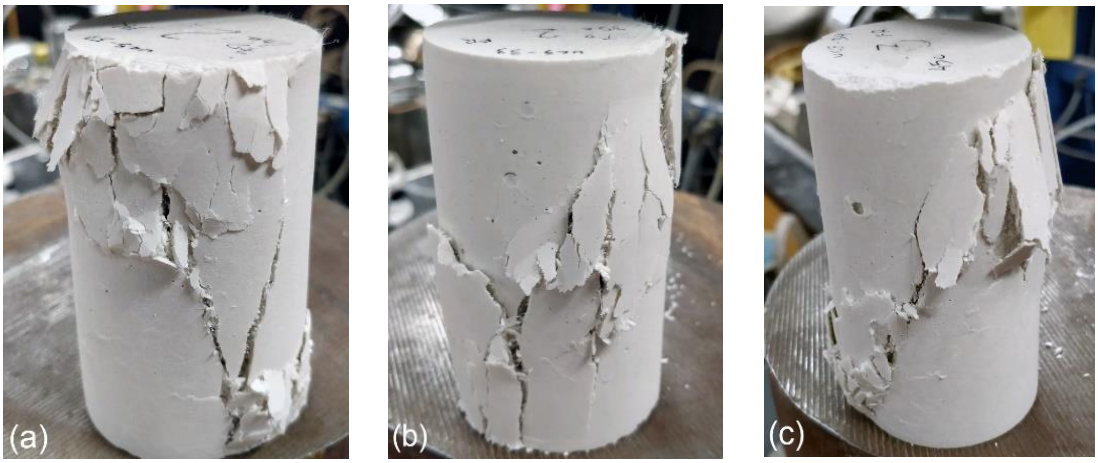

Figure 4.2 – The shear cracks developed in early-age (7-day) FR-CPB subjected to UCS tests with a curing temperature of (a) 20°C, (b) 35°C, and (c) 45°C.

4.1.2. Effect of curing temperature on the compressive and tensile behavior of advanced-age FR-CPB

Figure 4.3 presents the typical constitutive curves of advanced-age (90-day) FR-CPB cured at various curing temperatures. As explained in the first paragraph of Session 4.1.1., this figure was also plotted in this manner. For Figure 4.3, it can be seen that the constitutive behavior of advanced-age FR-CPB still shows strong temperature-dependent hardening behavior at the pre-failure stage and softening behavior at the post-failure stage, which is similar to the early-age behavior (see Figure 4.1). However, compared to the early-age constitutive behavior, advanced-age FR-CPB illustrates a noticeable difference in the post-failure regimes. For the post-failure compressive behavior, FR-CPB shows similar residual compressive strength. This is because the cement hydration consumed a large portion of the pore water (Kropp et al., 2012). As a result, the lubricant effect of pore water becomes weaker at the advanced ages. Therefore, similar friction mobilization takes place along the shear failure surfaces in advanced-age FR-CPB, and thus yields similar residual strength values. Moreover, the pseudo hardening behavior becomes relatively unnoticeable compared to those observed in early-age FR-CPB under STS tests. The weakened pseudo hardening behavior can be interpreted by the combined effect of loss of high cohesion and fiber pullout from the CPB matrix after the peak force. Specifically, advanced-age CPB cured at warmer temperature possesses a higher cohesion, which accounts for a greater proportion of tensile strength of FR-CPB. Consequently, the loss of the greater proportion of tensile after peak force directly causes the comparatively weak pseudo hardening behavior induced by the fiber bridging

effect. Moreover, the abruptly released strain energy after the peak resistance force is partially dissipated by the tensile crack propagation and partially consumed by the stress redistribution around fibers (see Figure 4.4). For the latter, the loss of large cohesion and the associated release of large strain energy may cause the fiber pullout and thus weaken the fiber bridging effect in the CPB matrix and the pseudo hardening behavior.

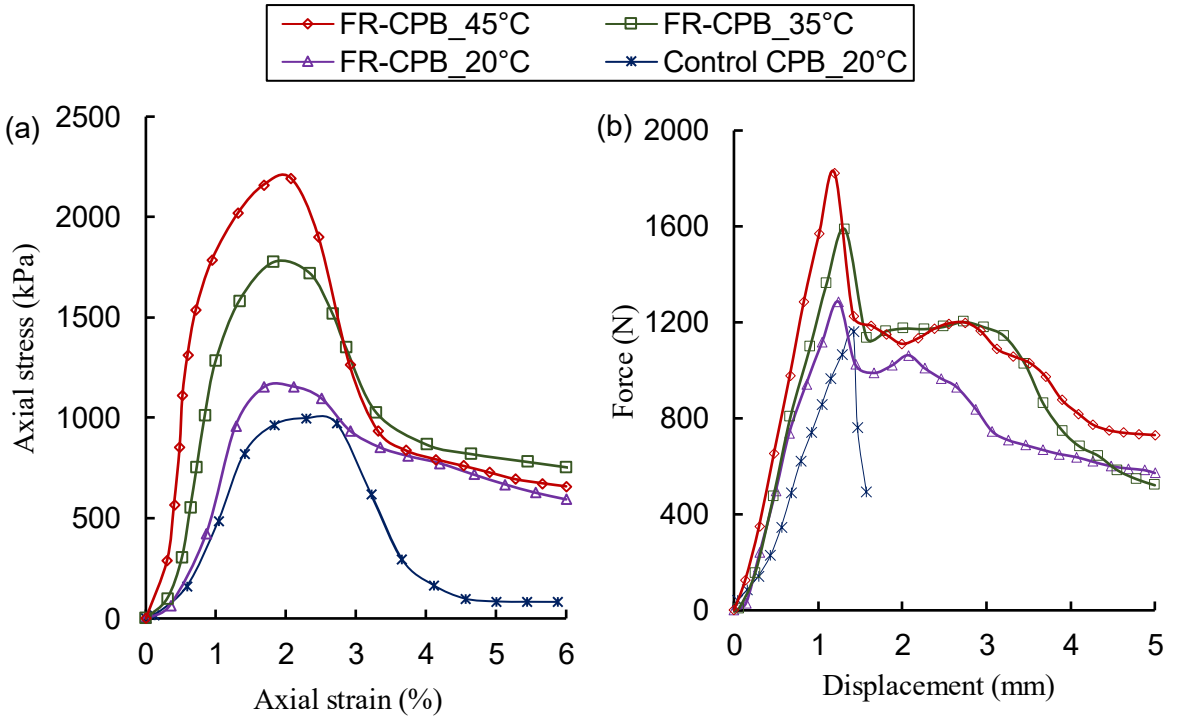

Figure 4.3 – Advanced-age (90-day) constitutive behavior of FR-CPB: (a) stress-strain behavior from compression tests (UCS values) and (b) force-displacement curve from tensile tests (STS values).

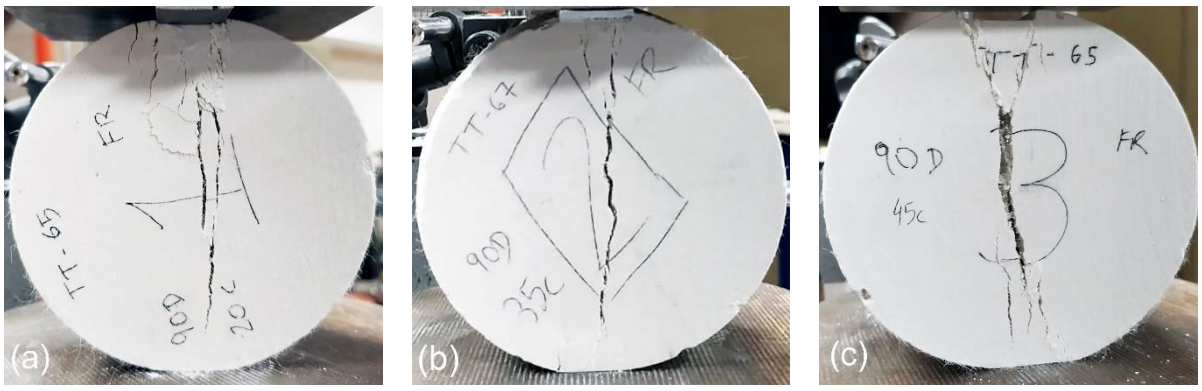

Figure 4.4 – The tensile cracks developed in advanced-age (90-day) FR-CPB subjected to STS tests with a curing temperature of (a) 20°C, (b) 35°C, and (c) 45°C.

4.1.3. Effect of curing temperature on the elastic modulus and material stiffness of FR-CPB

The material resistance to being deformed elastically can be quantitatively evaluated by the elastic modulus from compressive stress-strain curves, and material stiffness from the tensile load-displacement curves. To ensure the comparability of material resistance to elastic deformation, the secant modulus at 50% peak stress and secant stiffness at 50% peak force are adopted in this study. The calculated elastic modulus and material stiffness were presented in Figure 4.5 (a) and (b), respectively. It can be seen that FR-CPB cured at warmer curing temperatures possesses a higher resistance to non-permanent deformation. The effect of enhanced resistance to the elastic deformation on the mechanical behavior of FR-CPB is twofold. Firstly, the stiffer FR-CPB formed in the warmer curing temperature scenario is able to provide more immediate support when subjected to the static and dynamic loadings from surrounding rock walls, contributing to the mechanical stability of underground openings. Secondly, based on the studies concerning cemented soil (Wang et al., (2020); Liu et al., (2019)) and concrete (Gafoor and Dinkler, (2020); Bekele et al., (2019)), a more brittle response of constitutive behavior is commonly featured in the stiffer cementitious materials, which may cause brittle failure in CPB subjected to finite deformation. The detailed discussion on the evolution of the material brittleness will be presented in Section 4.2.2. Moreover, through a comparison with the control CPB cured at 20°C, it is interesting to find that the addition of fibers has a limited effect on the magnitude of elastic modulus and material stiffness of FR-CPB cured at the same temperature. This can be interpreted by the higher elastic modulus of cement hydration products (over 40 GPa after 7 days (Sasmal and Anoop, (2019)) relative to that of polypropylene fibers (approximately 3 GPa (Kim et al., (2010); Bhaskar and Mohamed, (2012)). Consequently, the elastic response of FR-CPB is dependent mainly on the stiffer binding between tailings particles. Therefore, fiber inclusion plays a relatively limited role in the elastic properties of CPB materials.

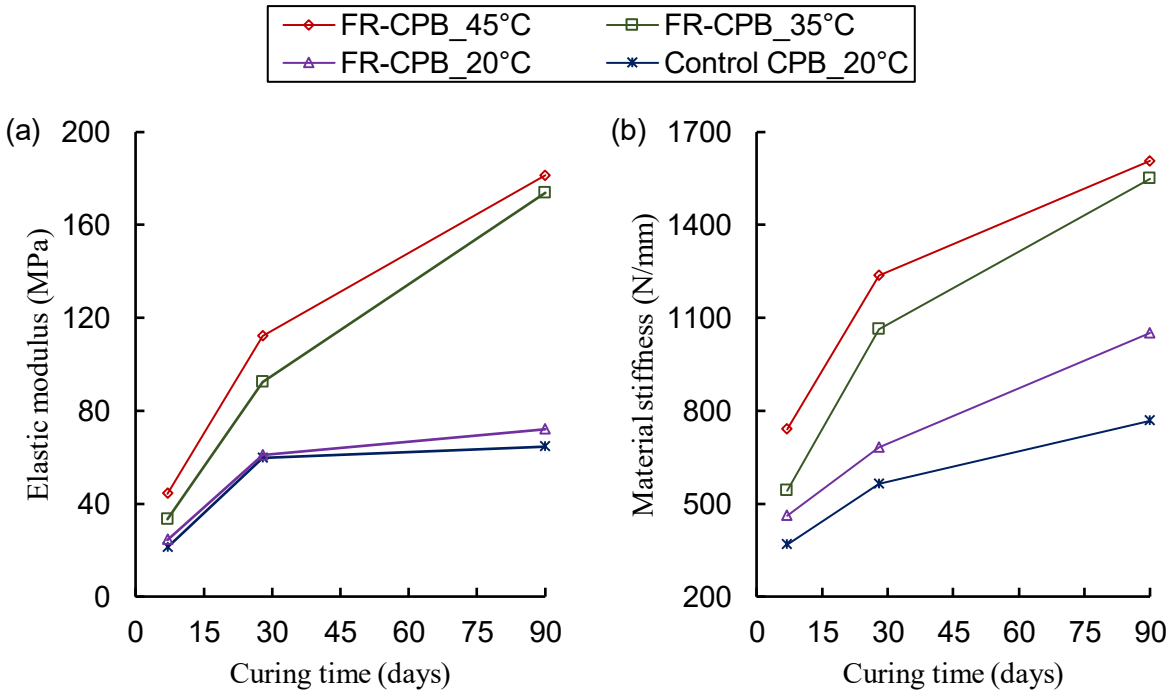

Figure 4.5 – Curing temperature sensitivity of (a) elastic modulus obtained from UCS tests and (b) material stiffness obtained from STS tests on FR-CPB.

4.1.4. Effect of curing temperature on the compressive and tensile strength of FR-CPB

Figure 4.6 shows the evolution of compressive strength and tensile strength of FR-CPB cured at different temperatures from early to advanced ages. Compared to FR-CPB cured at 20°C, significant improvement of material strength is obtained from FR-CPB cured at warmer temperatures. Moreover, it is interesting to find that the strength improvement of FR-CPB cured at a warmer temperature becomes more obvious at the advanced ages. For instance, compared to the FR-CPB cured at 20°C (see Figure 4.6a), FR-CPB cured at 45°C shows improvement in 7-day and 90-day UCS, with 64% (from 474kPa to 777kPa) and 110% (from 1135kPa to 2365kPa) increase, respectively. A similar improvement is observed in the long-term tensile strength as well (see Figure 4.6b). The significant strength improvement at advanced ages can be explained by the strengthened fiber-matrix interfacial interaction as the progress of cement hydration. This because a denser and more cohesive CPB matrix can be formed at a warmer curing temperature, resulting in a stronger interfacial friction and bonding force between fibers and tailings particles. Consequently, the desirable effect of fiber bridging can be further strengthened at advanced ages with a warmer curing temperature, which directly contributes to the control of crack propagation

in the CPB matrix and to the improvement of the material strengths. However, compared to the enhancement of the material`s strength induced by the warmer curing temperature, FR-CPB and control CPB cured at the same temperature (20°C) show less strength variability from early to advanced ages. Therefore, due to the temperature dependence of cement hydration and its effect on the fiber-CPB matrix interfacial interaction, the extent of fiber reinforcement is dependent on the curing temperature.

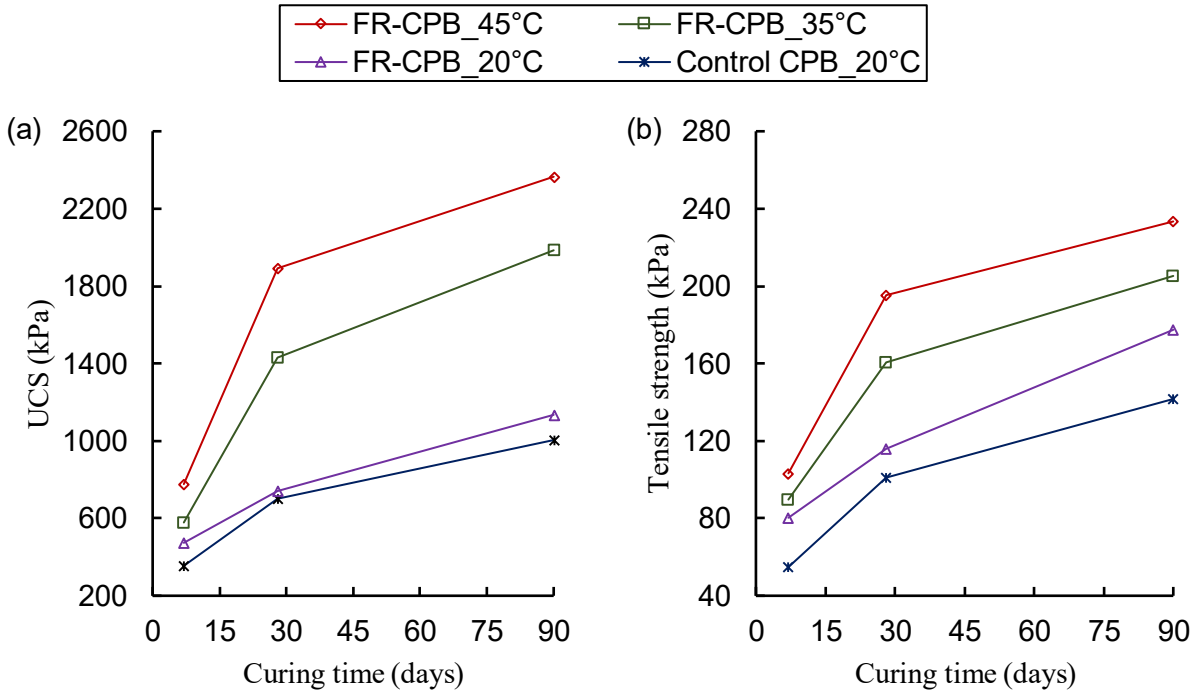

Figure 4.6 – Curing temperature sensitivity of (a) compressive strength and (b) tensile strength on FR-CPB from early to advanced ages.

4.2. Shear Behavior

4.2.1. Effect of warmer curing temperature on the shear behavior of early-age FR-CPB

Figure 4.7 shows the typical stress-displacement behavior of early-age (7-day) FR-CPB subjected to warmer curing temperatures. It was observed that the warmer temperature affects pre- and post-failure shear behavior of early-age FR-PCB. For the pre-failure behavior, it is interesting to note that compared to the early-age shear behavior under low normal stress (Figure 4.7a), FR-CPB under higher normal stress (Figure 4.7b) shows a noticeable hardening behavior (i.e., the nonlinear portion of stress-displacement curves) in the pre-failure regime as the curing temperature increases.

This is because the chemical shrinkage causes the self-densification process in CPB (Cui and Fall, 2018a). Correspondingly, warmer temperature results in a denser cohesive porous matrix. When denser, FR-CPB is exposed to higher normal stress and the interlocking effect among tailings particles becomes more pronounced and thus results in a strengthened hardening behavior.

The softening behavior of FR-CPB becomes more obvious with the increased curing temperature in the post-failure stage. This is because warmer curing temperature is favorable for the improvement of cohesion among tailings particles (Fall and Pokharel, 2010). Correspondingly, the higher cohesion associated with warmer temperature delivers a great contribution to the shear strength of FR-CPB. Consequently, when shear displacement breaks the cemented tailings after the peak stress, a greater reduction in shear stress (i.e., the enhanced softening behavior) is observed in FR-CPB cured with warmer temperatures.

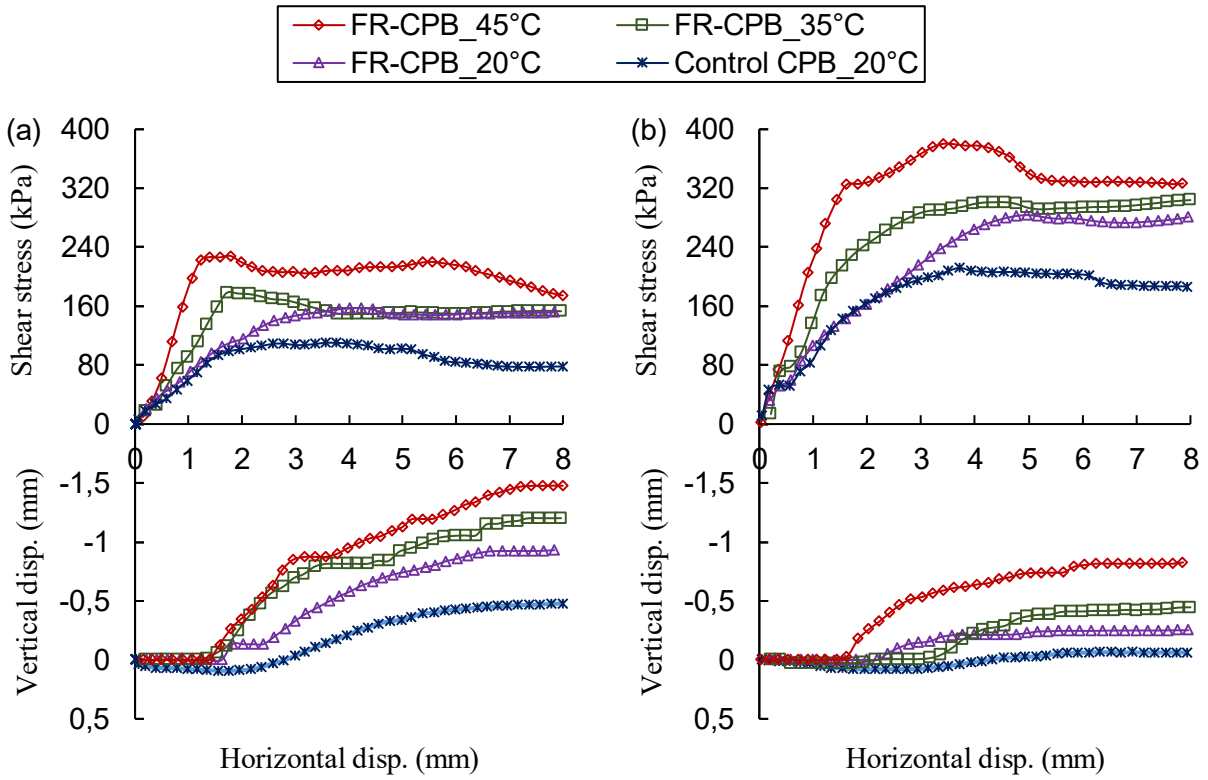

Figure 4.7 – Effect of curing temperature on the shear behavior of early-age (7-day) FR-CPBs subjected to the normal stress of: (a) 50 kPa; and (b) 150 kPa

Moreover, the vertical displacement was measured to evaluate the shear-induced volume change. In the field of geotechnical engineering, the signs convention utilize compression strain (contraction) as positive and tension strain (expansion) as negative. As shown in Figure 4.7, the

volumetric expansion becomes progressively larger as curing temperature increases. This is because when the shear stress gradually overcomes the particle-particle interlocking, sliding and rolling take place among different particles (DeJong and Westgate, 2005). As a result, the microscale particle sliding and rolling on top of the denser FR-CPB matrix formed due to warmer temperature curing caused the greater volumetric expansion at the macroscale scenario. Furthermore, the addition of fibers significantly improves the peak and residual shear strength compared to ordinary CPB. This is because the polypropylene microfibers bridge the cracks in the porous matrix and, thus, provides an effective reinforcement for crack width control (Lee and Jeon, 2011), especially in the post-failure stage.

Since the peak shear strength cannot be mobilized simultaneously and equally along a slip surface, the residual shear strength also plays a vital role in stabilizing the backfill mass in the field. Therefore, it is necessary to study both peak and residual shear strength for the FR-CPB design. As shown in Figure 4.8, early-age FR-CPB displays higher peak shear strength and residual shear strength when curing temperature increases. For instance, compared to FR-CPB at a curing temperature of 20°C and subjected to the normal stress of 150kPa, the peak shear strength obtained from same normal stress increases by approximately 7% (to 328 kPa) at 35°C and 17% (to 359 kPa) at 45°C. Similarly, the corresponding residual shear strength is improved by 28% (to 300kPa) at 35°C and 35% (to 315kPa) at 45°C. The improvement of peak and residual shear strength is closely related to the progress of cement hydration in the CPB matrix. Specifically, due to the temperature dependence of cement hydration (Cheng et al., 2020), warmer temperature facilitates more hydration products including calcium silicate hydrate (C-S-H) and calcium hydroxide (CH) precipitated in the CPB matrix, and thereby enhances the cementation of porous media. Consequently, a higher peak shear strength is obtained from CPB cured under warmer temperature. The self-desiccation process in CPB explains the enhancement of residual shear strength. With the advancement of cement hydration, a greater amount of pore water is consumed in CPB cured at a warmer temperature (Cui and Fall, 2018b). Correspondingly, a higher matric suction is expected from warmer temperature cured FR-CPB, which will contribute directly to the improvement of residual shear strength.

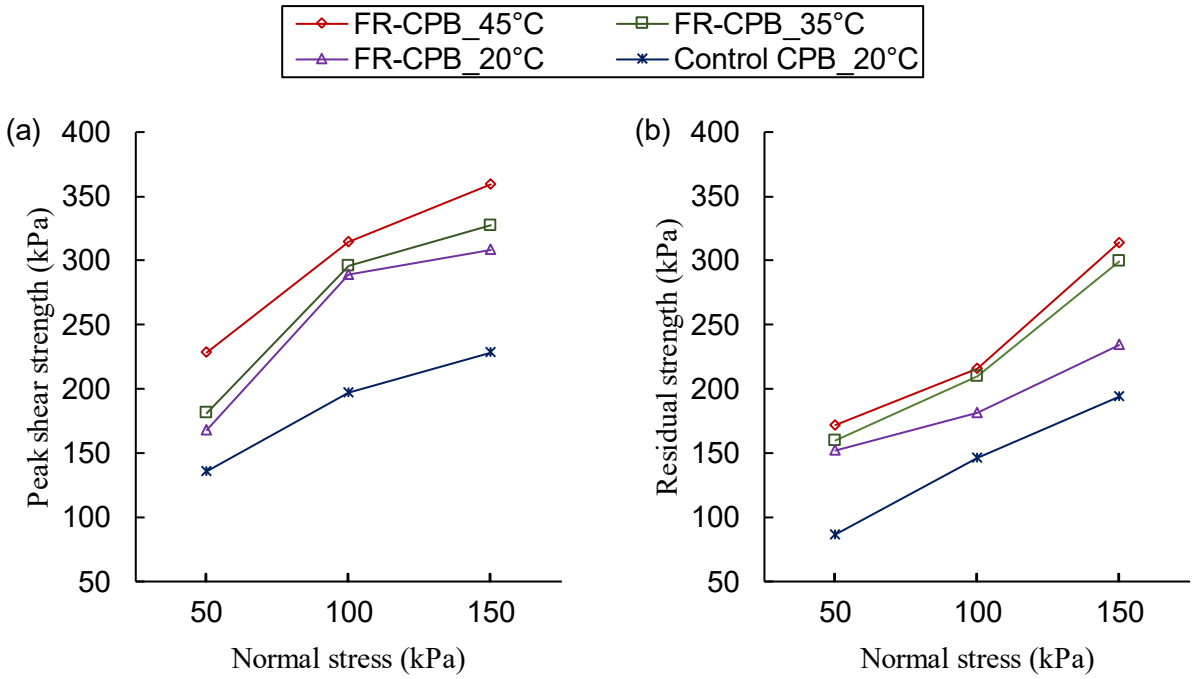

Figure 4.8 – Evolution of (a) peak shear strength and (b) residual shear strength of early-age (7 days) FR-CPBs cured at different curing temperatures.

4.2.2. Effect of warmer curing temperature on the shear behavior of advanced-age FR-CPB

Typical shear stress-displacement curves of FR-CPB at 90 days are plotted in Figure 4.9. Compared with the early-age shear behavior (Figure 4.7), 90-day FR-CPB shows distinctive pre- and post-failure shear behaviors. At the pre-failure stage, FR-CPB displays an unnoticeable hardening behavior, which indicates the loss of ductility of FR-CPB at an advanced age. Based on previous studies (Gettu et al., 1990; Yu et al. 2017), it has been found that cementitious materials with higher strength generally have a more brittle nature, which is consistent with the finding in this study. However, FR-CPB demonstrates consistent and considerable strength degradation after peak stress, which also indicates the higher brittleness of FR-CPB at an advanced age.

Moreover, it is interesting to note that regardless of curing temperature, FR-CPB shows similar residual strength under the same normal stress at an advanced age. This is because the cohesive strength component is lost after the peak stress. Consequently, the friction strength component and matric suction dominate the evolution of residual strength (Kayadelen et al., 2007).

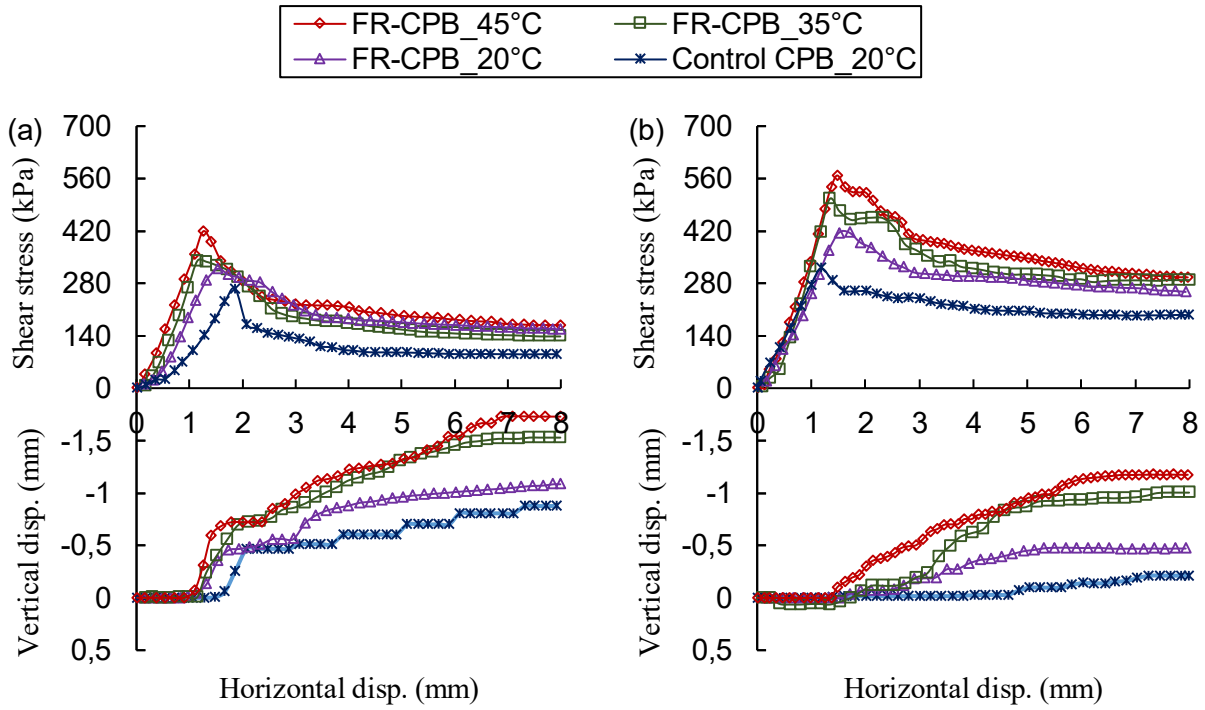

Figure 4.9 – Effect of curing temperature on the shear behavior of advanced-age (90-day) FR-CPBs subjected to the normal stress of (a) 50kPa; and (b) 150kPa.

For the friction strength component, previous studies have shown the effect of cement hydration on friction angle is very limited at advanced ages (Askarani and Pakbaz, 2016; Boutouba et al., 2019). Moreover, the contribution of matric suction to material strength is dependent on the water content in the porous media (Fredlund et al., 1996). Therefore, the higher matric suction associated with lower water content can only impose a limited effect on the improvement of material strength at advanced ages. Consequently, FR-CPB demonstrates similar residual strength at an advanced age. However, the volume change of 90-day FR-CPBs still shows an increasing trend as curing temperature increases, which is similar to the shear-induced volume change behavior of early-age FR-CPB. The mechanism responsible for the shear-induced volumetric deformation has been discussed in Section 4.2.1.

As discussed previously, FR-CPB shows a weakened hardening shear behavior and a considerable reduction from peak shear strength to residual strength at an advanced age, which indicates the development of material brittleness. Material brittleness plays a crucial role in the mechanical stability of FR-CPB subjected to definite deformation.

To quantitatively characterize the brittle behavior of FR-CPB, the brittleness index, I_b, ($I_b=\tau_{max}/\tau_{res}-1$, with τ_{max} as peak shear strength, and τ_{res} as residual shear strength) defined by

Consoli et al. (1998) is adopted. The calculated brittleness index of FR-CPBs cured at different temperatures is shown in Figure 4.10. From this figure, it became clear that warmer temperature causes a higher brittleness index of FR-CPB from early to advanced ages. For example, 7-day FR-CPB cured at 35˚C and 45˚C respectively have a brittleness index of 0.13 and 0.27, with an increase of 30% and 170% with reference to I_b (approximately 0.1) of FR-CPB cured at 20˚C. Similarly, the brittleness index of 90-day FR-CPB is enhanced by 56% (I_b =1.68) and 65% (I_b=1.79) relative to the counterpart (I_b=1.08) of FR-CPB cured at 20˚C. However, as mining depth increases, the high geo-stress and large deformation are commonly featured in the surrounding rocks (Meng et al., 2013; Yuan et al. 2018). In consequence, the increased brittleness can impose the destabilizing effect on FR-CPB structure as the plastic deformation tolerance is reduced. Moreover, compared with I_b obtained from control CPB, FR-CPB cured at the same temperature (20˚C) shows a substantial reduction in the brittleness index, which indicates the positive contribution of fiber inclusion to the improvement of material ductility and thus to the control of brittle failure of CPB materials.

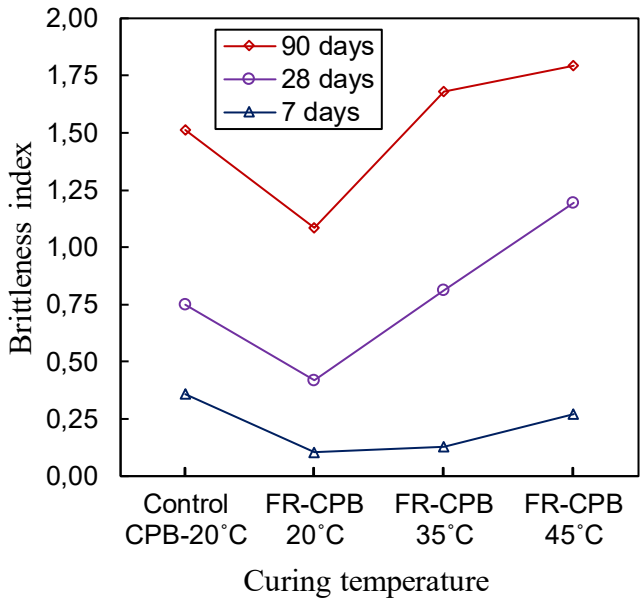

Figure 4.10 – Comparison of brittleness index of 7-day and 90-day FR-CPBs under normal stress of 50kPa and cured at different temperatures.

4.2.3. Effect of warmer curing temperature on shear stiffness of FR-CPB

The slope of stress-displacement curves can determine the shear stiffness. Based on the definition of secant modulus E_{50} (i.e., Young's modulus), the secant shear stiffness at 50% of peak shear

strength was calculated to standardize the determination of shear stiffness. The calculated shear stiffness is presented in Figure 4.11.

It is possible to observe that a stiffer FR-CPB is obtained at warmer curing temperature. This is because, at warmer curing temperature, the chemical hardening process can proceed to a higher extent and thus yield a stiffer cementitious material. The increased shear stiffness due to cement hydration can effectively redistribute the load to the surrounding rock mass (Helinski et al., 2010), and thus provide more immediate secondary group support to the underground excavation. Moreover, FR-CPB and control CPB cured at 20˚C demonstrate similar shear stiffness from early to advance ages. This is because, compared to the stiffness of the cemented matrix, the stiffness of flexible fibers is small. Consequently, the cementation process dominates the evolution of shear stiffness in FR-CPB.

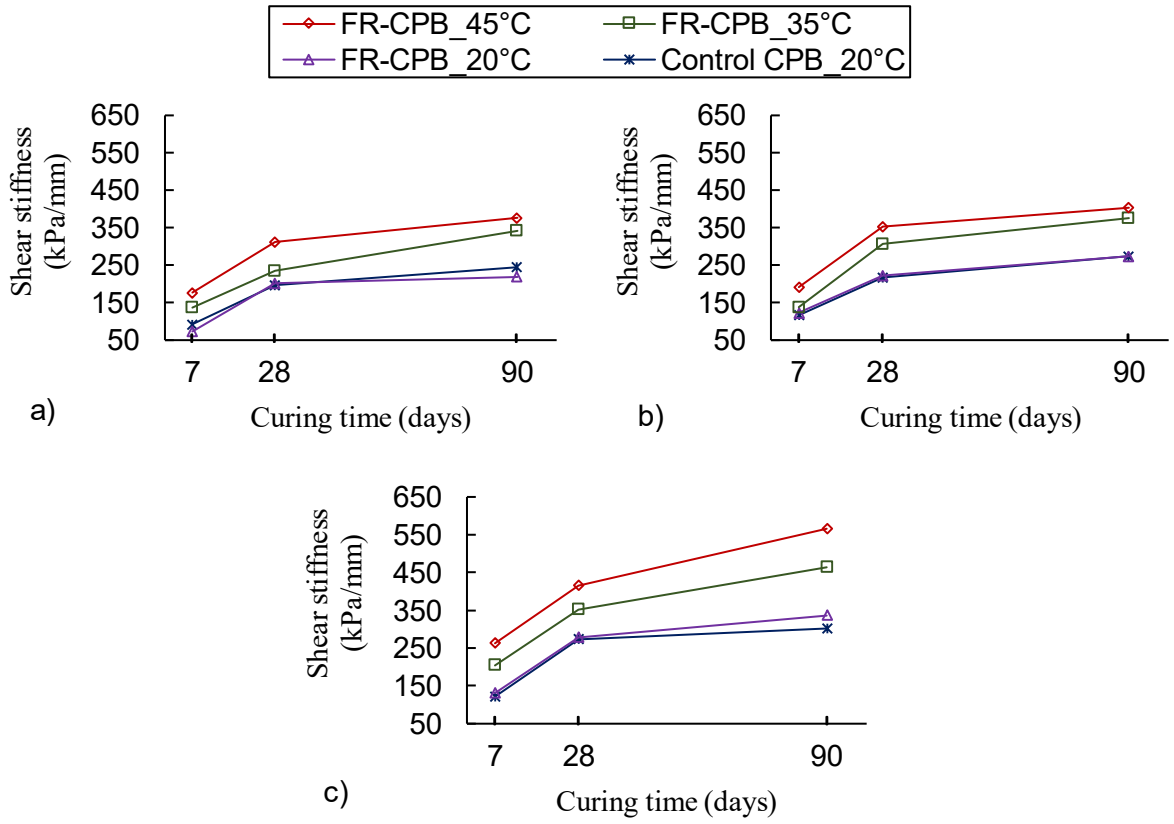

Figure 4.11 – Effect of curing temperature on shear stiffness of FR-CPBs under the normal stress of (a) 50 kPa; (b) 100kPa; and (c) 150 kPa

4.2.4. Effect of warmer curing temperature on shear strength parameters of FR-CPB

Based on the Mohr-Coulomb criterion, shear strength parameters including cohesion (c) and internal friction angle (ϕ) were determined. Figure 4.12 shows the calculated shear strength parameters of FR-CPB subjected to different curing temperatures. As expected, the cohesion shows strongly temperature-dependent evolution from early to advanced ages (Figure 4.12a). Regarding the peak shear strength (Figure 4.7 and Figure 4.8), the magnitude of cohesion becomes more comparable with curing time.

For example, the 90-day cohesion respectively accounts for 47.3% (c=169.8kPa) at 7 days, 55.6% (c=330.1kPa) at 28 days and 62.1% (c=394.4kPa) of the corresponding peak shear strength of FR-CPB cured at 45˚C and subjected to normal stress of 150 kPa. A similar correlation between cohesion and peak shear strength was also found on FR-CPB cured at 20˚C and 35˚C. However, it should be noted that when the cohesion and peak shear strength are more comparable in magnitude, the rapid and considerable loss of the large cohesive strength component after peak stress will enhance the brittle failure of FR-CPB. By contrast, through the comparison of FR-CPB and control CPB cured at 20˚C (Figure 4.12a), it can be found that fiber inclusion has a weak effect on cohesion. This is because due to the inert surfaces and low wettability of polypropylene microfibers (Tu et al., 1998; Yao and Chen, 2013), the weak interfacial adhesion between tailings particles and polypropylene microfibers has very limited contribution to the cohesive strength component of FR-CPB.

Moreover, as shown in Figure 4.12b, the effect of curing temperature on the internal friction angle is limited. More specifically, FR-CPB subjected to various curing temperatures shows a slight variation of ϕ in the range of 0.1˚ to 4˚ from early to advanced ages, which indicates the limited effect of cement hydration over the friction angle.

The weak effect of cement hydration on friction angle has been widely observed on cemented soil with a similar cement content (Clough et al. 1981; Maher and Ho 1993; Schnaid et al. 2001). Therefore, due to the insensitivity of friction angle to the temperature-dependence of cement hydration, the effect of warmer curing temperature plays a less important role in the variation of friction angle. However, from Figure 4.12b, it is evident that the inclusion of fibers can significantly increase friction angle and thus contribute to the increase of the peak shear strength (Figure 4.7 and Figure 4.8). It is important to point out that due to the poor surface roughness of the polypropylene fibers, interfacial friction resistance between fibers and the CPB matrix is

relatively weak. Consequently, shear strength improvement associated with fiber inclusion is mainly attributed to the mechanical interlocking between the fibers and tailings particles.

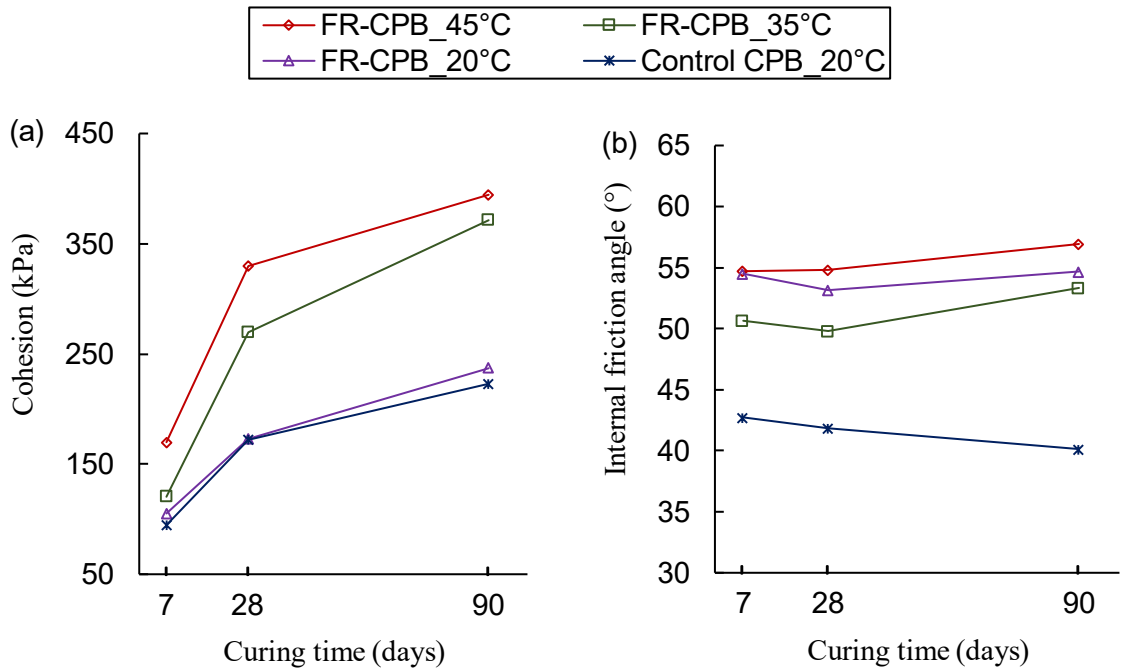

Figure 4.12 – Effect of curing temperature on shear strength parameters of FR-CPB: (a) cohesion; and (b) internal friction angle.

4.2.5. Effect of warmer curing temperature on dilation angle of FR-CPB

Figure 4.13 shows the changes of the dilation angle defined as the arctangent of the maximum increase of $\delta u_v / \delta u_h$ (with u_v as vertical displacement, and u_h as horizontal displacement). From this figure, it is seen that the warmer curing temperature can increase the dilation angle from early to advanced ages. The shear-induced volumetric deformation has been discussed in Section 4.2.1. Moreover, as expected, the degree of dilation is inhibited as the normal stress increases. However, compared with control CPB, FR-CPB shows a higher dilation angle at the same curing temperature and normal stress.

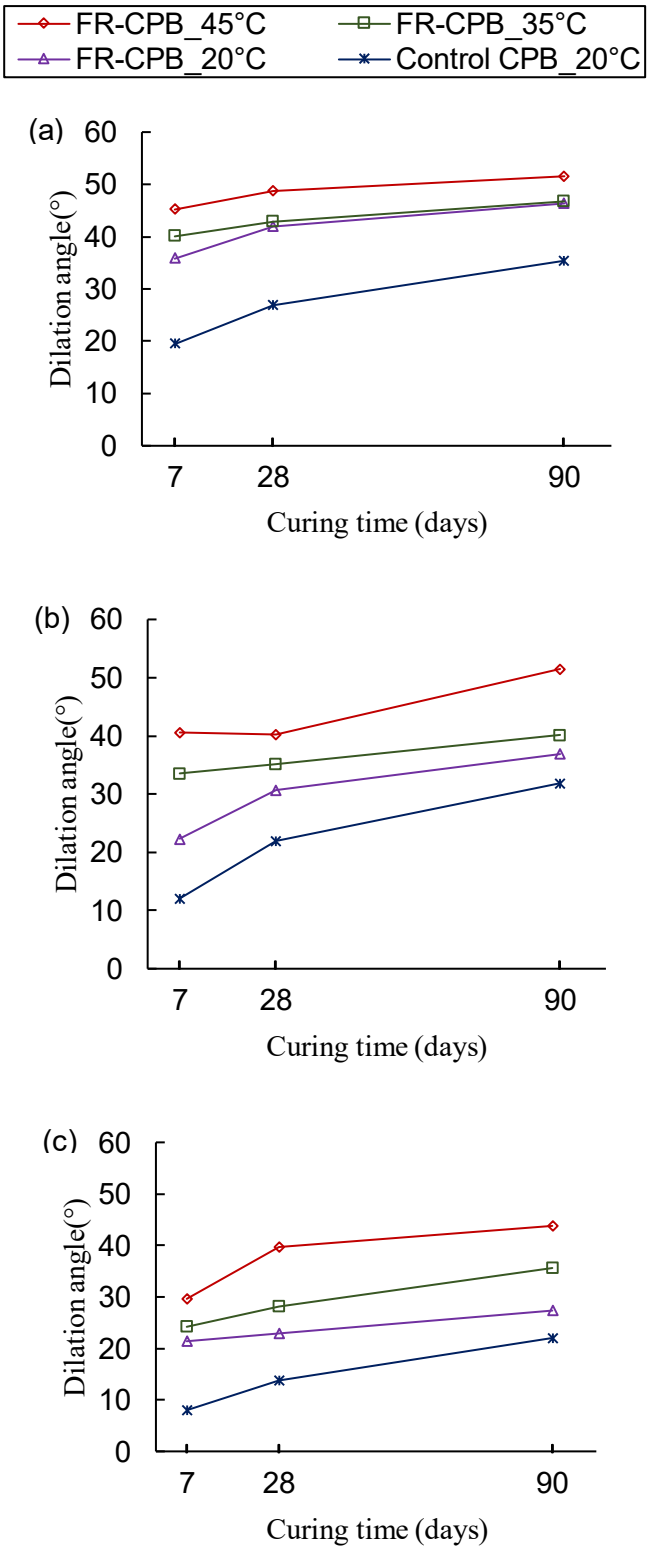

Figure 4.13 – Effect of curing temperature on dilation angle of FR-CPB under different normal stress: (a) 50kPa; (b) 100kPa; and (c) 150kPa.

It is important to address that contradictory findings regarding the effect of fiber inclusion on the dilation angle were obtained in published studies. For example, experimental studies showed that the addition of fiber can significantly increase the dilation in granular materials including soil (Diambra et al., 2010; Falorca and Pinto, 2011), and cementitious composites (Hamidi and Dehghan, 2015; Salah-ud-din, 2012). By contrast, dilation suppression due to the addition of fibers was also observed in soil (Consoli et al., 2009; Michalowski and Čermák, 2003), and cemented soil (Hamidi and Hooresfand, 2013; Kutanaei and Choobbasti, 2016).

Assuming that the diameter of fibers plays a critical role in the dilative behavior of granular materials such as CPB. More specifically, compared to the diameter (80μm) of the adopted polypropylene microfibers, approximately 96% of tailings particles possess smaller particle sizes (Figure 3.1). The considerable difference between particle size and fiber diameter is observed by the SEM images of FR-CPB specimens (Figure 4.14). Therefore, when tailings particles are subjected to shear distortion, the sliding and rolling of particles against the fibers with larger diameter cause a significant reduction in curvature of particle movement paths around the fibers. Consequently, the change in microstructure and associated volume expansion will be considerably magnified due to the inclusion of fibers.

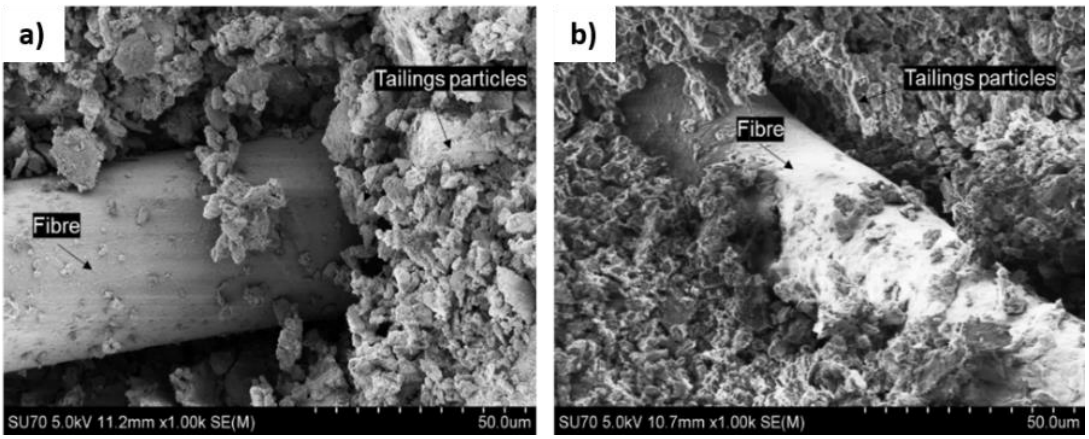

Figure 4.14 – Scanning electron micrographs of (a) 28-day, and (b) 90-day FR-CPB specimens cured at 20˚C.

4.3. Triaxial Behavior

4.3.1. Effect of warmer curing temperature on the triaxial behavior of early-age FR-CPB

The early-age (3-day) triaxial behavior is presented in Figure 4.15. From this figure, it can be seen that the warm temperature affects the stress-strain behavior of FR-CPB (Figure 4.15a). However, the volume change is insensitive to change in the curing temperature (Figure 4.15b). Assessing the

hardening session of the curve (pre-failure behavior), it is clear that the temperature possesses a very limited influence on the modulus of elasticity (i.e., the slope of the loading portion of the stress-strain curve) of the material. However, from Figure 58a, it is obvious to recognize the significant improvement in peak stresses as curing temperature increases. For example, FR-CPB cured under 45°C almost doubled its peak strength when compared to control CPB and FR-CPB cured under 20°C.

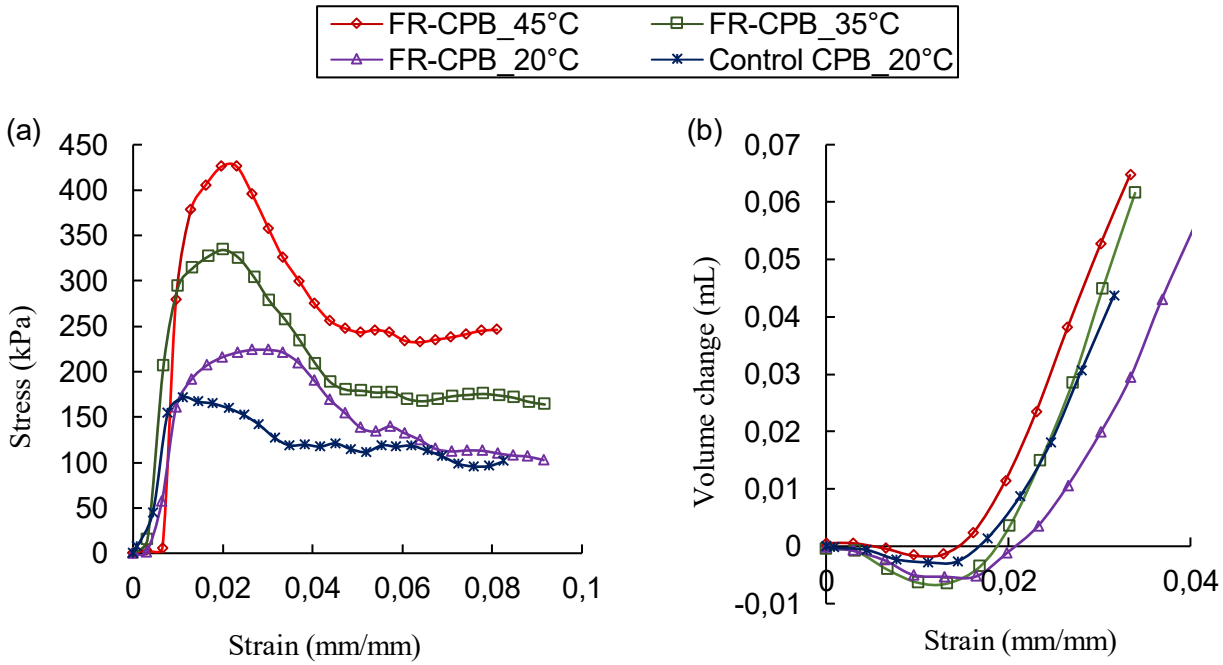

Figure 4.15 – Effect of curing temperature on the triaxial behavior of early-age (3-day) FR-CPBs subjected to a confining pressure of 75 kPa: (a) stress-strain curves; and (b) volume change curves.

As mentioned before, the temperature dependency of cement hydration (Cheng et al., 2020) affects the resultant amounts of hydration products at a given curing time. Correspondingly, when FR-CPB is cured at warmer temperatures, pore space can be refined by the participation of hydration products to a larger extent. Consequently, a more cohesive and denser FR-CPB matrix can be expected at a higher curing temperature, which contributes to the improvement of the peak stresses in FR-CPB subjected to triaxial loading conditions. At the post-failure stage, the curing temperature plays a significant role in the development of the softening behavior of FR-CPB. As shown in Figure 4.15, the softening behavior becomes more obvious with the increased curing temperature. For instance, the residual strength of FR-CPB cured at 20°C reached 113 kPa while the counterpart at 35°C demonstrated 167 kPa (48% improvement) and at 45°C resulted in 232 kPa (105% improvement) of residual strength. As discussed in Section 4.2, the post-failure behavior is

dominated by the fiber bridging effect. The warmer curing temperature can form a more cohesive CPB matrix and thus enhance the fiber-CPB matrix interfacial interaction. Consequently, a higher residual strength was observed in FR-CPB cured at warmer temperatures.

4.3.2. Effect of warmer curing temperature on the triaxial behavior of advanced-age FR-CPB

As shown in Figure 4.16, the advanced-age (28-day) triaxial behavior of FR-CPB shows significant changes in peak stress, peak strain, and residual strength as the curing temperature increases. As shown in Figure 4.16a, the peak values of FR-CPB results were enhanced with increased curing temperature. For example, compared to the peak strength (672 kPa) of FR-CPB cured at 20°C, the 28-day peak strength reached 1259 kPa (increased by 61%) at 35°C and 1725 kPa (increased by 157%) at 45°C, respectively. The strength improvement is associated with the accelerated cement hydration process at warm temperatures, which has been previously discussed.

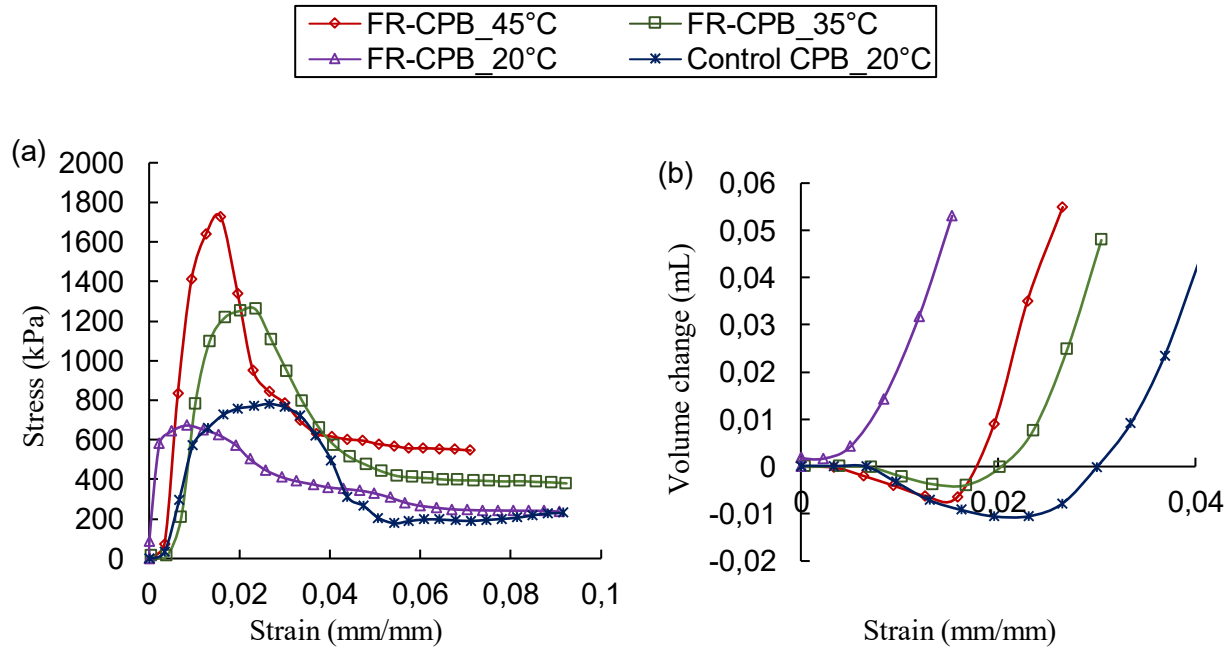

Figure 4.16 – Effect of curing temperature on the triaxial behavior of advanced-age (28-day) FR-CPBs subjected to a confining pressure of 300 kPa: (a) stress-strain curves; and (b) volume change curves.

Regarding the pre-failure behavior under confinement, it is interesting to observe the increase in the elastic modulus (E, the slope of loading curves) as temperature rises (Figure 4.16), which is consistent with the findings in the early-age FR-CPB. The increased E indicates that the material can sustain more load at a given strain level. Also, the reduction in elongation of the hardening section of the curve before the peak stress implies that the material ductility becomes weaker as

curing temperature increases. The detailed discussion about the material brittleness of FR-CPB subjected to warm curing temperature was presented in Section 4.2.2.

At the post-failure stage, it is interesting to notice the gradual enlargement of the downwards inclination of the curve after the peak with the increase of temperature. This because as the temperature increases, damage inside the material propagates at a faster and more severe pace once limit stress is reached. This scenario results in a considerable strength degradation, evidencing the weakened softening behavior and demonstrating the reason behind the loss of material ductility of FR-CPB cured at warmer temperatures.

However, even with the rapid drop in strength after the peak, FR-CPB cured at warmer curing temperature still evidenced a significant increase in the residual strength as shown in Figure 4.16. For example, FR-CPB cured at 20°C possesses a residual strength of 241 kPa, while the residual strength increases to 386 kPa at 35°C and 555 kPa at 45°C, respectively. Thus, curing temperature enhanced the residual strength of FR-CPB under the confinement of 300 kPa by 60% at 35°C and 130% at 45°C. Based on the obtained results from early- and advanced-age FR-CPB, it is confirmed that curing temperature is able to influence the development of material properties including elastic modulus and material brittleness. Moreover, the pre- and post-failure triaxial behaviors are sensitive to the curing temperature. Therefore, curing temperature plays a critical role in the triaxial behavior of FR-CPB from early to advanced ages.

4.4. Fracture Toughness Behavior

4.4.1. Effect of curing time on fracture toughness of CPB

Figure 4.17 shows the evolution of mode-I fracture toughness (K_{IC}) of CPB with a cement content of 4.5%. From this figure, it is evident that fracture toughness increases monotonically with the curing time, especially during an early age. Compared to 3-day fracture toughness (4.17 kPa·m$^{1/2}$), the K_{IC} increases by 1.47 kPa·m$^{1/2}$, 3.68 kPa·m$^{1/2}$, and 5.05 kPa·m$^{1/2}$ at the curing time of 7, 28, and 90 days, respectively. The enhanced fracture toughness with curing time is related to the development of bonding strength among tailings particles. This is because as curing time ellipses, more cement hydration products (e.g., calcium silicate hydrate (C-S-H) and calcium hydroxide (CH)) can be generated among tailings particles (Cui and Fall, 2016b), which contribute directly to the formation of a more cohesive CPB matrix. The improvement of cohesive CPB matrix by hydration products can be observed through the comparison of SEM images of the CPB specimens

at early- (at 7 days, see Figure 4.18a) and advanced-age (at 90 days, see Figure 4.18b). Consequently, CPB materials demonstrate a strongly time-dependent fracture resistance. However, the rate of change in fracture toughness shows a decreasing trend. The nonlinear evolution of K_{IC} is related to the decelerated cement hydration with curing time. This is because the spherical barrier shells of C-S-H gradually envelop the anhydrous cement during the hydration process (Rahimi-Aghdam et al., 2017). The thickened barrier shell progressively delays the diffusion of capillary water toward the anhydrous cement (Nasir and Fall, 2010), and thus slows down the cement hydration. Correspondingly, the enhancement of fracture toughness decelerates with curing time.

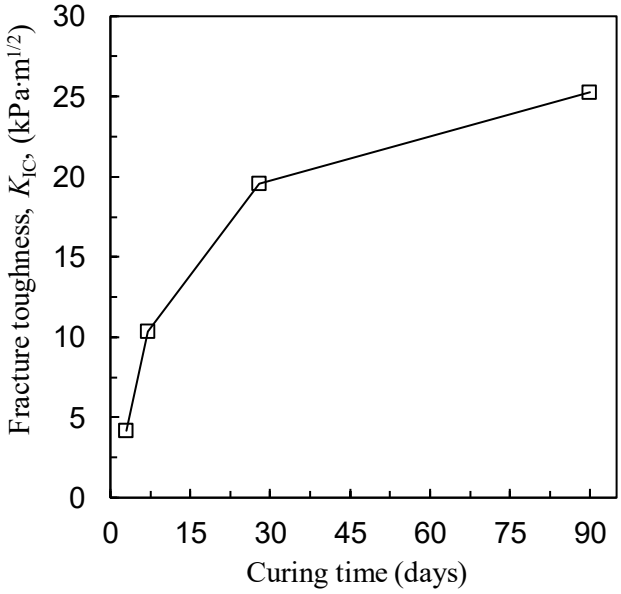

Figure 4.17 – Evolution of mode-I fracture toughness (K_{IC}) of CPB with a cement content of 4.5%.

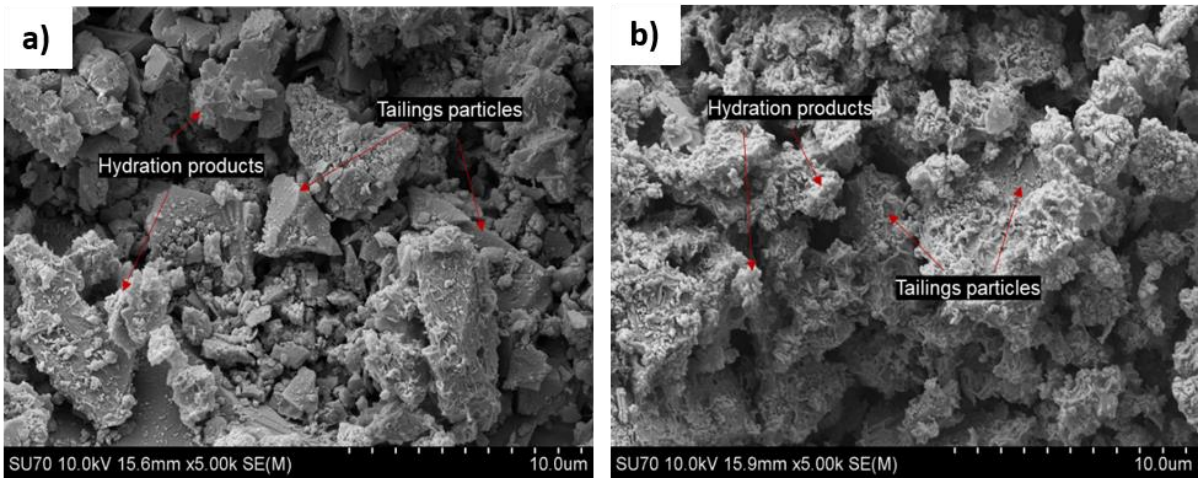

Figure 4.18 – SEM observation of microstructure of CPB at the curing time of (a) 7 days, and (b) 90 days.

The deceleration of cement hydration is also confirmed by the evolution of electrical conductivity (EC) in CPB. This is because, as an effective measure to characterize the mobility of ions, EC can be used to evaluate cement hydration kinetics (Ghirian and Fall, 2015). As shown in Figure 4.19, the measured EC of CPB with a cement content of 4.5% displays an initial increase until approximately 0.2 days. The initial increase in EC is due to the rapid cement hydration during the very early age. After the peak value, EC results show a decreasing trend with respect to curing time, which indicates the nonlinear deceleration of the cement hydration process. Consequently, the reduced hydration rate slows down the improvement of bonding strength over curing time and thereby results in a nonlinear evolution of fracture resistance (check Figure 4.17).

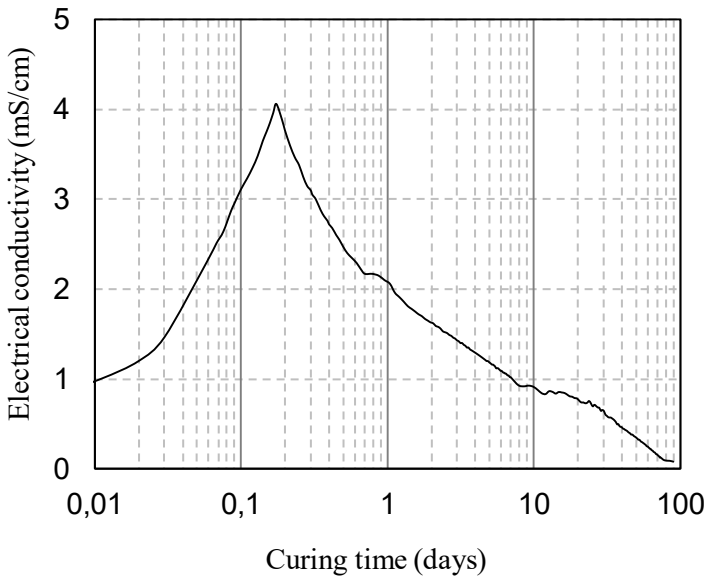

Figure 4.19 – Evolution of electrical conductivity of CPB (Cc=4.5%) with curing time.

Apart from the development of fracture toughness, it is necessary to study the fracture behavior of CPB from early to advanced ages. Letter (a) of Figure 4.20 presents the typical load versus load-point displacement curves obtained from TPB tests on CPB specimens (C_c=4.5%) at different curing times. From this figure, it is possible to see that for all curing time, the load increases approximately linearly with the displacement up to the fracture load. The linear load-displacement relationship before peak load represents the elastic response of CPB materials, which indicates CPB possesses a strongly brittle behavior. Therefore, the linear elastic fracture mechanics (LEFM) can characterize the fracture behavior of CPB. Moreover, the material stiffness defined by the slope in the linear region of the load-displacement curve can be used to describe the deformation

resistance (i.e., material stiffness) of CPB. The calculated stiffness of CPB at different curing time is illustrated in Figure 4.20b. It is demonstrated that CPB stiffness gradually develops with curing time. For example, the 90-day stiffness increase by 300% (1.61 N/mm) compared to the 3-day stiffness (0.41 N/mm). The improved stiffness results in resistance to deformation under stress to a higher extent. Based on the continuous improvement of elastic fracture behavior with time (Figure 4.20a) and material stiffness (Figure 4.20b), it can be found that CPB materials exhibit higher brittleness with curing time.

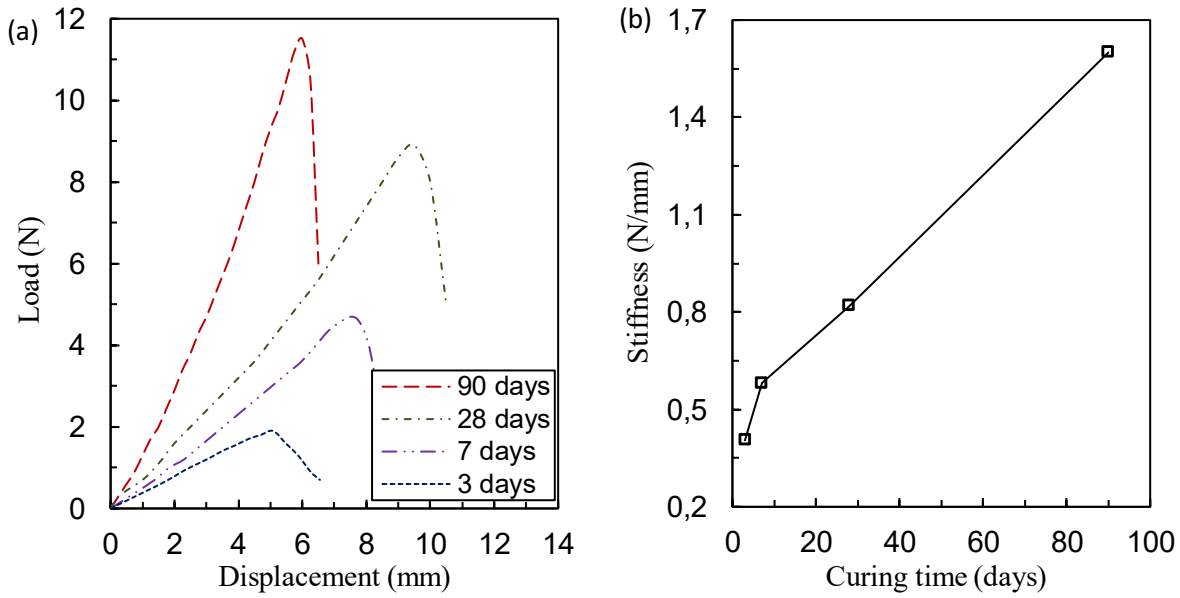

Figure 4.20 – Effect of curing time on fracture behavior (a), and material stiffness (b) of CPB with a cement content of 4.5%.

4.4.2. Effect of cement content on fracture toughness of CPB

The effect of cement content on 90-day K_{IC} is shown in Figure 4.21. It is seen that K_{IC} is sensitive to the change in cement content. Specifically, the K_{IC} increases from 11.32 kPa·m$^{1/2}$ to 55.39 kPa·m$^{1/2}$ when cement content changes from 2% to 7%. The improvement of K_{IC} with the increase in cement content is explained by the combination of at least two mechanisms including 1) the generation of more hydration products and 2) the development of a larger extent chemical shrinkage associated with higher cement content.

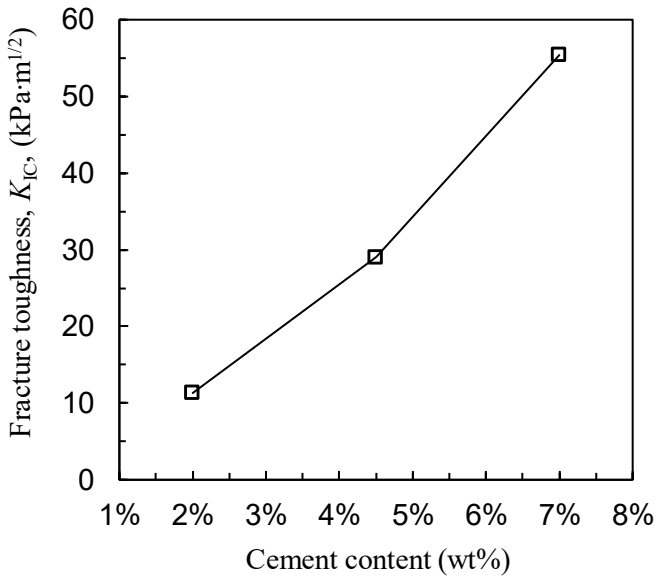

Figure 4.21 – Development of mode-I fracture toughness (K_{IC}) with the change in cement content at 90 days.

For the first mechanism, a greater amount of hydration products are generated in the CPB matrix as cement content increases, which facilitates the formation of a denser CPB matrix. As a result, CPB with higher cement content is able to resist more to the fracture propagation process. The second mechanism is related to the self-densification process in CPB. Specifically, the capillary water (liquid phase) is consumed during cement hydration and gradually converted into chemically bound water (solid phase) (Cui and Fall, 2018a). However, during the self-desiccation process, the resultant hydration products (i.e., hydrated cement and chemically bound water) are less in comparison to the not hydrated constituents (Walske, 2014; Pichler et al., 2007). Consequently, the chemical shrinkage happens, especially during early ages. The measured chemical shrinkage of CPB with three different cement contents (2%, 4.5%, and 7%) is presented in Figure 4.22. From this figure, it was found that, as the increase of cement content, the chemical shrinkage proceeds to a higher extent. For instance, the chemical shrinkage of 90-day CPB with a cement content of 7% reaches 0.1 ml/g and increases by 43% compared to the counterpart in CPB with a cement content of 2% (0.07ml/g).

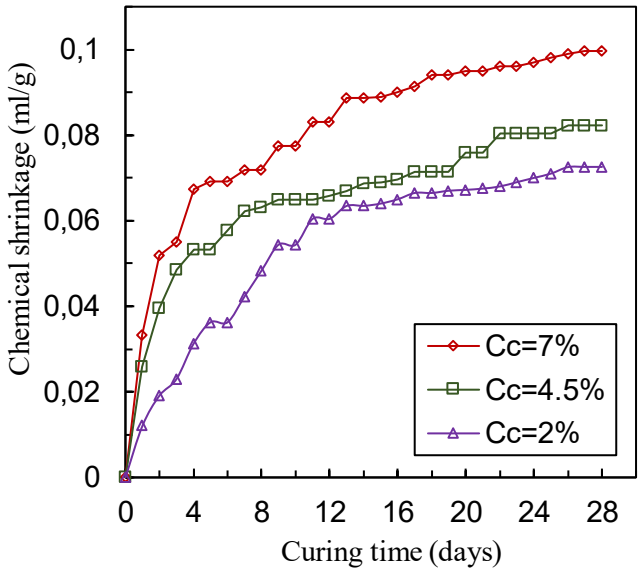

Figure 4.22 – Effect of cement content on the chemical shrinkage of CPB with curing time.

The chemical shrinkage contributes directly to the self-densification process in CPB. The correlation between the measured dry density of CPB and its chemical shrinkage is illustrated in Figure 4.23. It was observed that the dry density increases with the development of chemical shrinkage. Therefore, the enhanced self-densification process associated with a higher cement content indicates the formation of a stronger CPB matrix, which will eventually further improve the fracture resistance of CPB.

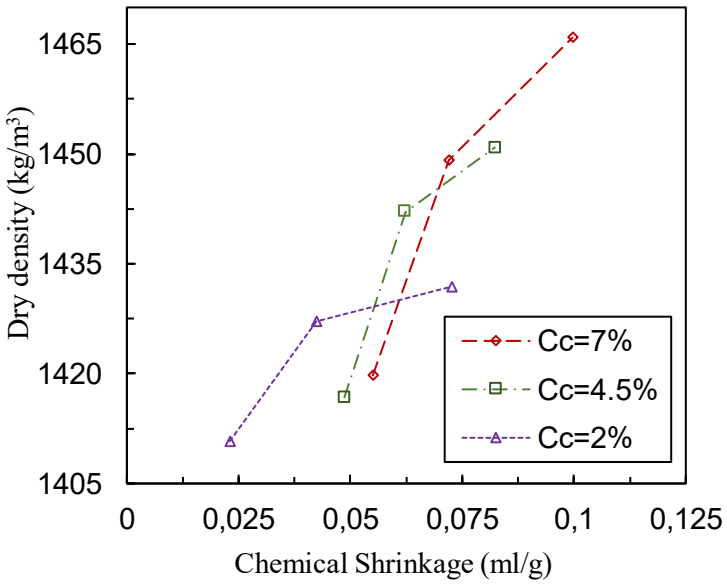

Figure 4.23 – Correlation between dry density and chemical shrinkage of CPB.

4.4.3. Effect of saturation state on fracture toughness of CPB

As discussed previously, the improvement of K_{IC} is significantly affected by the participation of hydration products and the self-densification process, which are governed by the progress of cement hydration. However, it is important to notice that the water consumption by cement hydration causes the change of CPB from a fully saturated state to a partially saturated state. Correspondingly, the solid-liquid phase system is transformed into a solid-liquid-gaseous phase system. The resultant multiphase system affects the mechanical properties and behavior of CPB. Therefore, it is necessary to investigate the effect of saturation state on the development of K_{IC}. To identify the effect of saturation state on $K_{IC,}$ TPB tests were conducted on re-saturated 90-day CPB specimens through the proposed vacuum-based rapid re-saturation method (Section 3.5.3). Then, the obtained re-saturated K_{IC} was compared with those obtained from the 90-day CPB specimens without re-saturation treatment. The comparison of K_{IC} obtained from 90-day unsaturated and re-saturated CPB specimens is shown in Figure 4.24.

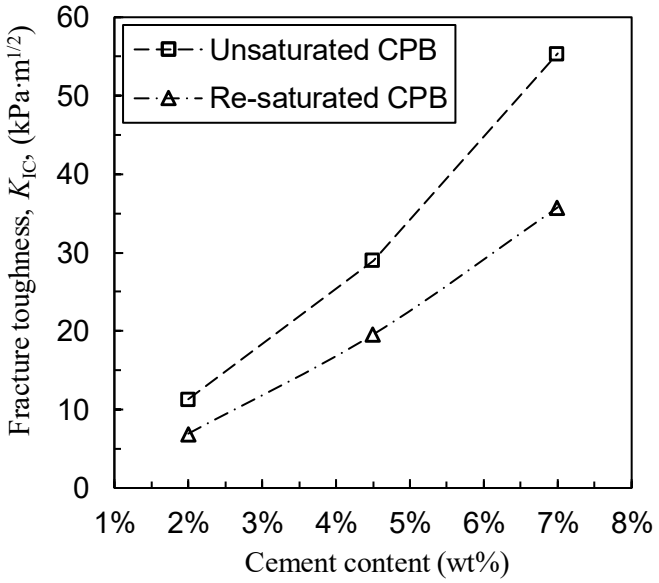

Figure 4.24 – Comparison of KIC between re-saturated and unsaturated CPBs at 90 days.

From this figure, it is observed that the saturation state significantly affects the K_{IC} of CPB. Specifically, re-saturated CPB demonstrates a lower K_{IC} compared to the counterpart of unsaturated CPB. The effect of saturation state on K_{IC} is associated with the development of matric suction in the porous CPB. This is because the water consumption by cement hydration causes the reduction of water content in CPB. Consequently, CPB changes from a fully saturated state to a partially saturated state, and thus results in the development of matric suction in CPB. The

measured matric suction of CPB with different cement content is plotted in Figure 4.25. The developed matric suction contributes positively to the improvement of bonding strength between tailings particles and thus the fracture resistance. Therefore, a higher K_{IC} is obtained from unsaturated CPB specimens. Moreover, as shown in Figure 4.24, the difference between unsaturated and re-saturated K_{IC} becomes more obvious (i.e., from 4.39 kPa·m$^{1/2}$ to 19.62 kPa·m$^{1/2}$) when cement content changes from 2% to 7%. This is because more capillary water was consumed by the cement hydration in CPB with a higher cement, and thus causes a larger matric suction in CPB (check Figure 4.25). Therefore, compared to re-saturated CPB, the unsaturated K_{IC} demonstrates an increasing trend with the increased cement content.

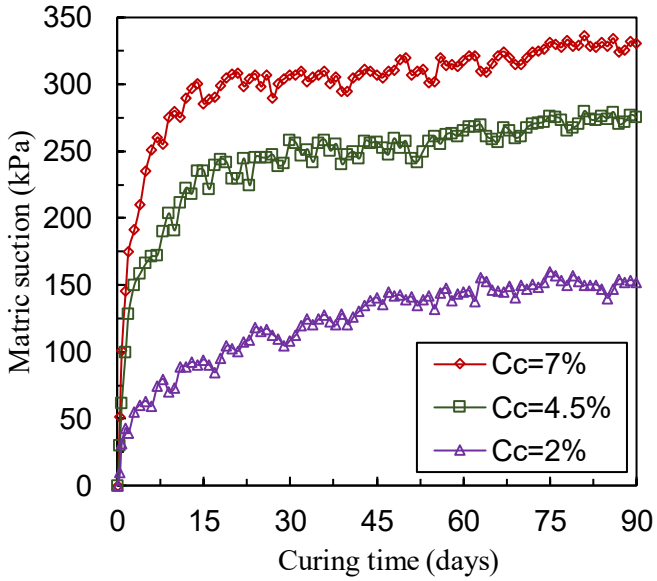

Figure 4.25 – Evolution of matric suction in CPB with curing time.

4.4.4. Effect of curing temperature on the Mode-I fracture toughness of FR-CPB

As shown in Figure 3.23, Mode-I refers to a crack propagation derived from tensile loading over the crack tip. From Figure 4.26, it is possible to see that the curing temperature can affect the evolution of K_I from early to advanced ages. For instance, FR-CPB cured under 20°C evidenced K_I values of 6 kPa·m$^{1/2}$, 9 kPa·m$^{1/2}$, and 18 kPa·m$^{1/2}$ at a curing period of 3 days, 7 days, and 28 days, respectively. However, when cured under 45°C, the K_I reaches 9 kPa·m$^{1/2}$ (improvement of 50%), 14 kPa·m$^{1/2}$ (improvement of 56%) and 23 kPa·m$^{1/2}$ (improvement of 28%) at 3, 7 and 28 days, respectively. Therefore, the temperature factor plays an important role in the mode-I fracture toughness development of FR-CPB.

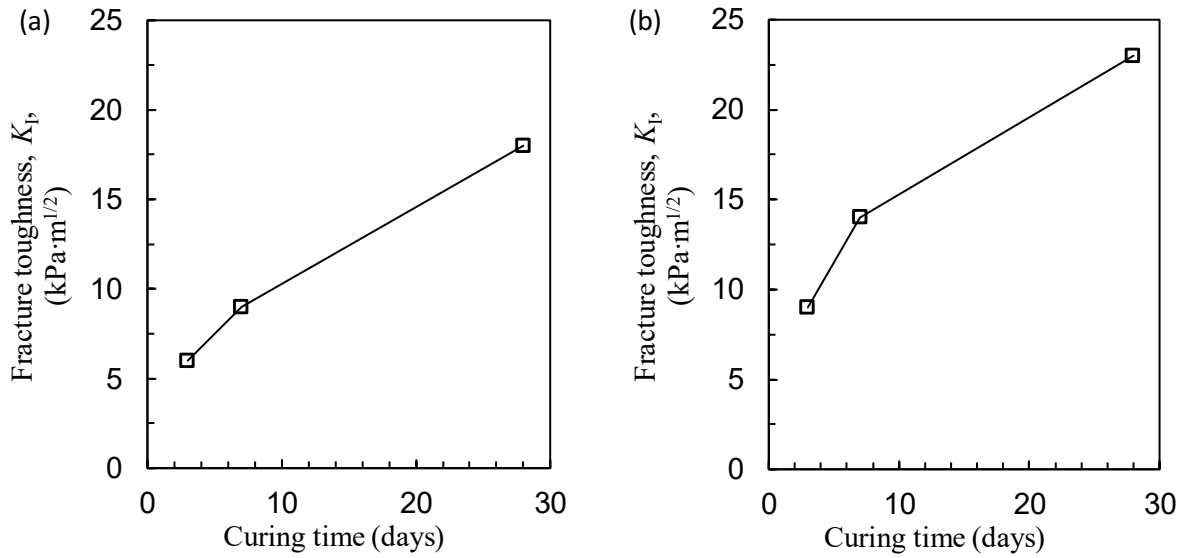

Figure 4.26 – Effect of curing temperature and time on the Mode-I fracture toughness of FR-CPB: (a) 20°C; (b) 45°C.

The effect of curing temperature on the load-displacement behavior is presented in Figure 4.27. From this figure, it can be seen that the curing temperature has a limited effect on the material stiffness (i.e., the slope of the straight-line portion) of early-age FR-CPB, but can significantly improve the peak resistance load. Moreover, a higher residual resistance force was observed from FR-CPB cured at warmer curing temperatures.

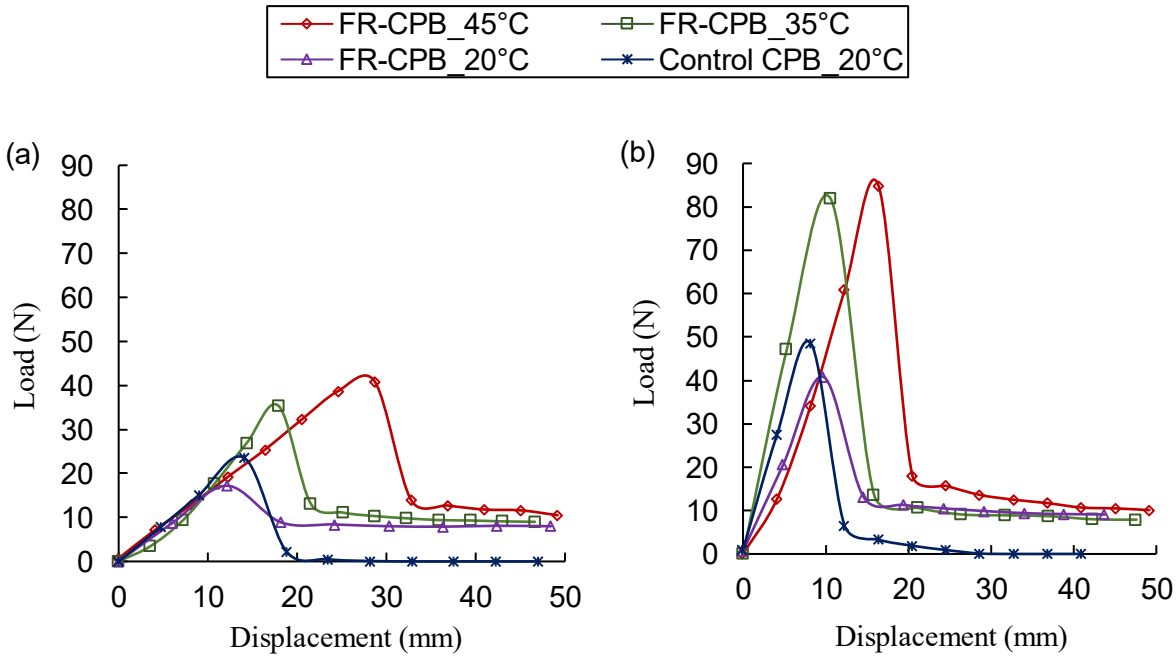

Figure 4.27 – Effect of curing temperature on the load-displacement curve of FR-CPB specimens tested on the mode-I fracture toughness: (a) early-age (3-day); (b) advanced-age (28-day).

Similar changes were observed in advanced-age FR-CPB. Therefore, the curing temperature mainly affects the post-peak fracture behavior of FR-CPB subjected to mode-I fracture loading. As discussed previously, the fiber bridging effect mainly manifests at the post-failure stage and it is sensitive to the change of curing temperature. Therefore, the obtained results further confirm that the warmer curing temperature is able to affect the mode-I fracture behavior of FR-CPB.

4.4.5. Effect of curing temperature on the Mode-II fracture toughness of FR-CPB

The effect of curing temperature on mode-II fracture toughness (K_{II}) is depicted in Figure 4.28. From this figure, it can be observed that the K_{II} of FR-CPB cured at 20°C increases from 3 kPa·m$^{1/2}$ at 3 days, to 6 kPa·m$^{1/2}$ at 7 days, and to 7 kPa·m$^{1/2}$ at 28 days, respectively. However, FR-CPB cured at 45°C possesses a K_{II} of 5 kPa·m$^{1/2}$ at 3 days, 7 kPa·m$^{1/2}$ at 7 days, and 14 kPa·m$^{1/2}$ at 28 days, respectively. Correspondingly, the K_{II} of FR-CPB cured at 45°C is improved by 67%, 17%, and 50% at a curing period of 3, 7, and 28 days, respectively. It should be pointed out that K_{II} can be mobilized as the crack tip is subjected to shear loading along the fracture surfaces. However, due to the addition of fiber into the CPB matrix, the bridging effect can also prevent the shear stress manifestation along the crack surfaces, contributing to the improvement of K_{II}. Therefore, the effect of curing temperature on the development of K_{II} further confirms that fiber inclusions not only effectively prevent tensile stresses, but also shear stresses along the crack surfaces. However, it should be noted that compared to the improvement of mode-I fracture toughness (K_I, see Figure 4.26), mode-II fracture toughness is more sensitive to curing temperature increases.

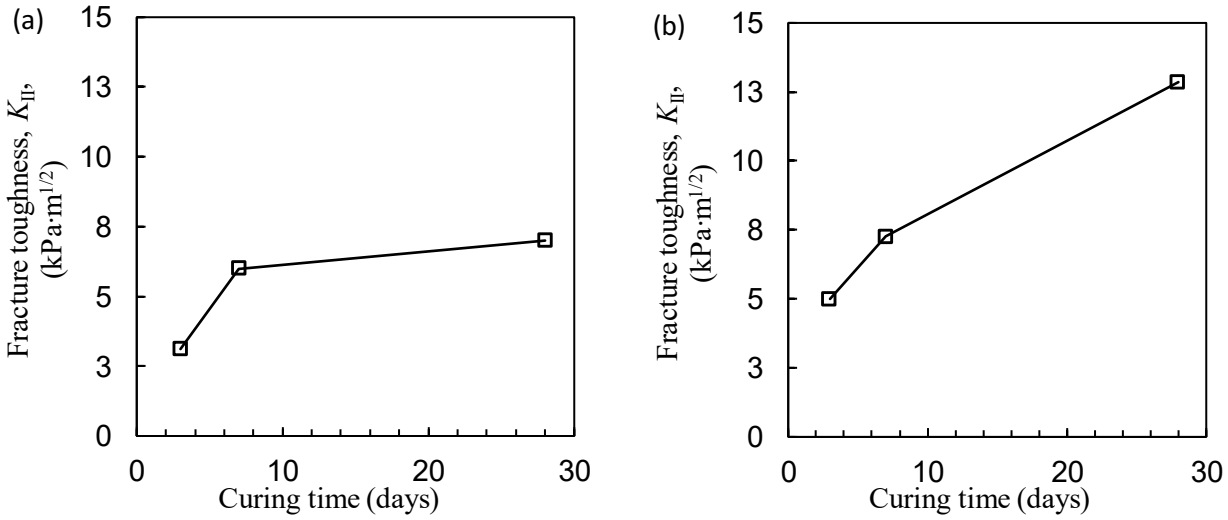

Figure 4.28 – Effect of curing temperature and time on the Mode-II fracture toughness of FR-CPB: (a) 20°C; (b) 45°C.

Particularly similar to what was observed in the pre-failure behavior of FR-CPB subjected to mode-I loading condition, mode-II fracture behavior also evidenced an increase of stiffness from 3 to 28 days (Figure 4.29). Concerning the post-failure behavior, unnoticeable change in the material`s residual resistance force was observed at various curing temperatures. The similar values of resistance force can be explained by the loss of cohesion and reduced fiber bridging effect at the post-failure stage. As the advancement of shear displacement along the crack surface, the cohesion cannot be mobilized. Moreover, after a certain relative crack displacement, the fiber pull-out failure will take place. Correspondingly, the fiber bridging effect will disappear as the crack propagates. Therefore, the residual strength of FR-CPB subjected to mode-II loading conditions is dominated by the shear friction force. However, the curing temperature has a very limited effect on the interface friction angle (see Section 4.2). Therefore, similar residual resistance forces were observed from FR-CPB under mode-II loadings.

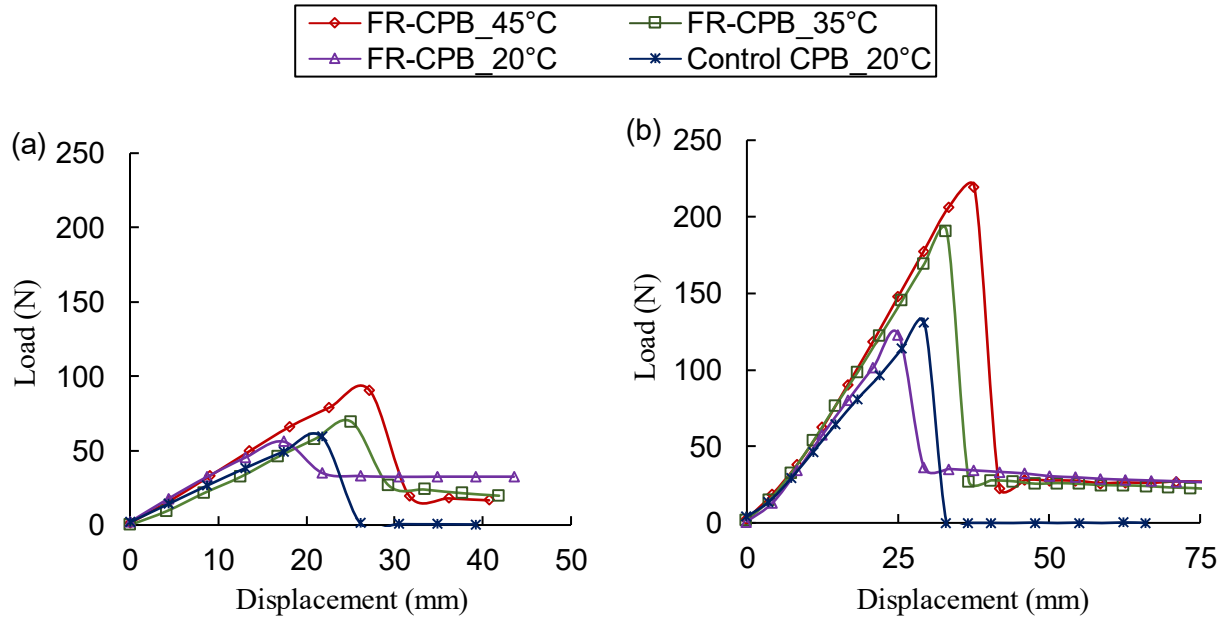

Figure 4.29 – Effect of curing temperature on the load-displacement curve of FR-CPB specimens tested on the mode-II fracture toughness: (a) early-age (3-day); (b) advanced-age (28-day).

4.4.6. Effect of curing temperature on the mixed-Mode fracture toughness of FR-CPB

Due to the complex field loading conditions, mixed-mode (mode-I plus mode-II) cracks may propagate in FR-CPB. Therefore, it is necessary to study the effect of curing temperature on the mixed-mode fracture toughness (K_{eff}). As shown in Figure 4.30a, K_{eff} of FR-CPB cured at 20°C changes from 11 kPa·m$^{1/2}$, 14 kPa·m$^{1/2}$, and 21 kPa·m$^{1/2}$ at 3-, 7- and 28-day curing period,

respectively. A similar evolution of K_{eff} was observed from FR-CPB cured at warmer curing temperature (45ºC, see Figure 4.30b). Therefore, K_{eff} demonstrates time-dependent characteristics. For the effect of curing temperature, changes of K_{eff} become more obvious at the advanced ages. For example, similar K_{eff} is obtained from early-age (3- and 7-day) FR-CPB cured at different curing temperatures. However, compared to the 28-day K_{eff} obtained at 20ºC, the counterpart at 45ºC reaches 26 kPa·m$^{1/2}$ (improvement of 24%). Therefore, K_{eff} also demonstrates curing temperature sensitivity, especially at advanced ages.

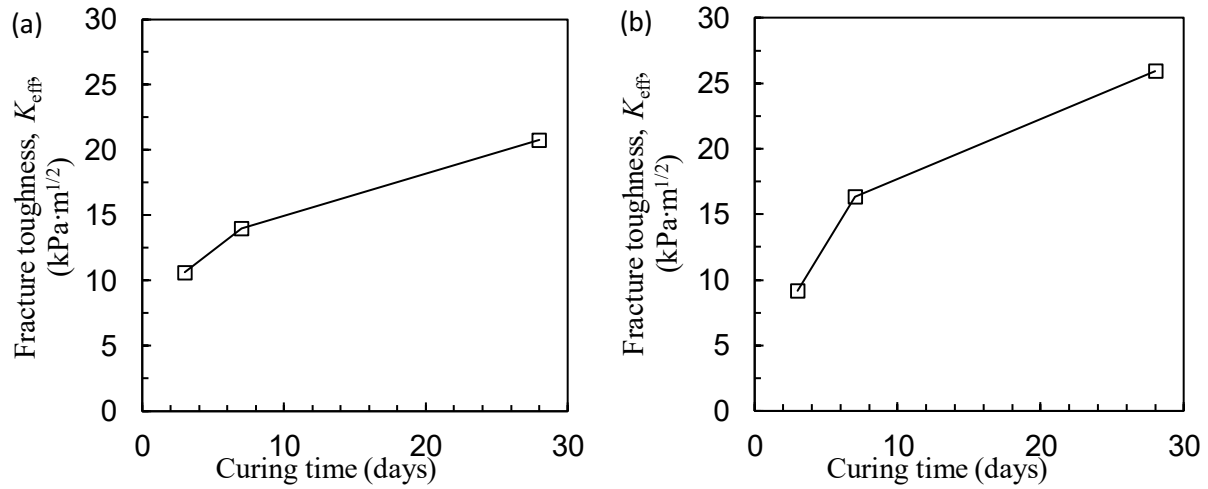

Figure 4.30 – Effect of curing temperature and time on the mixed-Mode fracture toughness of FR-CPB: (a) 20ºC; (b) 45ºC

Additionally, observing the pre-failure behavior in the load-displacement curves presented in Figure 4.31 for 3- and 28-day curing time, it is clear the substantial impact of the time factor over the stiffness development of the material. The temperature factor is inexpressive during early ages but becomes more significant during advanced ages. Based on the results from the post-failure portion of the curves presented in Figure 4.31, it is possible to conclude that the temperature and time factors evidenced very limited impact on the residual load-bearing capacity of FR-CPB at both early and advanced ages. For instance, during the early-age (Figure 4.31a), a residual load-bearing capacity value of 17 N was obtained at 20ºC and a value of 12 N was obtained from 45ºC, denoting a 30% loss in the residual load resistance capacity. Checking the advanced-age results (Figure 4.31b), the residual load resistance capacity values of 17 N for 20ºC and 18 N for 45ºC were presented, resulting in an improvement of 6%. Consequently, through the comparison between the residual load resistance capacity from early and advanced ages, it is possible to observe how similar these values are. Therefore, these similarities evidence the inhibition of the

residual load-bearing capacity development process with time and temperature curing of FR-CPB. In the author`s point of view, this inhibition manifestation results from the gradual evolution of the material brittleness of FR-CPB cured under warmer temperatures, which has been discussed in Session 4.2.2.

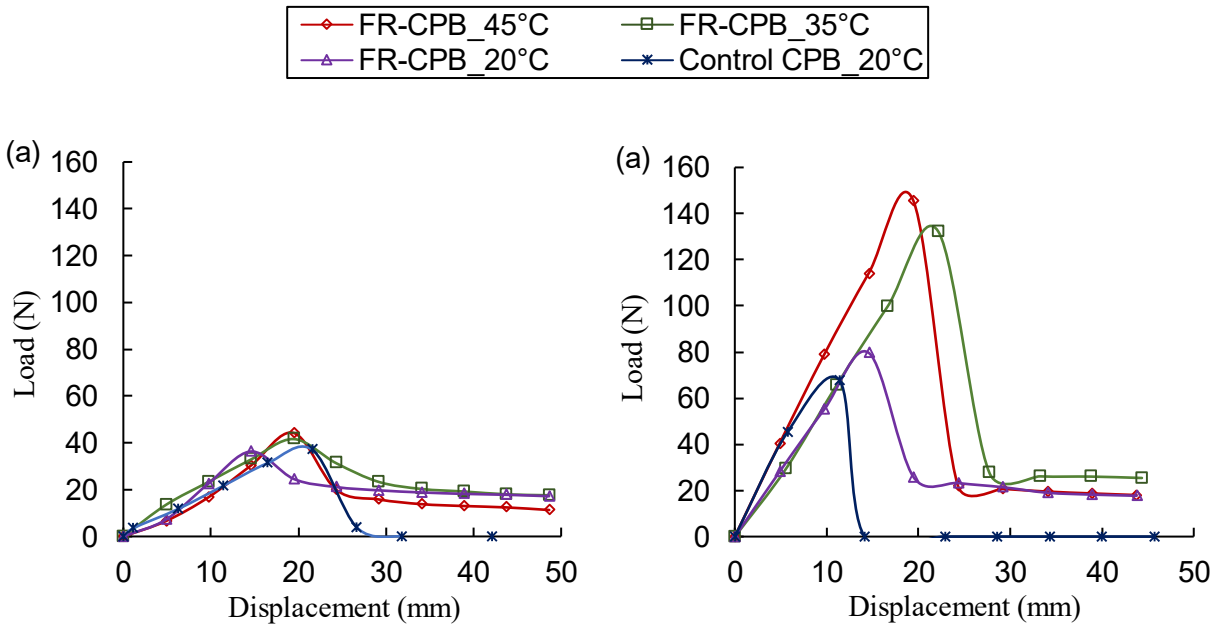

Figure 4.31 – Effect of curing temperature on the load-displacement curve of FR-CPB specimens tested on the mixed-mode fracture toughness: (a) early-age (3-day); (b) advanced-age (28-day)

4.5. Summary

This chapter exposes the findings encountered after analyzing all the data from the experimental studies, delivering useful data information and discussing potential mechanisms behind the findings. The geomechanical behavior of FR-CPB cured under warm temperature accounts for the compression, tension, shear, triaxial, and fracture performances of this material.

Concerning the compressive performance, the effect of warm temperature curing delivers properties gains to the material related to UCS peak values. When cured under 45ºC, the UCS peak was more than doubled and increments in residual strength were also observed. However, the gains are more expressive during early age. The residual strength also showcases improvements during the early ages, but it becomes limited during the advanced ages, considering the temperature factor. Additionally, FR-CPB develops larger resistance to non-permanent deformation when subjected to warmer curing temperatures. Also, for equal temperatures, fiber inclusions deliver an

inexpressive impact on the elastic modulus and stiffness when comparing FR-CPB to ordinary CPB.

The presence of fibers indeed induces the improvement of material ductility. However, the warmer curing temperature causes the development of brittleness. Compared to FR-CPB cured at 20ºC, the peaks of STS at 45ºC evidenced improvements of 50% or more at both early and advanced ages. Additionally, when the temperature comes into play, the production of hydration products is increased, which allows the matrix of FR-CPB to lock the fibers inside much stronger, permitting the material to work under higher residual stresses after failure.

Another interesting fact was to observe that the internal friction angles obtained from direct shear tests did not demonstrate expressive changes concerning temperature variation. However, properties such as shear stiffness, cohesion, and dilation angle demonstrated susceptible to temperature changes. Furthermore, higher peak shear strength, residual shear strength, and volume expansion values were collected from FR-CPB specimens subjected to warmer curing temperature. Also, the brittleness development in FR-CPB with time and temperature increase was attested by the calculated brittleness index of the material.

With the increase in curing temperature, it was observed a considerable development of the peak stresses in early-age FR-CPB subjected to confinement (triaxial shear performance). However, its modulus of elasticity evidenced minor changes concerning temperature variation. Besides, when evaluating the post-failure stage, it is evident that the development of the material`s softening behavior is undoubtedly affected by the curing temperature. While assessing the changes in advanced-age FR-CPB under confinement, peak stress, peak strain, elastic modulus, and residual strength properties evidenced strong temperature dependency. Also, it was observed that with temperature increase there is a weakening in the material`s ductility property as a reduction in elongation of the hardening section manifests. Concerning the post-failure stage, an accelerated strength reduction in the softening behavior was found since the results evidenced a gradual increase in the downwards angle after the peak as temperature elevated. Nevertheless, even with the sudden drop in strength, the residual strength still showcased a substantial development as the temperature rose.

Lastly, the fracture toughness is sensitive to curing time. Similarly to the compressive, tensile, and shear behavior of CPB, it was observed that the fracture toughness was also affected by the saturation state, curing time, and cement content. Furthermore, mode-I, mode-II, and mixed-mode

fracture toughness evidenced reasonable development of peak values in response to warm curing temperature. However, the respective residual load-bearing capacity from each fracture mode showcased inexpressive evolution concerning temperature and time factors.

Chapter 5 Conclusions and Future Work Recommendations

5.1. Conclusions

An extensive experimental testing program was conducted to investigate the geomechanical behavior of FR-CPB subjected to distinct curing temperatures (20˚C, 35˚C, and 45˚C) at 3, 7, 28, and 90 days. The geomechanical behavior of FR-CPB englobes compressive, tensile, shear, triaxial, and fracture responses that were investigated in detail through UCS, STS, DS, CU, and TPB tests. This study has shown that properties (except the internal friction angle) and performances of FR-CPB are significantly affected by warmer curing temperatures from early to advanced ages. Based on the obtained results, the following conclusions were drawn:

1. Curing temperature can significantly affect the pre- and post-failure behavior of FR-CPB subjected to compressive and tensile loading stress. Hardening and softening behavior becomes more obvious as the curing temperature increases. Moreover, the pseudo hardening behavior is commonly featured in the tensile behavior of FR-CPB and shows strong temperature sensitivity, especially during the early ages. The elastic modulus and material stiffness can be improved to a greater extent when FR-CPB is cured at a warmer temperature. Elastic modulus improvements of 83% and 182% were observed during early and advanced ages, respectively. Also, improvements of 60% and 53% referent to the material`s stiffness were obtained for early and advanced ages, respectively. The stiffer FR-CPB formed at warmer curing temperature indicates the backfill mass can offer more immediate secondary support to the surrounding walls and thus contribute to the stope stability. The compressive strength and tensile strength become more sensitive to the curing temperature at advanced ages. Compressive strength improvements of 64% and 108% were observed during early and advanced ages, respectively. Besides, improvements of 29% and 32% referent to the tensile strength were obtained for early and advanced ages, respectively. The significant improvement of the strength of advanced-age FR-CPB implies that warmer curing temperature can strengthen the fiber-matrix interfacial interaction and thus the bridging effect in the CPB matrix. Therefore, with the development of cementation of tailings particles, fiber reinforcement can significantly improve the long-term material strength of CPB cured at a warmer temperature. Compression is 6 to 10 times the value of the tensile ranging from early to advanced age.

2. As curing temperature increases, shear constitutive properties including shear stiffness, cohesion, and dilation angle show increasing trends from early to advanced ages. However, the internal friction angle of FR-CPB demonstrates comparatively low sensitivity to the curing temperature (0.1˚ to 4˚ from early to advanced ages). The inclusion of fibers shows a very limited effect on shear stiffness and cohesion, but considerably enhances the internal friction angle and dilation angle of FR-CPB. Internal friction angle improvements of 29% and 40% were observed during early and advanced ages, respectively, due to the inclusion of fibers. Additionally, improvements of 137% and 49% referent to the dilation angle (50 kPa normal stress) were obtained for early and advanced ages, respectively. The comparison between results contrasted the control group subjected to 20˚C against the FR-CPB group under 45˚C for both early and advanced ages. The increased internal friction angle is associated with the mechanical interlocking between fibers and tailings particles, while the changes in the dilation angle are mainly attributed to the sliding and rolling of tailings particles around the fiber with a relatively large diameter.
3. For the early-age FR-CPB, the shear hardening and softening behavior become more noticeable as curing temperature increases. Moreover, enhanced peak shear strength, residual shear strength, and volume expansion were observed from FR-CPB cured under warmer temperature. Additionally, the addition of polypropylene microfibers can improve the peak and residual shear strength. Peak shear strength improvements of 36% and 17% were observed when applying 50 and 150 kPa normal stress, respectively. Also, improvements of 13% and 34% referent to the residual shear strength were obtained under 50 and 150 kPa normal stress, respectively. The comparison between results contrasted the data from FR-CPB under 20˚C and 45˚C for both 50 and 150 kPa normal stresses. At advanced ages, the pre-failure hardening behavior of FR-CPB becomes more unnoticeable, while post-failure softening behavior is accompanied by consistent and considerable strength degradation as the curing temperature increases. The pre- and post-failure shear behavior of FR-CPB implies the development of material brittleness, which has been confirmed by the changes in the calculated brittleness index. However, during the post-failure stage, advanced-age FR-CPB subjected to various curing temperatures evidenced similar residual shear strength at the same normal stress.
4. The temperature factor substantially influences the behavior of FR-CPB under confinement (triaxial loading condition). Both early and advanced age FR-CPB peak values evidenced

important development with the increase of curing temperature. Also, the residual strength was improved from early and advanced ages. Under confinement, peak value improvements of 90% and 157% were observed during early and advanced ages, respectively. Besides, improvements of 105% and 130% referent to the residual strength under confinement were obtained during early and advanced ages, respectively. However, the reduction in amplitude of the peak from stress-strain curves with the increased curing temperature implies property degradation due to the development of brittleness in FR-CPB.

5. Mode-I fracture toughness of CPB from ASTM D5045 demonstrates a strong time-dependency with curing time. The major improvement in K_{IC} occurs during early age (150% increase between 3 to 7 days). Moreover, as curing time elapses, the rate of change of K_{IC} decreases (30% increase between 28 and 90 days). The micro-scale SEM observation revealed that the improvement of fracture resistance is due to the refinement of pore space by the participation of cement hydration products. The chemical shrinkage results in the self-densification process in CPB at the macro-scale, and, thus, contributes to the improvement of K_{IC}. Therefore, a larger chemical shrinkage associated with higher cement content can further improve the K_{IC} of CPB. Re-saturated CPB has a lower K_{IC} when compared to the CPB without re-saturation treatment. K_{IC} reduced from 11 kPa·m$^{1/2}$ to 7 kPa·m$^{1/2}$ when respectively comparing the unsaturated to the re-saturated results of samples containing 2% cement content. Also, it reduced even more with a 7% cement content, going from 55 kPa·m$^{1/2}$ to 36 kPa·m$^{1/2}$. Therefore, the saturation state plays a crucial role in the development of K_{IC}. The effect of saturation state on the K_{IC} is governed by matric suction and water content in CPB. Correspondingly, the evolutive water retention curves of CPB needs to be further investigated. The curing time, cement content, and saturation state significantly affect the development of K_{IC}. These three influential factors are closely related to the key chemical reaction in CPB, i.e., cement hydration.

6. The mode-I, mode-II and mixed-mode fracture toughnesses of FR-CPB evidenced gains in peak values with the rise in temperature from early to advanced ages. For example, the peak values of the mixed-mode fracture toughness improved 15% and 83% during early and advanced ages, respectively. Also, it was noticed that the material stiffness gradually develops with the curing time. However, as the curing temperature changes, no significant improvements in residual load resistance were encountered in FR-CPB subjected to different fracture mode loading conditions. Actually, the abrupt loss of fracture resistance force after the

peak point becomes more obvious as the curing temperature increases, which further confirms a more brittle response can be obtained from FR-CPB at warmer curing temperature.

The presented research achieved all pre-established objectives and delivered valuable data metrics that can be used in FR-CPB applications. The obtained results show that the curing temperature plays a vital role in the evolution of geomechanical properties and behavior of FR-CPB. Therefore, the obtained results from this study can not only improve the understanding of the fiber-reinforcement technique but also contribute to the accurate assessment of the in-situ performance of FR-CPB subjected to geothermal gradient induced warmer curing temperatures. Moreover, through the extensive experimental studies on the geomechanical behavior, the obtained results have the potential to improve the limitations associated with the conventional strength-based design method, and thus contribute to safer designs.

5.2. Recommendations

The experimental investigation of the geomechanical behavior of FR-CPB cured under warmer temperature is the primary purpose of this research. Even though many investigations were successfully conducted and finished, it is not possible to completely explore every single aspect of such complex material in a single research program. Therefore, the findings encountered in this research study will serve as guidance to foment future work recommendations to further contribute to the area. That said, the list of recommendations follows as seen:

1. Acknowledging the findings related to the UCS and STS improvements of FR-CPB due to warm curing temperature, it is necessary to incorporate the thermal factor into the design method.
2. Following a similar chain of thoughts from the first recommendation, it is recommended to develop an analytical model to design fiber-reinforced backfilled structures. If possible, integrating the results into the Building Information Modeling (BIM) technology is highly recommended.
3. The internal friction angle did not evidence expressive changes with respect to the variation of warmer temperature. However, the friction resistance between fiber and CPB matrix is dependent on the roughness of fiber surfaces. Therefore, surface roughness modification technique is a promising approach to further improve the fiber bridging effect. Moreover, the

natural fibers with higher water absorption capacity and rough surfaces should be received more attention in future works.

4. In the field, during pillar recovery procedures, the confining pressure acting on the backfilled structures is never the same in all directions due to the rearrangement of forces acting on the surrounding rock mass as the pillar is removed. Thus, the true triaxial behavior is preferred to better simulate in-situ performance, which requires a more advanced testing system.
5. Further extend the investigations over fracture toughness behavior of FR-CPB, accounting for possible effects related to distinct fiber type properties, fiber length, fiber diameter, and fiber chemical reactivity. Additionally, investigate the impact of distinct casting procedures on the fracture behavior of FR-CPB. For example, intercalation of textile meshes to cast layers of FR-CPB in a stope.
6. From the experimental data of FR-CPB subjected to warmer curing temperature obtained from this study, a solid information foundation to improve the understanding of the field behavior of this material can be used to develop a numerical analysis. For that, multiphysics and multiscale models must be established. Also, if in the future the field behavior of FR-CPB subjected to complex loading conditions needs to be quantitatively predicted, mathematical modeling should be used.

References

Aboudi, J. (1984). Elastoplasticity theory for porous materials. Mechanics of Materials, 3(1): 81-94. ISSN 0167-6636.

Andrews, E. (1974). A generalized theory of fracture mechanics. J Mater Sci, 9: 887–894.

Altun, A.,Yilmaz, I., and Yildirim, M. (2010). A short review on the surficial impacts of underground mining. Scientific Research and Essays. 5. 3206-3212.

Askarani, K.K., and Pakbaz, M.S. (2016). Drained shear strength of over-consolidated compacted soil-cement. Journal of Materials in Civil Engineering. 28(5): 04015207.

ASTM Standard C1116/C1116M. (2015). Standard Specification for Fiber-Reinforced Concrete, International A, West Conshohocken, PA. www.astm.org.

ASTM Standard C1608. (2017). Standard Test Method for Chemical Shrinkage of Hydraulic Cement Paste, International A, West Conshohocken, PA. www.astm.org.

ASTM Standard C192/C192M-13a. (2012). Standard Practice for Making and Curing Concrete Test Specimens in the Lab. Annual Book of ASTM Standards, West Conshohocken, PA.

ASTM Standard C39/C39M-18. (2018). Test Method for Compressive Strength of Cylindrical Concrete Specimens. Annual Book of ASTM Standards, West Conshohocken, PA.

ASTM Standard D3080/D3080M-11. (2011). Standard Test Method for Direct Shear Test of Soils Under Consolidated Drained Conditions. West Conshohocken, PA; ASTM International.

ASTM Standard D3967-16. (2016). Test Method for Splitting Tensile Strength of Intact Rock Core Specimens. Annual Book of ASTM Standards, West Conshohocken, PA.

ASTM Standard D5045. (2014). Standard Test Methods for Plane-Strain Fracture Toughness and Strain Energy Release Rate of Plastic Materials, International A, West Conshohocken. www.astm.org.

ASTM Standard D7263-09. (2018). Standard Test Methods for Laboratory Determination of Density (Unit Weight) of Soil Specimens, International A, West Conshohocken, PA. www.astm.org.

Aubertin, M., Li, L., Arnoldi, S., Belem, T., Bussière, B., Benzaazoua, M., et al. (2013). Interaction between backfill and rock mass in narrow stopes. 12th Panamerican Conference on Soil Mechanics & Geotechnical Engineering and 39th US Rock Mechanics Symposium Cambridge, USA: 1157-64.

Aubynn, A. (2009). Sustainable solution or a marriage of inconvinience? The coexistence of large-scale mining and artisanal and small-scalle mining on the Abosso Goldfields concession in Western Ghana. Resources Policy, 34, 64-70.

Barrett, J. R., Coulthard, M. A. and Dight, P. M. (1978). Determination of Fill Stability, Mining with Backfill, 12th Canadian Rock Mechanics Symposium, CIM Special Volume 19, Sudbury, Ontario May 23-25.

Bekele, A., Ryden, N., Gudmarsson, A., and Birgisson, B. (2019). Effect of cyclic low-temperature conditioning on stiffness modulus of asphalt concrete based on non-contact resonance testing method, Constr. Build. Mater. 225: 502-509.

Belem, T., and Benzaazoua, M. (2008). Design and Application of Underground Mine Paste Backfill Technology. Geotechnical and Geological Engineering, 26(2): 147–174.

Belem, T., Benzaazoua, M., Bussière, B., and Dagenais, A. (2002). Effects of settlement and drainage on strength development within mine paste backfill. Proceedings of the 9th International Conference on Tailings and Mine Waste, 27–30 January: 139-148.

Belem, T., Fourie, A., and Fahey, M. (2010). Time-dependent failure criterion for cemented paste backfills. Proceedings of the Thirteenth International Seminar on Paste and Thickened Tailings: Australian Centre for Geomechanics: 147-62.

Bhaskar, P., and Mohamed, R. H. (2012). Analytical estimation of elastic properties of polypropylene fiber matrix composite by finite element analysis, Advances in Materials Physics and Chemistry 2012: 23-30.

Blackwell, D. D., and Steele, J. L. (1989). Heat flow and geothermal potential of Kansas, Kansas Geol. Surv. Bull. Geophys. Kansas; 226: 267-295.

Bloss, M. (2002). Below ground disposal (mine backfill). In: Jewell, R.J., Fourie, A.B., Lord, E.R. (Eds.), *Paste and Thickened Tailings: A Guide*. University of Western Australia, Nedlands: 103–126.

Borgesson, L. (1981). Mechanical properties of hydraulic backfill. In*: Application of rock mechanics to cut and Fill mining*. London: IMM. 193-195.

Boutouba, K., Benessalah, I., Arab, A., and Henni, A.D. (2019). Shear strength enhancement of cemented reinforced sand: role of cement content on the macro-mechanical behavior. Studia Geotechnica et Mechanica. 41(1): 200-11.

Brackebusch, F.W. (1994). Basics of paste backfill systems. Mining Engineering, 46(10): 1175–1178.

Brown, E. T. (2003). Block caving geomechanics. The international caving JKMRC monograph series in mining and mineral processing, University of Queensland, vol. 3.

Cao, S., Yilmaz, E., and Song, W. (2019). Fiber type effect on strength, toughness and microstructure of early age cemented tailings backfill, Construction and Building Materials, 223: 44-54.

Castendyk, D.N., and Eary, L.E. (2009a). Mine pit lakes: characteristics, predictive modeling, and sustainability . Littleton, Colorado , Society for Mining, Metallurgy, and Exploration.

Chen, J., Gu, D., and Li, J. (2003). Optimization principle of combined surface and underground mining and its applications. Journal of Central South University of Technology. 10: 222-225.

Chen, J.; Li, K.; Chang, K.; Sofia, G., and Tarolli, P. (2015). Open-pit mining geomorphic feature characterisation. International Journal of Applied Earth Observation and Geoinformation. 42: 76–86.

Chen, X., Shi, X.Z., Zhang, S., Chen, H., Zhou, J., Yu, Z., and Huang, P.S. (2020). Fiber-reinforced cemented paste backfill: the effect of fiber on strength properties and estimation of strength using nonlinear models. Mater., 13(3): 718.

Chen, X., Shi, X.Z., Zhou, J., and Yu, Z. (2019). Influence of Polypropylene Fiber Reinforcement on Tensile Behavior and Failure Mode of Tailings Cemented Paste Backfill. *IEEE Access*.

Cheng, H., Wu, S., Li, H., and Zhang, X.(2020). Influence of time and temperature on rheology and flow performance of cemented paste backfill. Construction and Building Materials. 231: 117117.

Clough, G.W., Sitar, N., Bachus, R.C., and Rad, N.S. (1981). Cemented sands under static loading. Journal of Geotechnical and Geoenvironmental Engineering. 107: 798-817.

Consoli, N.C., Casagrande, M., Thomé, A., Dalla-Rosa, F., and Fahey, M. (2009). Effect of relative density on plate loading tests on fibre-reinforced sand. Géotechnique. 59(5): 471-76.

Consoli, N.C., Prietto, P.D., and Ulbrich, L.A. (1998). Influence of fiber and cement addition on behavior of sandy soil. Journal of Geotechnical and Geoenvironmental Engineering. 124(12): 1211-14.

Cooke, R. (2001). Design procedure for hydraulic backfill distribution systems. J South Afr Inst Min Metall, 101: 97–102.

Cui, L., and Fall, M. (2016a). An evolutive elasto-plastic model for cemented paste backfill. Comput Geotech, 71: 19-29.

Cui, L., and Fall, M. (2016b). Mechanical and thermal properties of cemented tailings materials at early ages: Influence of initial temperature, curing stress and drainage conditions. Construction and Building Materials. 125: 553-63.

Cui, L., and Fall, M. (2017). Multiphysics modeling of arching effects in fill mass. Computers and Geotechnics. 83: 114-31.

Cui, L., and Fall, M. (2018a). Modeling of self-desiccation in a cemented backfill structure. Int J Numer Anal Methods Geomech. 42: 558-83.

Cui, L., and Fall, M. (2018b). Multiphysics modeling and simulation of strength development and distribution in cemented tailings backfill structures. Int J Concr Struct Mater. 12: 25.

Dagdelen, K. (2000). Open pit optimization—strategies for improving economics of mining projects through mine planning. Application Computers for Mining Industry.

Deb, D., Sreenivas, T.,Dey, G.K, and Panchal, S. (2017). Paste backfill technology: Essential characteristics and assessment of its application for mill rejects of uranium ores. Trans. Indian Inst. Met., 70: 487-495.

DeJong, J., and Westgate, Z. (2005). Role of overconsolidation on sand–geomembrane interface response and material damage evolution. Geotextiles and Geomembranes. 23(6): 486-512.

Desjardins, J. (2013). What is the Cost of Mining Gold?. Visual Capitalist.

Di W., Run-kang Z., Chao-wu X., and Shuai L. (2020). Effect of curing humidity on performance of cemented paste backfill, Int. J. Miner. Metall. Mater. https://doi.org/10.1007/s12613-020-1970-y.

Diambra, A., Ibraim, E., Wood, D.M., and Russell, A. (2010). Fibre reinforced sands: experiments and modelling. Geotextiles and Geomembranes. 28(3): 238-50.

Dimitrakopoulos, R., and Ramazan, S. (2003). Managing risk and waste mining in long-term production planning of open pit mine, in SME Annual Meeting & Exhibition: 03-151.

Eary, L.E., and Castendyk, D.N. (2009). The state of the art of pit lake research. In: Castendyk D.N. and Eary L.E. *Mine pit lakes: characteristics, predictive modeling, and sustainability*. Littleton, Colorado: 275-289.

Edraki, M., Baumgartl, T., Manlapig, E., Bradshaw, D., Franks, D.M., and Moran C.J. (2014). Designing mine tailings for better environmental, social and economic outcomes: a review of alternative approaches. J. Cleaner Prod., 84: 411-420.

Emad, M.Z., Mitri H., and Kelly, C. (2015). State-of-the-art review of backfill practices for sublevel stoping system, International Journal of Mining, Reclamation and Environment, 29(6): 544-556.

Fall, M., and Pokharel, M. (2010). Coupled effects of sulphate and temperature on the strength development of cemented tailings backfills: Portland cement-paste backfill. Cement and Concrete Composites. 32(10): 819-28.

Fall, M., and Samb, S. (2009). Effect of high temperature on strength and microstructural properties of cemented paste backfill. Fire Safety Journal, 44(4), 642-651.

Fall, M., Adrien, D., Célestin, J.C., Pokharel, M., and Touré, M. (2009). Saturated hydraulic conductivity of cemented paste backfill, Minerals Engineering, 22(15): 1307-1317.

Fall, M., Célestin, J., Pokharel, M., and Touré, M. (2010). A contribution to understanding the effects of curing temperature on the mechanical properties of mine cemented tailings backfill. Engineering Geology; 114(3-4): 397-413.

Falorca, I., and Pinto, M. (2011). Effect of short, randomly distributed polypropylene microfibres on shear strength behaviour of soils. Geosynthetics International. 18(1): 2-11.

Feng, G., Kang, Y., and Wang, X.C. (2019). Fracture failure of granite after varied durations of thermal treatment: an experimental study. Royal Society open science. 6, 10.1098/rsos.190144.

Festugato, L., Fourie, A., and Consoli, N. (2013). Cyclic shear response of fibre-reinforced cemented paste backfill. Géotechnique Letters, 3(1): 5-12.

Fourie, A.B., Copeland, A.M., and Barrett, A.J. (1994). Optimisation of the As-placed Properties of Hydraulic Backfill. Journal of the South African Institute of Mining and Metallurgy, 94(8): 199-209.

Fredlund, D.G., Xing, A., Fredlund, M.D., and Barbour, S.L. (1996). The relationship of the unsaturated soil shear strength to the soil-water characteristic curve. Canadian Geotechnical Journal. 33(3): 440-48.

Gafoor, A. H., and Dinkler, D. (2020) A macroscopic gradient-enhanced damage model for deformation behavior of concrete under cyclic loadings, Arch Appl Mech: 1-21.

Gardner, J. S., and Sainato, P. (2007). Mountaintop mining and sustainable development in Appalachia. Pro Quest Science Journals. Mining Engineering, 59(3), 48-55.

Gettu, R., Bazant, Z.P., and Karr, M.E. (1990). Fracture properties and brittleness of high-strength concrete. ACI Materials Journal. 87(6): 608-18.

Ghirian, A., and Fall, M. (2013). Coupled thermo-hydro-mechanical–chemical behavior of cemented paste backfill in column experiments. Part I: Physical, hydraulic and thermal processes and characteristics. Engineering Geology,164: 195-207. ISSN 0013-7952.

Ghirian, A., and Fall, M. (2014). Coupled thermo-hydro-mechanical–chemical behavior of cemented paste backfill in column experiments: Part II: Mechanical, chemical and microstructural processes and characteristics. Engineering Geology, 170: 11-23. ISSN 0013-7952.

Ghirian, A., and Fall, M. (2015). Coupled behavior of cemented paste backfill at early ages. Geotech Geol Eng. 33: 1141-66.

Godoy, M., and Dimitrakopoulos, R. (2004). Managing risk and waste mining in long-term production scheduling, SME Transactions, 316.

Grant, C.D. (2006), State-and-Transition Successional Model for Bauxite Mining Rehabilitation in the Jarrah Forest of Western Australia. Restoration Ecology, 14: 28-37.

Grice, A.G. (1998). Underground mining with backfill, The 2nd Annual Summit - Mine Tailings Disposal Systems. Brisbane, Australia.

Hamidi, A., and Dehghan, A. (2015). Impact of fiber reinforcement on deformation characteristics of cemented sand-gravel mixtures. Journal of Engineering Geology. 9(2): 2729-50.

Hamidi, A., and Hooresfand, M. (2013). Effect of fiber reinforcement on triaxial shear behavior of cement treated sand. Geotextiles and Geomembranes. 36: 1-9.

Hamrin, H. (1997). Guide to Underground Mining Methods and Applications. Stockholm: Atlas copco.

Hamrin, H., Hustrulid, W. A., and Bullock, R. L. (2001). Underground mining methods and applications. *Underground Mining Methods: Engineering Fundamentals and International Case Studies*, (SME, Littleton, CO) 3–14.

Hansen, L. (2009). A plea to President Obama: end mountaintop coal minng. Yale Environment 360.

Hartman, L. H., and Mutmansky, J. M. (2002). Introductory Mining Engineering. 2nd ed. John Wiley and Sons, Inc., Hoboken, New Jersey. 584p.

Harraz, H. (2010). Underground mining Methods. 10.13140/RG.2.1.2881.1124.

Harries, K.A., and McNeice, D.S. (2006). Performance-based design of high-rise coupled wall systems. Struct Des Tall Special Build, 15: 289-306.

Hassani, F., and Archibald, J. (1998). Mine Backfill, Canadian Institute of Mining, Metallurgy, and Petroleum, Montreal, Canada.

Helinski, M., Fahey, M., and Fourie, A.J. (2010). Behavior of cemented paste backfill in two mine stopes: measurements and modeling. Journal of Geotechnical and Geoenvironmental Engineering. 137(2): 171-82.

Henning, J.G., and Mitri, H.S. (2008). Assessment and Control of Ore Dilution in Long Hole Mining: Case Studies. Geotech Geol Eng, 26: 349–366.

Hilson, G., and Murck, B. (2000). Sustainable development in the mining industry: clarifying the cooperate perspective. Resources Policy, 26, 227-238.

Hilson, G., and Basu, A. J. (2003). Devising indicators of sustainable development for the mining and minerals industry: an analysis of critical background issues. International Journal of Sustainable Development and World Ecology, 10(4), 319-332.

Hochbaum, D. and Chen, A. (2000). Improved Planning for the Open-Pit Mining Problem, Operations Research. 48(6).

Huang, S., Li, G., Ben-Awuah, E., Afum B.O., and Hu, N. (2019). A robust mixed integer linear programming framework for underground cut-and-fill mining production scheduling, International Journal of Mining, Reclamation and Environment.

ICC ES AC32. (2018). Performance-based Standard Specification for Synthetic Fiber-Reinforced Concrete, International Code Council.

ISRM. (2007). The complete ISRM suggested methods for rock characterization, testing and monitoring: 1974–2006. In: Ulusay R, Hudson JA (eds) Suggested methods prepared by the commission on testing methods, International Society for Rock Mechanics, compilation arranged by the ISRM Turkish National Group. Kozan Ofset, Ankara.

Jarosz, A. P., and Shepherd, L. (1998). Open stope cavity monitoring for the control of dilution and ore loss. Mining Engineering, (8): 63–67.

Jayanta, B. (2007). Principles of Mine Planning. 2nd edn, Wide Publishing, 505p. ISBN 81-7764-480-7.

Jianhua, H., Zhao, F., Ren, Q., Kuang, Y., Zhou, T. and Luo, Z. (2019). Microscopic characterization and strength characteristics of cemented backfill under different humidity curing conditions. R. Soc. open sci. 6:191227.

Johnson, D. B., and Hallberg, K. B. (2005). Acid mine drainage remediation options: a review, Science of The Total Environment. 338(1–2): 3-14.

Johnson, J., Seymour, J., Martin, L., Stepan, M., Arkoosh, A., and Emery, T. (2015). Strength and elastic properties of paste backfill at the Lucky Friday Mine, Mullan, Idaho. 49th US Rock Mechanics/Geomechanics Symposium, American Rock Mechanics Association.

Karaoglu K., and Yilmaz E. 2017. Cemented Paste Backfill Pressure Monitoring and Field Testing. In: Yilmaz E., Fall M. (eds) Paste Tailings Management. Springer, Cham.

Kayadelen, C., Tekinsoy, M., and Taşkıran, T. (2007). Influence of matric suction on shear strength behavior of a residual clayey soil. Environmental Geology. 53(4): 891.

Kebede, K., Titus, A.M., and Bhekie, B. (2017). Acid mine drainage: Prevention, treatment options, and resource recovery: A review. Journal of Cleaner Production, 151, 475-493.

Kesimal, A., Yilmaz, E., Ercikdi, B., Alp, I., and Deveci, H. (2005). "Effect of properties of tailings and binder on the short- and long-term strength and stability of cemented paste backfill. Materials Letters, 59, 3703-3709.

Kevorkian, J. and Cole, J. (1996). Multiple-scale and singular perturbation methods, Springer, ISBN 978-0-387-94202-5.

Kim, J., Ali, M., and Yang, H. (2019). Robust Design of Pillar Arrangement for Safe Room-and-Pillar Mining Method. Geotech Geol Eng, 37, 1931–1942.

Kim, Y. J., Hu, J., Lee, S. J., and You, B. H. (2010). Mechanical properties of fiber-reinforced lightweight concrete containing surfactant, Advances in Civil Engineering 2010: 1-8.

Kropp, R., Cramer, S. M., and Anderson, M. A. (2012). Laboratory Study of High Performance Curing Compounds for Concrete Pavement: Final Report. Phase I, Wisconsin Highway Research Program.

Kuruppu, M.D., Obara, Y., Ayatollahi, M.R., Chong, K.P., and Funatsu, T. (2014). ISRM suggested method for determining the mode I fracture toughness using semi-circular bend specimen. Rock Mech. Rock Eng. 47, 267-274.

Kutanaei, S.S., and Choobbasti, A. (2016). Triaxial behavior of fiber-reinforced cemented sand. Journal of Adhesion Science and Technology.30(6): 579-93.

Lane, C. (1998). Reducing Capital and Operating Costs by Using Inpit Tailings Disposal: Marymia Gold Operations Case History, 2nd Annual Summit - Mine Tailings Disposal Systems, AIC Worldwide, Brisbane.

Laurence, D. (2011). Establishing a sustainable mining operation: an overview. Journal of Cleaner Production, 19, 278-284.

Laurence, D. C. (2005). Safety rules and regulations on mine sites – The problem and a solution. Journal of Safety Research, 36(1), 39-50.

Lee, H., and Jeon, S. (2011). An experimental and numerical study of fracture coalescence in pre-cracked specimens under uniaxial compression. International Journal of Solids and Structures. 48(6): 979-99.

Lerchs, H., and Grossmann, I. (1965). Optimum design of open-pit mines. Canadian mining and metallurgical bulletin LXVIII, 17–24.

Li, M., Zhang, J., and Gao, R. (2016). Compression Characteristics of Solid Wastes as Backfill Materials. *Adv. Mater. Sci. Eng*. 2496194.

Liu, G., Li, L., Yang, X., and Guo, L. (2016). A numerical analysis of the stress distribution in backfilled stopes considering nonplanar interfaces between the backfill and rock walls. Int J Geotech Eng, 10: 271-82.

Liu, J. F., Yang, H.Q., Xiao, Y., and Zhou, XP. (2018). Macromesoscopic fracture and strength character of pre-cracked granite under stress relaxation condition. Rock Mech. Rock Eng. 51,1401-1412.

Liu, L., Liu, H., Stuedlein, A. W., Evans, T.M., and Xiao, Y. (2019). Strength, stiffness, and microstructure characteristics of biocemented calcareous sand, Can. Geotech. J. 56(10): 1502-1513.

Maher, M., and Ho, Y. (1993). Behavior of fiber-reinforced cemented sand under static and cyclic loads. Geotechnical Testing Journal. 16(3): 330-38.

Marschalko, M., Bednárik, M., Yilmaz, I., Bouchal, T., and Kubečka, K. (2012). Evaluation of subsidence due to underground coal mining: an example from the Czech Republic. *Bulletin of Engineering Geology*, 71(1), 105-111.

Martin, B. E., Chen, W., Song, B., and Akers, S. A. (2009). Moisture effects on the high strain-rate behavior of sand, Mech Mater. 41(6): 86-798.

Matallah, M., Farah, M., Grondin, F., Loukili, A., and Rozière, E. (2013). Size-independent fracture energy of concrete at very early ages by inverse analysis. Eng Fract Mech, 109: 1-16.

Mbonimpa, M., Kwizera, P., and Belem, T. (2019). Mine backfilling in the permafrost, part II: effect of declining curing temperature on the short-term unconfined compressive strength of cemented paste backfills. Minerals; 9(3): 172.

McCullough, C.D., Hunt, D., and Evans, L.H. (2009a). Sustainable development of open pit mines: Creating beneficial end uses for pit lakes. In *Mine Pit Lakes: Characteristics, predictive modeling, and Sutainability*, D.N Castendyk and L.E. Eary,eds.,249-268. Littleton, CO: Society for Mining, Metarllurgy, and Exploration (SME).

Meng, L., Li, T., Jiang, Y., Wang, R., and Li, Y.J.T. (2013). Characteristics and mechanisms of large deformation in the Zhegu mountain tunnel on the Sichuan–Tibet highway. Tunnelling and Underground Space Technology. 37: 157-64.

Michalowski, R.L., and Čermák, J. (2003). Triaxial compression of sand reinforced with fibers. Journal of Geotechnical and Geoenvironmental Engineering. 129(2): 125-36.

Mitchell, R. J., and Stone, D. M. (1987). Stability of reinforced cemented backfills. Canadian Geotechnical Journal, 24(2), 189-197.

Nasir, O., and Fall, M. (2010). Coupling binder hydration, temperature and compressive strength development of underground cemented paste backfill at early ages. Tunnelling Underground Space Technol. 25: 9-20.

Nyberg, U., and Fjellborg, S. (2000). Controlled drifting and estimation of blast damage. In: Proceedings of first world conference on explosives and blasting technique, Munich, Germany, 6–8 September, Rotterdam: Balkema, p. 207–216.

Okubo, S., and Yamatomi, J. (2009) Underground mining methods and equipment. In: *Civil engineering*, vol 2.

Orejarena, L., and Fall, M. (2008). Mechanical response of a mine composite material to extreme heat. Bulletin of Engineering Geology and the Environment. 67: 387-396. 10.1007/s10064-008-0148-z.

Pariseau, W. G., and Kealy, C. D. (1972). Support Potential of Hydraulic Backfill. Proc. 14th U.S. Symposium on Rock Mechanics (New Horizons in Rock Mechanics), ASCE, N.Y.: 501-526.

Peng, S. (2006). Longwall mining, 2nd edn. Peng SS publisher, Morgantown, WV, 14: 486-507.

Peyronnard, O., and Benzaazoua, M. (2012). Alternative by-product based binders for cemented mine backfill: Recipes optimisation using Taguchi method. Miner Eng., 29: 28-38.

Pham D. C. 2000. From local failure toward global collapse of elastic–plastic structures in fluctuating fields. International Journal of Mechanical Sciences, 42(4), 819-829.

Pichler, C., Lackner, R., and Mang, H.A. (2007). A multiscale micromechanics model for the autogenous-shrinkage deformation of early-age cement-based materials. Eng Fract Mech. 74: 34-58.

Pourmalek, A., and Shariatipour, S. M. (2019). Dependence on temperature and salinity gradients and the injection rate of CO2 storage in saline aquifers with an angular unconformity. *Journal of Porous Media*, 22(8).

Qi, C., and Fourie, A. (2019). Cemented paste backfill for mineral tailings management: Review and future perspectives, Minerals Engineering, 144, 106025, ISSN 0892-6875.

Rahimi-Aghdam, S., Bažant, Z.P., and Qomi, M.A. (2017). Cement hydration from hours to centuries controlled by diffusion through barrier shells of CSH. J Mech Phys Solids. 99: 211-24.

Rajaram, V., Dutta, S., and Parameswaran, K. (2005). Sustainable mining practices: a global perspective. Taylor and Francis Group, London UK, ISBN 90 5809 689 0.

Salah-ud-din, M. (2012). Behaviour of fibre reinforced cemented sand at high pressures. Ph.D. Thesis. Nottingham, England: University of Nottingham.

Sasmal, S., and Anoop, M. B. (2019). Nanoindentation for evaluation of properties of cement hydration products, in: F. Pacheco-Torgal, M.V. Diamanti, A. Nazari, C.G. Granqvist, A. Pruna, S. Amirkhanian (Eds.), Nanotechnology in Eco-efficient Construction (Second Edition), Woodhead Publishing: 141-161.

Schindler, A. K. (2004). Effect of Temperature on Hydration of Cementitious Materials. Materials Journal, 101(1), 72-81.

Schnaid, F., Prietto, P.D., and Consoli, N.C. (2001). Characterization of cemented sand in triaxial compression. Journal of Geotechnical and Geoenvironmental Engineering. 127(10): 857-68.

Scoble, M. J., and Moss, A. (1994). Dilution in underground bulk mining: Implications for production management, mineral resource evaluation, II: Methods and case histories. Geol. Soc. Sp. Publ., 79: 95–108.

Sheshpari, M. (2015). A review of underground mine backfilling methods with emphasis on cemented paste backfill. Electron. J. Geotech. Eng., 20: 5183-5208.

Singh, P., Roy, M., Paswan, R., Sarim, Md., Kumar, S., and Jha, R. (2016). Rock fragmentation control in opencast blasting. Journal of Rock Mechanics and Geotechnical Engineering, 8(2) ,225-237.

Simms, P., and Grabinsky, M. (2009). Direct measurement of matric suction in triaxial tests on early-age cemented paste backfill. Can Geotech J.,46: 93-101.

Sivakugan N., Veenstra R. and Naguleswaran N. (2015). International Journal of Geosynthetics and Ground Engineering. 1: 18. https://doi.org/10.1007/s40891-015-0020-8.

Smith, J.D., and Mitchell, R.J. (1982). Design and control of large hydraulic backfill pours. CIM Bulletin, 75(838): 102-111.

Spiegel, S. J. (2009). Resources policies and small-scale gold mining in Zimbabwe. Resources Policy, 34(1,2), 39-44.

Su, W. H., and Peng, S. S. (1987). Cutter roof and its causes, Mining Science and Technology. 4(2): 113-132.

Sun, Q., Zhou, N., Quan, K., and Chen, Y. (2017). Stability analysis and control of embankment with solid backfill coal mining. Min. Technol. 126, 104–112.

Susmel, L. (2009). Multiaxial Notch Fatigue: From Nominal to Local Stress/Strain Quantities. Multiaxial Notch Fatigue: From Nominal to Local Stress/Strain Quantities. 1-566.

Tariq, A., and Yanful, E.K. (2013). A review of binders used in cemented paste tailings for underground and surface disposal practices. J Environ Manage. 131:138-49.

Tazawa, E., Miyazawa, S., and Kasai, T. (1995). Chemical shrinkage and autogenous shrinkage of hydrating cement paste. Cem Concr Res. 25:288-92.

Topal, E., and Sens, J. (2010). A new algorithm for stope boundary optimization. J Coal Sci Eng China 16, 113–119.

Tu, L., Kruger, D., Wagener, J., and Carstens, P. (1998). Surface modified polypropylene fibres for use in concrete. Magazine of Concrete Research. 50(3): 209-17.

US Environmental Protection Agency – US EPA. (1989). Stabilization/solidification of CERCLA and RCRA wastes: physical tests, chemical testing procedures, technology screening, and field activities, EPA/625/6-89/022. Risk Reduction Engineering Laboratory Cincinnati, USA.

Villaescusa, E. (1998). Geotechnical design for dilution control in underground mining. In *Proc. Seventh International Symposium on Mine Planning and Equipment*, Balkema, Calgary, 141-149.

Villaescusa, E., and Kuganathan, K. (1998). Backfill for Bench Stoping Operations, Minefill 98, AusIMM, Brisbane.

Weber, I. (2005). Actualizing sustainable mining: whole mine, ehole community, whole planet through industrial ecology and community-based strategies. Society of Mining Engineers, USA.

Xiawei, Y. (2016). "Experimental studies on the stability of reinforced cemented paste backfill." PhD Dissertation, The University of Western Australia.

Yan, B., Zhu, W., Hou, C., Yu, Y., and Guan, K. (2020). Effects of coupled sulphate and temperature on internal strain and strength evolution of cemented paste backfill at early age. Constr Build Mater. 230: 116937.

Yao, Y., and Chen, S. The effects of fiber's surface roughness on the mechanical properties of fiber-reinforced polymer composites. Journal of Composite Materials 2013; 47(23): 2909-23.

Yi, X., Ma, G., and Fourie, A. (2015). Compressive behaviour of fibre-reinforced cemented paste backfill. Geotextiles and Geomembranes, 43(3): 207-215.

Yilmaz, E., Belem, T., and Benzaazoua, M. (2015). Specimen size effect on strength behavior of cemented paste backfills subjected to different placement conditions. Engineering Geology, 185: 52–62.

Yu, K., Wang, Y., Yu, J., and Xu, S. (2017). A strain-hardening cementitious composites with the tensile capacity up to 8%. Construction and Building Materials. 137: 410-19.

Yuan, Y., Wang, W., Li, S., and Zhu, Y. (2018). Failure mechanism for surrounding rock of deep circular roadway in coal mine based on mining-induced plastic zone. Advances in Civil Engineering. 1-14.

Zhang, J., Fu, M., Hassani, F.P., Zeng, H., Geng, Y., and Bai, Z. (2011). Land Use-Based Landscape Planning and Restoration in Mine Closure Areas. Environmental Management 47, 739–750.

Zhang, J., Li, M., Taheri, A., Zhang, W., Wu, Z., and Song, W. (2019). Properties and Application of Backfill Materials in Coal Mines in China. *Minerals*, *9*, 53.

Zhang, T., Gao, P., Luo, R., Guo, Y., Wei, J., and Yu, Q. (2013). Measurement of chemical shrinkage of cement paste: Comparison study of ASTM C 1608 and an improved method. Constr Build Mater. 48:662-9.

Xu, W., and Cao, P. (2018). Fracture behaviour of cemented tailing backfill with pre-existing crack and thermal treatment under three-point bending loading: Experimental studies and particle flow code simulation. Eng Fract Mech, 195:129-41.

Xu, W., Li, Q., and Zhang, Y. (2019). Influence of temperature on compressive strength, microstructure properties and failure pattern of fiber-reinforced cemented tailings backfill. *Construction and Building Materials*, 222, 776-785.

Xue, G., Yilmaz, E., Song, W., Cao, S. (2020). Fiber length effect on strength properties of polypropylene fiber reinforced cemented tailings backfill specimens with different sizes. Constr Build Mater. 241: 118113.

Walske, M. (2014). An experimental study of cementing paste backfill [Ph.D. Thesis]. Perth, Australia: The University of Western Australia.

Wang, H. S., Tang, C. S., Gu, K., Shi, B., and Inyang, H. I. (2020). Mechanical behavior of fiber-reinforced, chemically stabilized dredged sludge, B Eng Geol Environ 79(2): 629-643.

Wang, K., Shah, S.P. and Mishulovich, A. (2004). Effects of curing temperature and NaOH addition on hydration and strength development of clinker-free CKD-fly ash binders. Cement and Concrete Research, 34(2), 299-309.

Wang, Y., Fall, M., Wu, A.(2016). Initial temperature-dependence of strength development and self-desiccation in cemented paste backfill that contains sodium silicate. Cem Concr Compos;67:101-10.

Wu, D., Fall, M., and Cai, S. (2013). Coupling temperature, cement hydration and rheological behavior of fresh cemented paste backfill. Minerals Engineering; 42: 76-87.